AD_____

Award Number: DAMD17-99-1-9391

TITLE: MRI Assessment of the Viscoelastic Properties of Normal and Abnormal Breast Tissue

PRINCIPAL INVESTIGATOR: Donald B. Plewes, Ph.D.

CONTRACTING ORGANIZATION: Sunnybrook and Women's Health Sciences Center
Toronto, Ontario M4N 3M5 Canada

REPORT DATE: January 2003

TYPE OF REPORT: Final

PREPARED FOR: U.S. Army Medical Research and Materiel Command
Fort Detrick, Maryland 21702-5012

REPORT DOCUMENTATION PAGE

Form Approved
OMB No. 074-0188

1. AGENCY USE ONLY (Leave blank)	2. REPORT DATE	3. REPORT TYPE AND DATES COVERED
	January 2003	Final (1 Jul 99 - 31 Dec 02)

4. TITLE AND SUBTITLE
MRI Assessment of the Viscoelastic Properties of Normal and Abnormal Breast Tissue

5. FUNDING NUMBERS
DAMD17-99-1-9391

6. AUTHOR(S)
Donald B. Plewes, Ph.D.

7. PERFORMING ORGANIZATION NAME(S) AND ADDRESS(ES)
Sunnybrook and Women's Health Sciences Center
Toronto, Ontario M4N 3M5 Canada

E-Mail: don.plewes@swchsc.on.ca

8. PERFORMING ORGANIZATION REPORT NUMBER

9. SPONSORING / MONITORING AGENCY NAME(S) AND ADDRESS(ES)
U.S. Army Medical Research and Materiel Command
Fort Detrick, Maryland 21702-5012

10. SPONSORING / MONITORING AGENCY REPORT NUMBER

11. SUPPLEMENTARY NOTES

12a. DISTRIBUTION / AVAILABILITY STATEMENT
Approved for Public Release; Distribution Unlimited

12b. DISTRIBUTION CODE

13. ABSTRACT (Maximum 200 Words)

Biological tissue stiffness alteration resulting from pathological processes has been known for centuries. Many investigators have considered tissue stiffness an attractive property that can be used to detect disease and aid in differentiation between normal and benign breast tissues. As a result elastography, an imaging technique which images tissue elasticity, was developed. Interpreting elastography images requires knowledge of elastic properties of various normal and abnormal tissues. Studies conducted over the past years suggest the presence of large variations in elastic modulus of each breast tissue type. In addition to using inaccurate mathematical models to obtain these data, the measured mechanical behavior was subject to sampling errors arising from tissue heterogeneity within the tissue samples and potential differences arising from ex-vivo conditions and tissue sample handling. As a result, repeatable measurements have been hard to achieve, thus the obtained data are less reliable. The goal of this project is to assess the ex-vivo and in-vivo biomechanical properties of normal, benign and cancerous breast tissues with an MRI method. During our first year of funding, we have developed two uniaxial loading systems, an MRI-based and table-top system. Also, we developed various inverse solution algorithms for reconstruction of elastic modulus using MRI derived displacement data. During our second year, we have integrated, optimized and tested the table-top system. Throughout our third year, we have used these systems along with reconstructions algorithms to measure the elastic properties of over 120 breast tissue specimens. Furthermore, we have developed a novel technique to measure the elastic properties of small tumors in breast slice in addition to an inversion technique for hyperelastic parameters estimation of breast tissues. Finally, an MRI based technique was developed to reconstruct breast hyperelastic parameters in-vivo.

14. SUBJECT TERMS
breast cancer, biomechanics, MRI, elastography, finite element method

15. NUMBER OF PAGES
107

16. PRICE CODE

17. SECURITY CLASSIFICATION OF REPORT	18. SECURITY CLASSIFICATION OF THIS PAGE	19. SECURITY CLASSIFICATION OF ABSTRACT	20. LIMITATION OF ABSTRACT
Unclassified	Unclassified	Unclassified	Unlimited

Table of Contents

MRI Assessment of the Viscoelastic Properties of Normal and Abnormal Breast Tissue: Final Report to the US Army

INTRODUCTION

Biological tissue stiffness alteration resulting from pathological processes has been known for centuries. Recent studies both in-vitro[1,2] and in-vivo[3,4] have indicated that quantitative knowledge of tissue elasticity can be used in detecting and differentiating between different types of breast cancer. During the past several years, a number of investigators[3,4,5,6,7] have been attempting to use elastography: a noninvasive imaging technique which images tissue stiffness as a means for breast cancer diagnosis. The goal of this research project is to lay the foundation required to interpret breast elastography by accurately measuring breast tissue elasticity both in-vivo via MRI elastography and in-vitro using a computerized electro-mechanical measurement system. In addition to having the potential of aiding in improved diagnosis of breast cancer, the results of this investigation can be used in predicting tissue deformation. The latter is very important in various medical applications such as breast image coregistration, image data fusion and image guided surgery.

For in-vivo breast tissue measurement, we developed MR elastography (MRE) techniques where MRI motion detection methods are applied to measure tissue strain while the surface is undergoing external gentle forces with a slowly moving plate. By an analysis of the resulting motions and through the use of a constrained inversion technique[7,8], we reconstruct the distribution of tissue elastic and hyperelastic properties in-vivo. To measure the elastic properties in-vitro, in addition to using a home built electro-mechanical system, we have developed an MRI measurement technique where a tissue specimen is encased inside a block of agar-gelatin, which undergoes an MRE test. In this technique, the elastic modulus of the specimen is calculated using the same constrained inversion technique[7]. Using these methods, measurements have been performed on over 120 normal and abnormal breast tissue specimens with determined pathologies. Based on these data, the feasibility of determining the type of breast tissue abnormality and predicting tissue deformation in-vivo will be assessed.

RESEARCH TASKS

This research project is a three-year project with a number of goals and tasks. In line with our goals, the following tasks were undertaken throughout the past three years:

Task I – Precision Table Top Elastic Modulus Measurement Systems

Development of computerized electro-mechanical systems for in-vitro elastic modulus measurement of breast tissue samples was undertaken during the first and second years. One device was designed to measure small tissue samples. This device was suitable for small homogeneous normal tissue samples obtained from breast reduction procedures. That device was later modified to make it useful for tumors in breast tissue slices obtained from lumpectomy or mastectomy procedures.

Task II – MR Compatible Phantom loading System

Development of an MR compatible instrument for loading phantoms was undertaken during the first year. This device was aimed at applying periodic

compression to block shape phantoms. While applying the compression, the resulting distribution of strain within the phantom was measured using MRI phase contrast technique.

Task III – MR Compatible breast loading System

Development of an MR compatible instrument for loading breasts or breast like phantoms was undertaken during the second year. This device was designed to apply periodic compression to breast like phantoms or breasts for in-vivo elastography.

Task IV – MR Compatible Tissue Sample loading System

Development of an MR compatible instrument for tissue elastic modulus measurement was undertaken during the second and third years. This device was aimed at applying periodic compression to breast tissue samples encased in calibrated gelatine-agarose blocks. While applying the compression, the resulting distribution of strain within the encased sample was measured using MRI phase contrast technique.

Task V – Elastography Inversion Techniques

Development of elastography inversion techniques was undertaken during the first and second years of this project. Two modulus reconstruction techniques based on continuum mechanics equations were developed that input the MRI derived displacement data of a tissue sample or breast undergoing quasi-static loading, and outputs the relative elastic moduli of different tissue components within the sample or breast. These techniques were studied and SNR requirements of each technique were assessed.

Task VI – Finite Element Meshing Techniques

Development of Finite Element (FE) meshing techniques was undertaken during the first year. FE meshing is the first and most tedious task in building FE models used in elastography and tissue deformation simulation models. Two meshing algorithms were developed to construct FE mesh of phantoms or breasts using MRI images.

Task VII – Breast Tissue Deformation Model

An important application of this research is predicting breast tissue deformation. Beside the fact that this model is used in our modulus reconstruction algorithm, it can be applied in many other medical applications such as breast image coregistration. A FE model that requires the biomechanical properties of breast tissues to predict tissue deformation was developed over the second year. This model is required as a forward model component of modulus reconstruction technique as well as to estimate breast tissue deformations required for biomechanics based image coregistration techniques[11].

Task VIII – Inversion Technique for Tissue slice Modulus Measurement

Due to the paramount importance of tumor margin identification, tumor dissection is generally not possible. As such, a modulus measurement technique was developed to accommodate this limitation. For this purpose, in parallel to modifying the table-top system, an iterative inversion technique was developed over the third year to determine the elastic modulus of tumors in breast slices.

Task IX – Breast Tissue Hyperelastic Parameters Reconstruction Model

Given their softness, normal breast tissues deform significantly. Predicting finite deformation of breast tissues is key to many medical applications such as image coregistration[11] and image guided surgery[12]. The FE model developed for this purpose

requires hyperelastic properties of breast tissues. As such, a nonlinear optimization inversion technique was developed over the third year to estimate the hyperelastic parameters from the force-deformation data obtained from the table-top system.

Task X – In-vitro Breast Tissue Elastic Modulus Measurement

Over the third year of this project, more than 120 samples of various normal and diseased breast tissues have been tested using the table-top electro-mechanical device to provide the data base required for elastography image interpretation. This activity is still ongoing.

KEY RESEARCH ACCOMPLISHMENTS

1) During the first year, we designed, configured, constructed, the computerized electro-mechanical table-top system to measure tissue elastic properties in-vitro[9,10]. Throughout the second year, this system has been tested, modified and integrated to provide both accurate measurements as well as conditions similar to those of in-vivo. This system is shown in ***Figure 1*** and it allows for table-top uniaxial loading experiments under a broad range of frequencies and amplitudes. This system consists of two main components: a linear stepper motor actuator used to deform the tissue sample in a programmable fashion and a load cell for force measurement. The applied tissue deformation is measured based on the motion delivered by the actuator, while measuring the resulting force dynamically with the load cell. The actuator and load cell are wired to a computer that gives instructions to the actuator and receives data from both the actuator and the load cell through LabView virtual instrument software. To provide conditions similar to those of in-vivo, tissue samples are kept moist by immersing them in an isotonic sodium chloride solution, and temperature is maintained at 37°c using a temperature control device. Based on the geometry and boundary conditions of the specimen, inversion models have been developed to estimate the elastic modulus of the tissue from the measured data. The measurement technique using unconstrained block shape tissue samples is described in Samani *et al.*[14].

2) Over the first year, we designed, configured and constructed an MR compatible system for controlled uniaxial loading of block shape phantoms in elastography experiments. As described in Plewes *et al.* 2000[15], this system, shown in ***Figure 2***, is driven by an ultrasound stepper motor under computer control which allows cyclic compression at variable frequencies from 0.1 to 1.5 Hz and and amplitudes from 0 to 5 mm. In conjunction with this system, an MRI pulse sequence using a stimulated echo acquisition method[15] was written and tested. This system was used to verify the validity of our developed FE models for tissue deformation prediction. This research which, was published as a paper[16], concludes that FE simulations of heterogeneous phantoms can accurately predict deformation given knowledge of constitutive properties of the phantom's materials.

3) For in-vivo breast tissue modulus reconstruction, a breast compression system shown in ***Figure 3*** has been designed and constructed over the second year. This system consists of a commercial MRI breast coil and two compression plates. One of these plates is stationary and the other is driven by an MR compatible stepper motor to compress the breast cyclically. This system was tested on a breast shaped phantom shown in ***Figure 4***. This figure shows a

sagittal MR image of this phantom with a preliminary coronal strain image of the phantom. Although encouraging, the strain image suggests that further improvement to the compression system is required to achieve better SNR.

4) For MRI elastic modulus measurement of ex-vivo breast tissues, an MR compatible loading device was designed and constructed over the third year. As described in Samani *et al.* 2002[9], a specimen encased in a block of gelatine-agarose is placed in the MR compatible loading system. While under cyclic compression, displacement data of a plane passing through the tissue specimen is acquired. Finally this data is used to obtain the elastic modulus of the tissue using our constrained elastography technique[7]. This method was validated using an adipose tissue specimen obtained from a 61 year old patient. The results obtained from this specimen using both this method and the table-top system method are reported in Samani *et al.* 2002[9] which indicates a good agreement.

5) During the first year of this project, in conjunction with the MR compatible loading systems, a direct inversion algorithm based on Navier equations was developed for tissue modulus reconstruction. To achieve a reasonable reconstruction results, however, very high SNR values are required which are very difficult to obtain in practice. The results of this research are published in Bishop *et al.* 2000[17]. As an alternative, we have developed an iterative constrained modulus reconstruction technique with moderate SNR requirement. This technique has been tested on a multi-component phantom with a 3-D complex geometry and the results indicate that the reconstruction algorithm is reasonably accurate and robust. ***Figure 5*** depicts the phantom's geometry and the modulus reconstruction results obtained from this technique. A paper outlining the mathematics and results of this technique has been published in Samani *et al.* 2001[7]. This paper suggests that very moderate SNR values are required for reasonably accurate modulus reconstruction.

6) Two FE meshing techniques were developed over the first year. These techniques input segmented MRI images of the breast to create 3D patient specific FE mesh taking into account adipose, fibrous, tumor and skin tissues. One of the meshing techniques is voxel based and leads to abrupt surfaces and tissue interfaces while the other is based on mathematical mapping algorithms and leads to smooth surfaces and tissue interfaces. The details of these methods are published in Samani *et al.* 2001[11].

7) Breast tissue deformation model was developed over the second year using the FE method. Tissue deformation modeling is a very important for this research project as it is the primary component of our constrained elasticity reconstruction technique. As such, in parallel to the modulus reconstruction technique, we have developed 3-D FE model that uses breast MRI images and tissue mechanical properties as an input and calculates tissue deformation and stress distribution as an output. This model is capable of predicting both small deformation as in the case of breast elastography as well as large deformation as required in other applications such as image coregistration. The latter requires the a knowledge of breast tissue hyperelastic parameters. The details of this model and its application in breast image coregistrationis are published in Samani *et al* 2001[11].

8) Excising breast tissue into a block-shape specimen, especially with small tumors, is often not possible as it may lead to insurmountable difficulties in determining the tumor's margin by pathologists. As such, we devised a novel technique over the third year by which excising the tissue is unnecessary and tissue slices coming from mastectomy or lumpectomy would remain intact. In this technique, the area of interest e.g. tumor is similarly indented using a slightly modified table-top system shown in ***Figure 6***. The resulting force-deformation is used to determine the elastic modulus of the indented tissue via an iterative inversion technique. This inversion technique is summarized in ***Figure 7***. As indicated in this figure, areas of various tissues are determined via segmenting a digital photo taken prior to the indentation test. The segmented image is then processed to obtain a slice specific FE mesh required for the inversion technique. ***Figure 8*** depicts a breast tissue slice obtained from a lumpectomy procedure along with its corresponding segmented image and FE mesh. So far over 120 various breast tissue specimens have been tested and the average Young's moduli of over 80 specimens are reported in ***Table 1***. The details of this methodology and measurement results will be submitted as a paper[18] in the near future.

9) While elastic moduli of breast tissues can be used in FE models where small tissue deformation, e.g. elastography, is involved, there are many medical applications where breast tissue undergoes large deformation. For example continuum mechanics based breast image coregistration[11] and image guided surgery[11] models require accurate hyperelastic parameters in order to be used reliably for clinical purposes. As such, we have developed a nonlinear optimization technique over the third year to estimate the hyperelastic parameters of breast tissues. The experimental set up for this measurement technique is the same as the one used for the elastic modulus measurement. However, the inversion technique used to infer the hyperelastic parameters from the force-displacement data is based on a nonlinear optimization technique. In this technique a nonlinear FE model is used that calculates the required indentation forces given the appropriate indentation boundary conditions. Thus, the nonlinear optimization inversion technique calculates the set of hyperelastic parameters that minimize the difference between the measured and calculated indentation forces. This technique was applied to estimate the hyperelastic parameters of an adipose tissue obtained from a patient who underwent a breast reduction. A small block of the tissue was excised and placed in the table-top system. A cyclic indentation of 1-mm amplitude was applied and corresponding force-displacement data was recorded. Assuming a second order polynomial strain energy potential function, 5 hyperelastic parameters have to be identified. The results obtained from this technique are shown in ***Table 2*** and the corresponding force-displacement curve is shown in ***Figure 9*** that indicates a good agreement. The details of this technique, results and applications will be submitted as a paper[19].

10) Over 120 specimens of various breast tissues both normal tissues and tumors have been tested using our table-top measurement system since the beginning of the third year. The specimens include both block shape samples and slices. The elastic modulus results of these in-vitro measurements will be compiled and form part of a paper[18] to be submitted in the near future.

REPORTABLE OUTCOMES

Since the beginning of this research project, we have published a number of papers and symposium abstracts, as detailed below, which relate to the research contained in this project.

PUBLISHED OR SUBMITTED PEER REVIEWED PAPERS:

1) Samani A, Bishop J and Plewes DB. Measuring the Elastic Modulus of Ex-vivo Small Breast Tissue Samples. Submitted to the Physics in Medicine and Biology, 2003.
2) Samani A, Zubovits J and Plewes DB. An Inverse Problem Solution for Measurin the Elastic Modulus of Ex-vivo Inhomogeneous Breast Tissue Slices. To be submitted.
3) Samani A and Plewes DB. Measuring the Hyperelastic Properties of Ex-vivo Breast Tissue Samples. To be submitted.
4) Sciarretta J, Samani A, Bishop J and Plewes DB. MR Validation of Soft Tissue Mimicking Phantom Deformation as Modeled by Nonlinear Finite Element Analysis. Medical Physics, **29**(1):65-72, 2002.
5) Samani A, Bishop J, Yaffe MJ and Plewes DB. Biomechanical 3-D finite Element Modeling of the Human Breast Using MRI Data. IEEE Transactions on Medical Imaging 20(4):271-279, 2001.
6) Samani A, Bishop J and Plewes DB. A Constrained Modulus Reconstruction Technique for Breast Cancer Assessmant. IEEE Transactions on Medical Imaging, vol. 20(9):877-885, 2001.
7) Bishop J, Samani A, Sciarretta J, Luginbhul C and Plewes DB. A Signal/Noise Analysis of Quasi-static MR Elastography. IEEE Transactions on Medical Imaging, 20(11):1183-1187, 2001.
8) Plewes DB, Bishop J, Samani A and Sciarretta J. Visualization and Quantification of Breast Cancer Biomechanical Properties with Magnetic Resonance Elastography. Phys. Med. Biol. **45**:1591-1610, 2000.
9) Bishop J, Samani A, Sciarretta J and Plewes DB. Two-dimensional MR Elastography: Methodology and Noise Analysis. Phys. Med. Biol. **45**:2081-2091, 2000.

PUBLISHED PEER REVIEWED ABSTRACTS AND CONFERENCE PAPERS:

1) Samani A, Sack I and Plewes D. Constrained Non-linear Elasticity Reconstruction Technique for Breast MRI Elastography. Submitted to the International Society for Magnetic Resonance in Medicine: Eleventh Annual Meeting, 2003.
2) Samani A and Plewes D B. Finite Element Model for MRI Image Updating for Breast Surgery. Computational and Numerical Modeling for Image-guided Therapy and Surgery Workshop, Toronto, December 13, 2002.
3) Samani A and Plewes D. In-vitro Breast Tissue Elastic Modulus Measurement Using Uniaxial Indentation Technique. Proceedings of the First International Conference on the Ultrasonic Measurement and Imaging of Tissue Elasticity, Niagara Falls, October 2002, Paper #69.
4) Samani A and Plewes D. Constrained Breast Elastography: Phantom Study and application in In-vitro Breast Tissue Measurement. Proceedings of the First

International Conference on the Ultrasonic Measurement and Imaging of Tissue Elasticity, October 2002, Paper #70.
5) A. Samani, C. Luginbuhl and DB Plewes. Measuring the Elastic and Hyperelastic Properties of Breast Tissue, Proceedings of the Department of Defense Breast Cancer Research Meeting, Orlando, September 2002,P24-17, 2002.
6) Samani A and Plewes D. Breast MRI Image Updating for Image Guided Surgery. 19th Annual Meeting of European Society for Magnetic Resonance in Medicine and Biology: Cann, August 2002, Paper #528.
7) Samani A, Luginbuhl C and Plewes DB. Magnetic Resonance Elastography Technique for Breast Tissue In-vitro Elasticity Measurement. Proceedings of the International Symposium on Biomedical Imaging:931-934, 2002.
8) Samani A, Bishop J and Plewes D. A Constrained Breast Magnetic Resonance Elastography Technique: 3D Phantom Study. International Society for Magnetic Resonance in Medicine: Ninth Annual Meeting, Glasgow, April 21-27, 2001, Paper#1640.
9) Samani A, Bishop J and Plewes D. 3D Finite Element Model for Breast Non Rigid Registration. International Society for Magnetic Resonance in Medicine: Ninth Annual Meeting, Glasgow, April 21-27, 2001, Paper#837.
10) Bishop A, Samani A and Plewes D. A Signal/Noise Analysis of Magnetic Resonance Strain Imaging. International Society for Magnetic Resonance in Medicine: Nineth Annual Meeting, Glasgow, April 21-27, 2001, Paper#1646.
11) Bishop J, Samani A, Sciarretta J and Plewes DB. Use of Constraints to Produce Plane Strain Conditions for MR Elastography. International Society for Magnetic Resonance in Medicine: Eighth Scientific Meeting, Denver, April 2000, Paper #1735.
12) Samani A, Bishop J, Sciarretta J and Plewes DB. Breast Magnetic Resonance Elastography: A New Reconstruction Technique Using MRI Derived Constraints. International Society for Magnetic Resonance in Medicine: Eighth Scientific Meeting, Denver, April 2000, Paper #2174.
13) Samani A, Bishop J, Sciarretta J and Plewes DB. Automated Three Dimensional Finite Element Mesh Generation Technique for Patient-specific Breast Using MRI Data. International Society for Magnetic Resonance in Medicine: Eighth Scientific Meeting, Denver, April 2000, Paper #2175.
14) Samani A, Bishop J, Ramsay E and Plewes DB. Breast Tissue Deformation Finite Element Modeling for MR/X-ray Mammography Data Fusion. Proceedings of the Fifth International Workshop on Digital Mammography, Toronto, June 2000, pp. 763-769.
15) Sciarretta J, Bishop J, Samani A and Plewes DB. MR Validation of Soft Tissue Deformation as Modeled by Non-linear Finite Element Analysis. International Society for Magnetic Resonance in Medicine: Seventh Scientific Meeting, Philadelphia, May 1999, Paper #246.
16) Bishop J, Samani A and Plewes DB. Pressure / Modulus Inversion for MR Elastography. International Society for Magnetic Resonance in Medicine: Seventh Scientific Meeting, Philadelphia, May 1999, Paper #2164.

DEGREES OBTAINED

Justin Siarretta: MSc 2000.

EMPLOYMENTS SUPPORTED BY THE AWARD

1. Abbas Samani: Research associate.
2. Jonathan Bishop: Post doctoral fellow.
3. Mohammad Abdel Bar: Co-op student.
4. Piragash Valamylum: Co-op student.
5. Erik Stutz: Co-op student.
6. David Hook: Co-op student.
7. Katayoon Rouhi: Co-op student.
8. Alizahra Chunara: Co-op student.

CONCLUSIONS

Over the past three years of this project, we have made good progress towards our end goal of understanding the biomechanical properties of breast tissues and developing the means to apply these in tissue deformation analyses. The overall objective of this project was to measure the biomechanical properties of various breast tissues, both normal as well as benign and neoplastic tissues for two purposes. One purpose was to obtain a breast tissue elasticity database required to interpret elastography images, and the other was to find tissue constitutive relations to create reliable mathematical tools to predict breast tissue deformation. To meet our research goals, we have used the hardware and software tools we have developed over the first two years. To measure the elastic properties of breast tissues, we developed MRI systems for small breast samples and breast elstography. While encouraging results were obtained, using the MRE system to measure elastic modulus of a large number of tissue samples proved to be impractical due to logistic issues. As a result our focus was shifted towards further developing and perfecting our table-top system which provided accurate and repeatable measurements. Using this system, we measured the elastic modulus of over 120 specimens of various breast tissues we obtained from pathology. The results of 80 specimens summarized in ***Table 1*** indicate that elastography provides sufficient contrast to aid in breast cancer diagnosis. A number of articles outlining the methodology and presenting the details and results of various components of this research have been published or submitted for publication over the past three years. After a careful processing and data statistical analysis of our over 120 specimens, a paper[18] will be submitted outlining the final results of this effort. Furthermore, another paper[19] presenting the details and results of our tissue hyperelastic properties system will be submitted in the near future. The importance of this work remains high providing a platform for new detection and diagnosis methods for breast cancer. This research can also open up new applications in breast imaging, including data fusion, and breast surgery based on the breast tissue hyperelastic parameters estimation and tissue deformation prediction techniques we developed over the second and third years of this project.

REFERENCES

1. Sarvazyan A, Goukassian D, Mavesky E and Oranskaja G. Elasticity Imaging as a New Modality of Medical Imaging for Cancer Detection. Proceeding of International Workshop on Interaction of Ultrasound with Biological Media, Valenciennes, France, 5-9 April 1994, pp 69-81.

2. Krouskop TA, Wheeler TM, Kallel F, Garra BS and Hall T. Elastic Moduli of Breast and Prostate Tissue Under Compression. Ultrasonic Imaging 20, 260-274, 1998.

3. Kruse SA, Smith JA, Lawrence AJ, Dresner MA, Manduca A, Greenleaf JF and Ehman RL. Tissue Characterization Using Magnetic Resonance Elastography: Preliminary Results. Physics in Medicine and Biology 45:1579-1590, 2000.

4. Sonderman E, Sinkus R, Morakkabati N, Leutner C, Reichel C and Kuhl C. MR-Elastographic Features of Benign and Malignant Breast Tumors. Proceedings of the ISMRM, Hawaii, pp. 33, 2002.

5. Plewes DB, Betty I, Urchuk S and Soutar I. Visualizing Tissue Compliance with MR. Journal of Magnetic Resonance Imaging 5(6):733-738, 1995.

6. Bishop JB, Poole G, Leitch M and Plewes DB. Magnetic Resonance Imaging of Shear Wave Propagation in Excised Tissue. Journal of Magnetic Resonance in Medicine 8:1257-1265, 1998.

7. Samani A, Bishop J and Plewes DB. A Constrained Modulus Reconstruction Technique for Breast Cancer Assessmant. IEEE Transactions on Medical Imaging 20(9):877-885, 2001.

8. Samani A, Sack I and Plewes D. Constrained Non-linear Elasticity Reconstruction Technique for Breast MRI Elastography. Submitted to the International Society for Magnetic Resonance in Medicine: Eleventh Annual Meeting, 2003.

9. Samani A, Luginbuhl C and Plewes DB. Magnetic Resonance Elastography Technique for Breast Tissue In-vitro Elasticity Measurement. Proceedings of the International Symposium on Biomedical Imaging:931-934, 2002.

10. Samani A and Plewes D. In-vitro Breast Tissue Elastic Modulus Measurement Using Uniaxial Indentation Technique. Proceedings of the 1st International Conference on the Ultrasonic Measurement and Imaging of Tissue Elasticity, Niagara Falls, pp. 69, October 2002.

11. Samani A, Bishop J, Yaffe MJ and Plewes DB. Biomechanical 3-D finite Element Modeling of the Human Breast Using MRI Data. IEEE Transactions on Medical Imaging 20(4):271-279, 2001.

12. Samani A and Plewes D B. Finite Element Model for MRI Image Updating for Breast Surgery. Computational and Numerical Modeling for Image-guided Therapy and Surgery Workshop, Toronto, December 13, 2002.

13. Samani A and Plewes D. Breast MRI Image Updating for Image Guided Surgery. 19th Annual Meeting of European Society for Magnetic Resonance in Medicine and Biology: Cann, August 2002, Paper #528.

14. Samani A, Bishop J and Plewes DB. Measuring the Elastic Modulus of Ex-vivo Small Breast Tissue Samples. Submitted to the Physics in Medicine and Biology, 2003.

15. Plewes DB, Bishop J, Samani A and Sciarretta J. Visualization and Quantification of Breast Cancer Biomechanical Properties with Magnetic Resonance Elastography. Phys. Med. Biol. **45**:1591-1610, 2000.

16. Sciarretta J, Samani A, Bishop J and Plewes DB. MR Validation of Soft Tissue Mimicking Phantom Deformation as Modeled by Nonlinear Finite Element Analysis. Medical Physics, **29**(1):65-72, 2002.

17. Bishop J, Samani A, Sciarretta J and Plewes DB. Two-dimensional MR Elastography: Methodology and Noise Analysis. Phys. Med. Biol. **45**:2081-2091, 2000.

18. Samani A, Zubovits J and Plewes DB. An Inverse Problem Solution for Measuring the Elastic Modulus of Ex-vivo Inhomogeneous Breast Tissue Slices. To be submitted.

19. Samani A and Plewes DB. Measuring the Hyperelastic Properties of Ex-vivo Breast Tissue Samples. To be submitted.

Appendix 1: Tables Figures of the body of the proposal

Table 1 A summary of the breast tissue measurement performed on over 80 specimens of various breast tissue types.

Adipose tissue	Fibroglandular tissue	Fibroadenoma	Carcinoma
1.94 ± 0.47	1.80 ± 0.40	4.82 ± 1.06	11.97 ± 2.77

Table 2 Hyperelastic parameters obtained for a breast adipose tissue specimen. A second order polynomial potential strain energy function was selected with 5 unknown coefficients that represent the hyperelastic parameters.

Init. Guess	0.00020	0.00020	0.00250	0.01500	0.00900
Calculated	0.00033	0.00028	0.00449	0.00772	0.00945

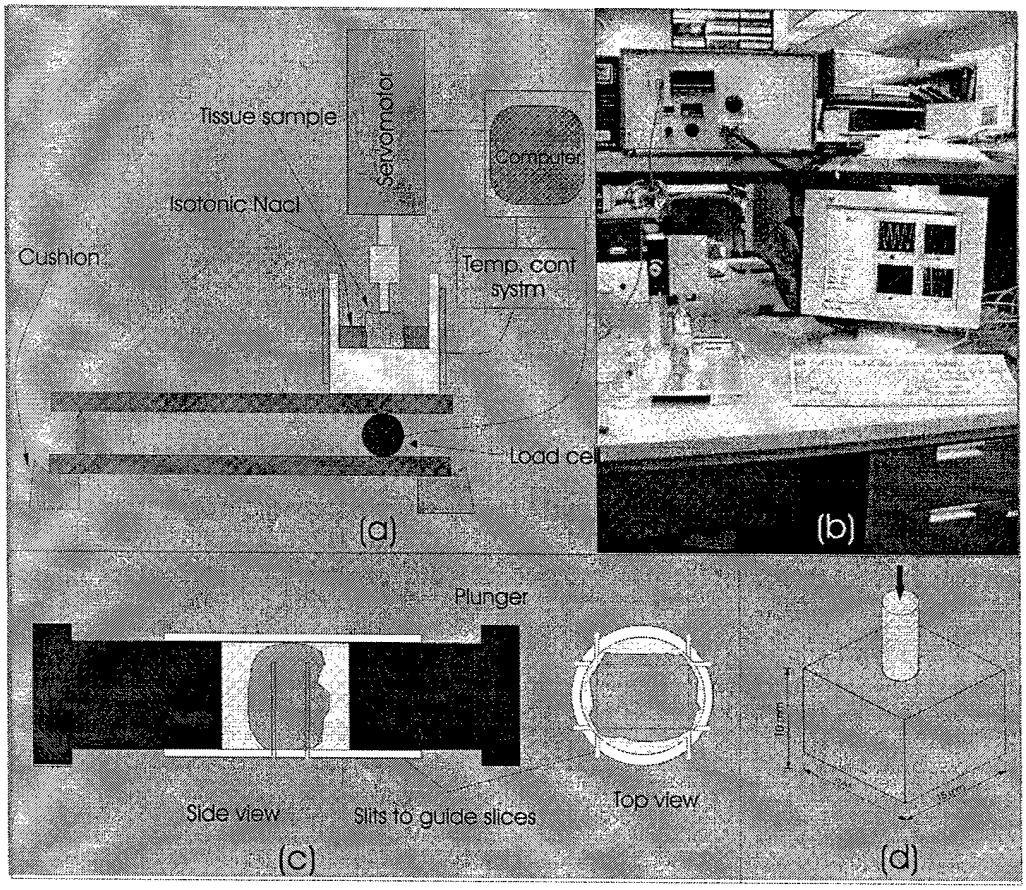

Figure 1. The unconstrained indentation system. a) schematic of the indentation experiment apparatus. b) photo of the indentation device. c) cutting device. d) ideal tissue sample prepared using the cutting device.

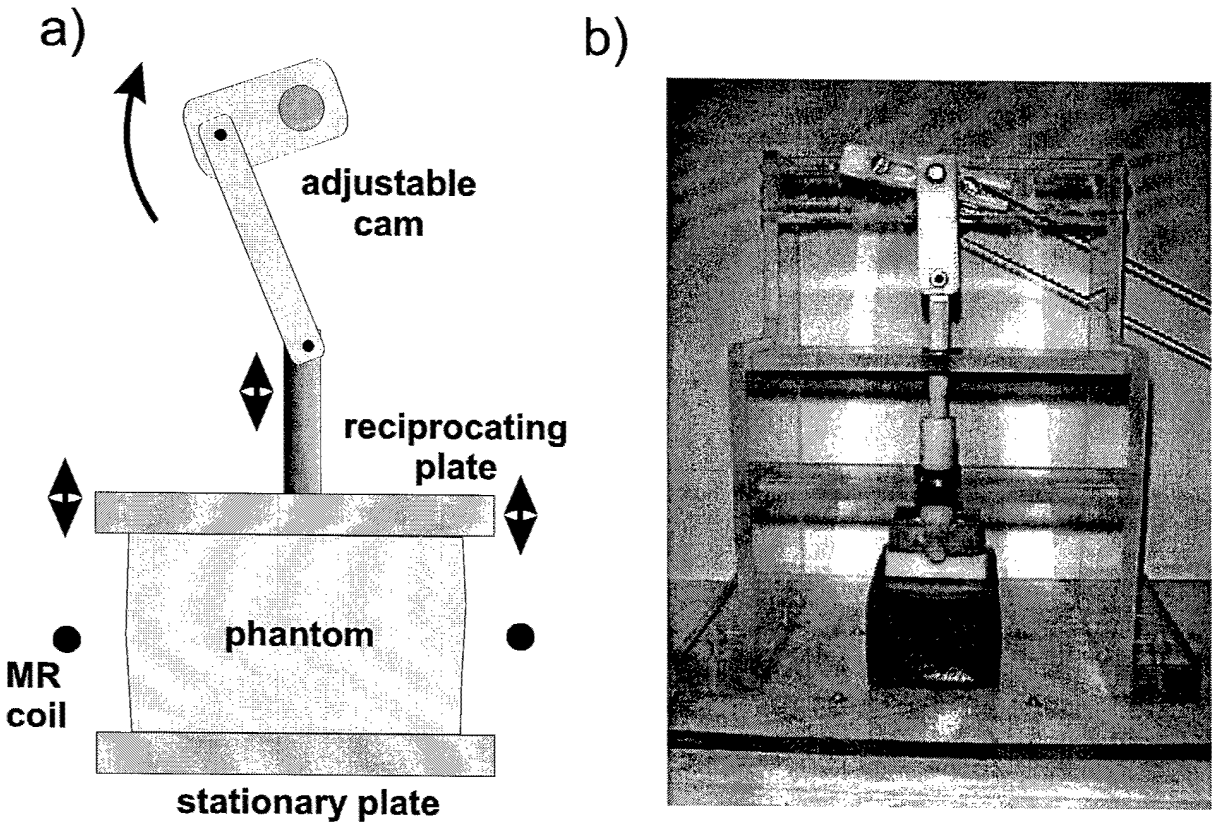

Figure 2. a) Schematic of the compression device for elastography phantom studies. b) photograph of the system.

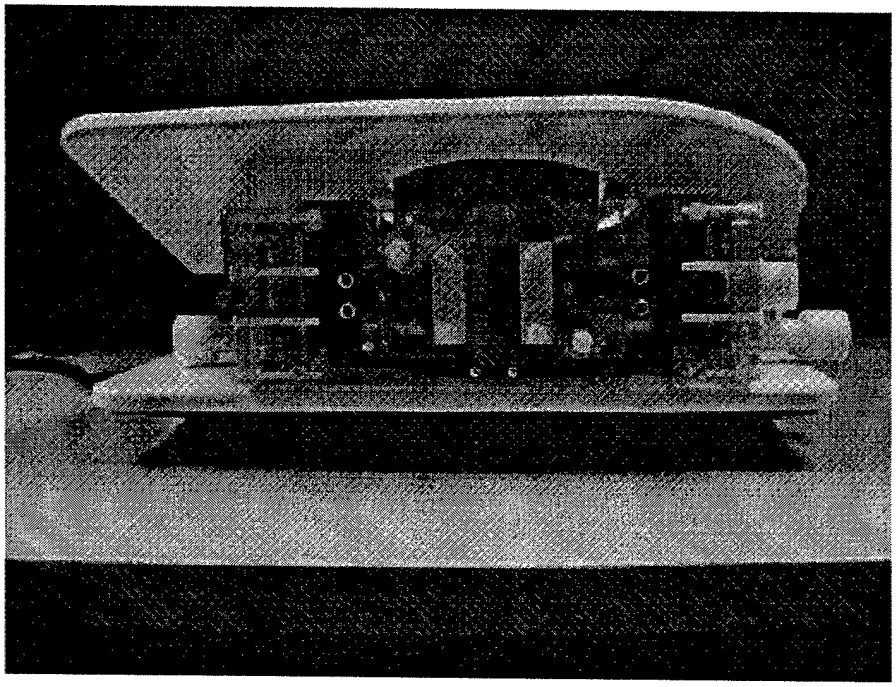

Figure 3. MRI compatible breast compression system used for MR elastograph of a breast-shaped phantom. This system consists of commercial breast coil and an assembly of plates and cams which deliver sinusoidal compression to the breast via an MR compatible stepper motor.

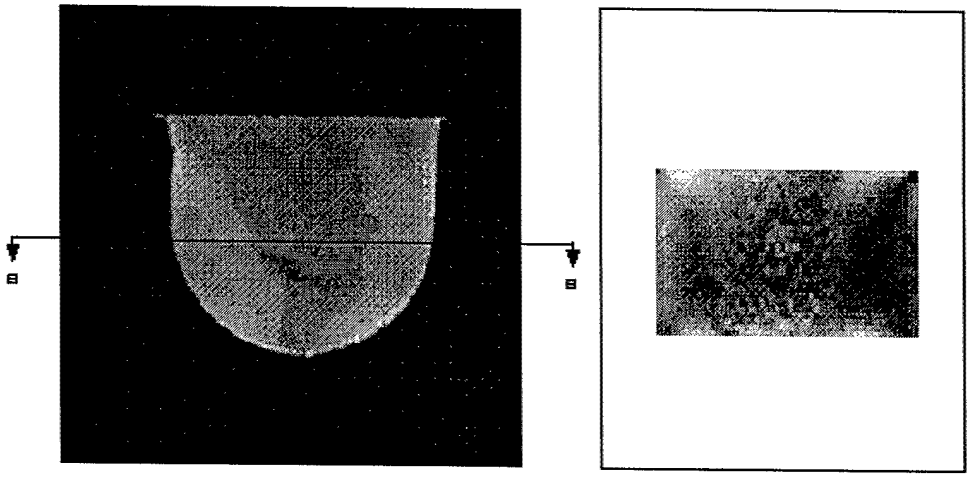

Figure 4. MRI sagittal image of the breast-shaped phantom (left) and a strain image a coronal slice corresponding to section a-a (right). Although the strain SNR is not satisfactory, different layers of the phantom are visible.

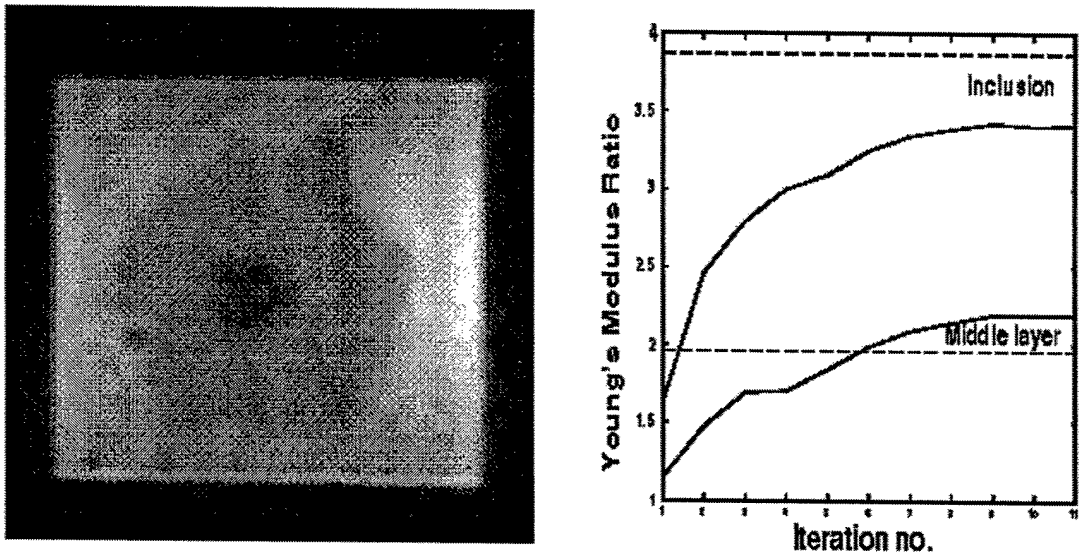

(a) (b)

Figure 5. a) MRI image of the multi-layer phantom. b) reconstruction results using the constrained reconstruction technique. The reconstruction results indicate a maximum error of 12% in reconstructing the modulus of different layers

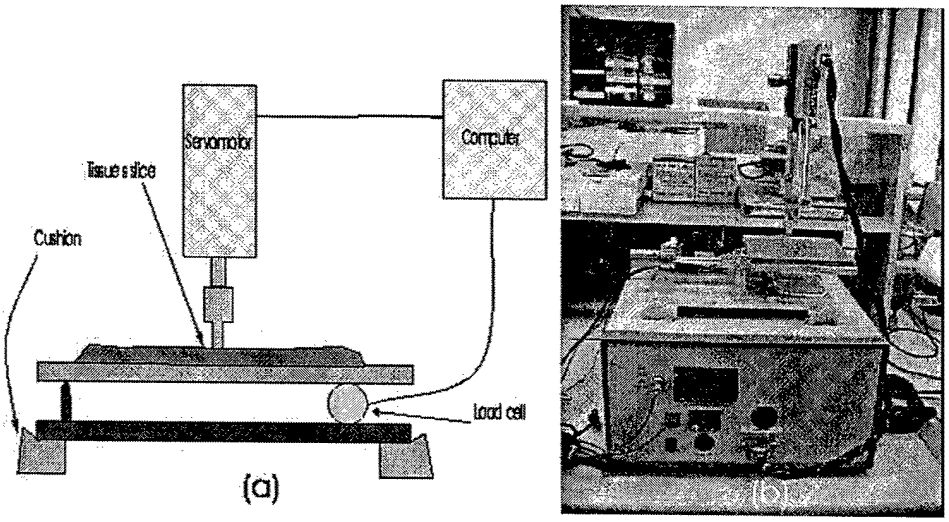

Figure 6. Electromechanical table-top measurement system for in-vitro tissue measurement. This system is designed primarily for small tumors in breast tissue slices obtained from lumpectomy or mastectomy. (a) shows a schematic of the modified system while a photo of the system is shown in (b). The system consists of two main component: a linear stepper motor actuator used to locally deform the tissue specimen in a programmable fashion and a load cell for force measurement.

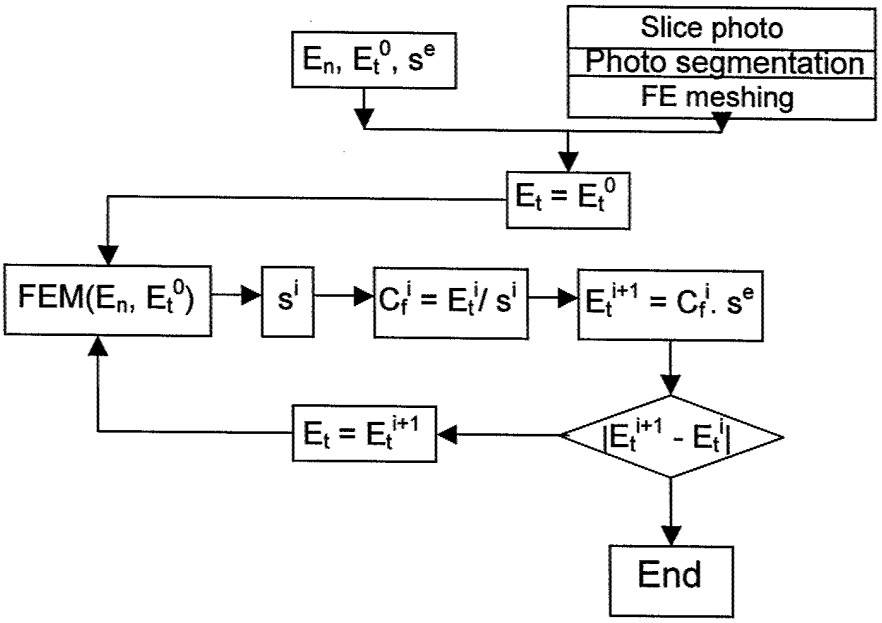

Figure 7. Flow chart of the the iterative inversion process required to calculate the elastic modulus of a small tumor in breast's slice. E_n represents the Young's modulus of the surrounding normal tissue, E_t^0 is the initial guess of the tumor's Young's modulus and s^e is the measured slope of the measured force vs, displacement in the uniaxial indentation test.

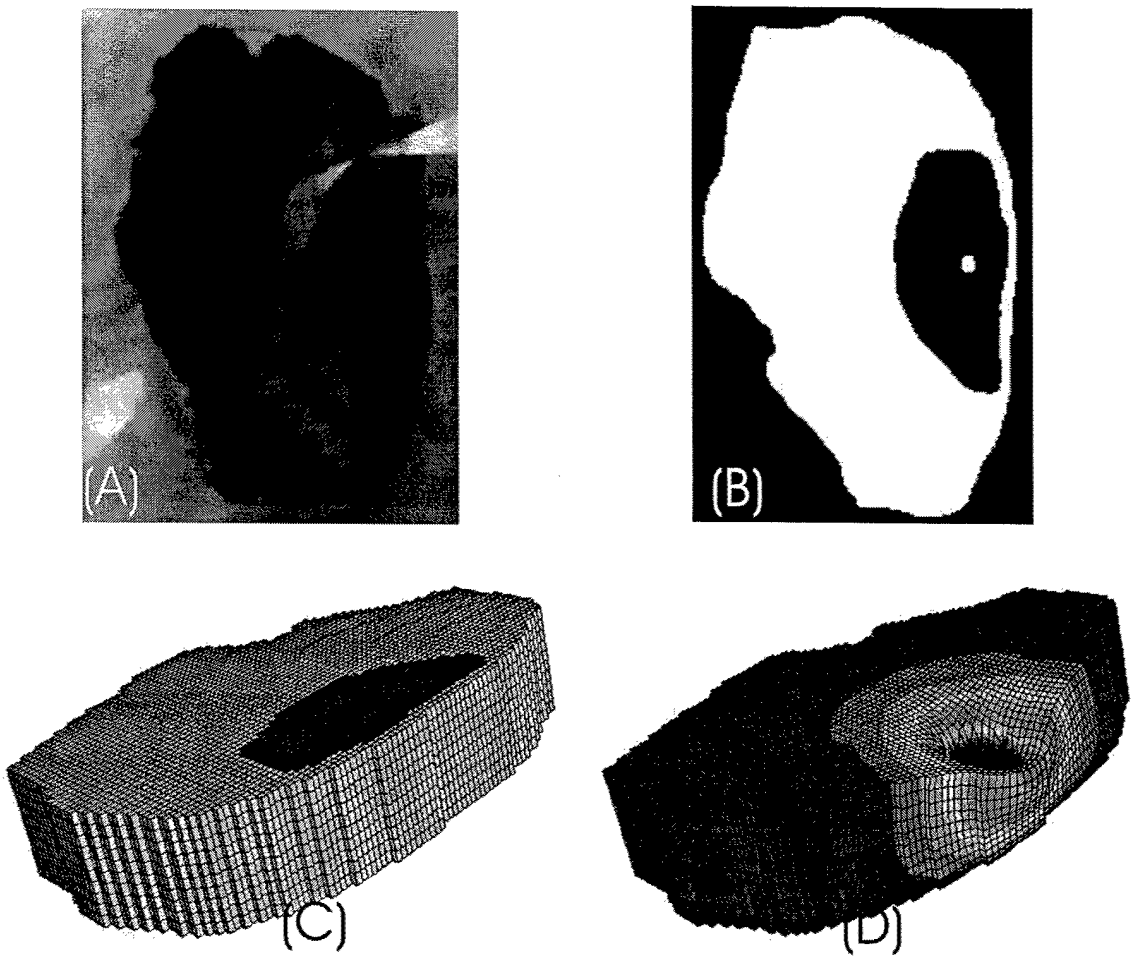

Figure 8. The process of building the FE mesh required for elastic modulus measurement using our novel inversion technique. A photo of a breast tissue slice with a tumor colored in red (A), corresponding segmented photo (B), FE mesh of the slice (C) and deformed FE mesh under indentation (D)

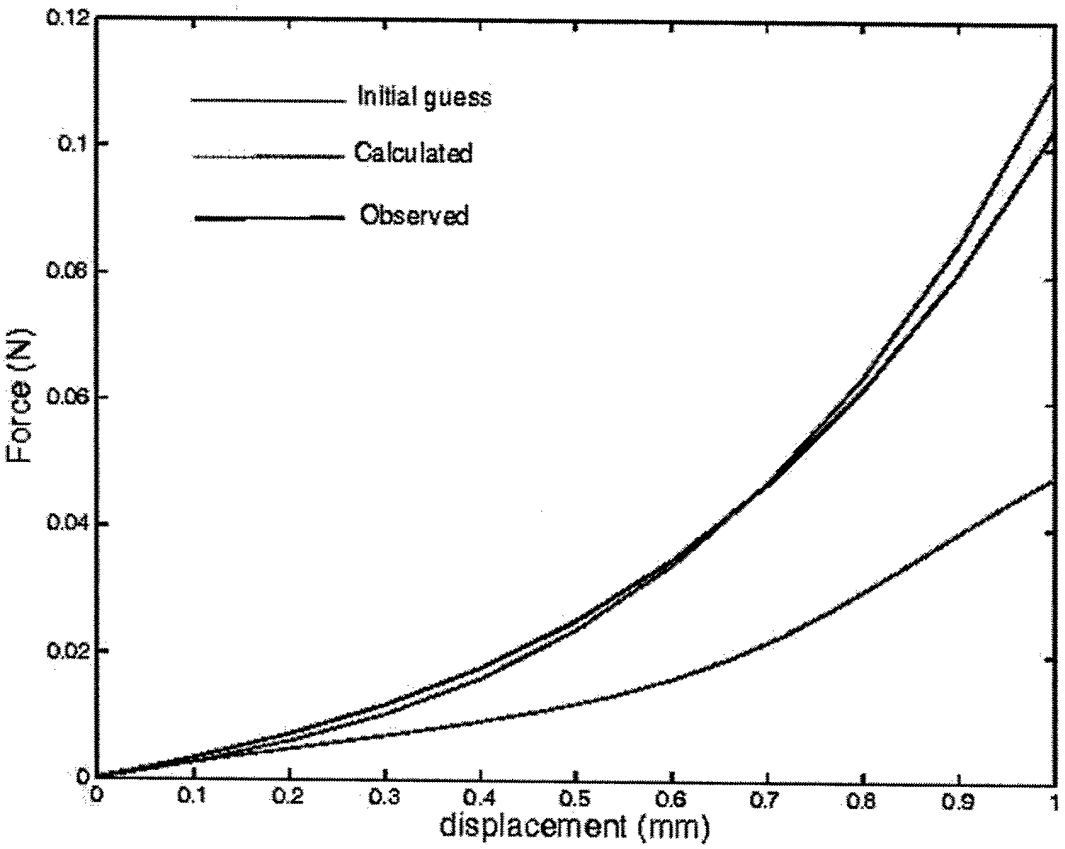

Figure 9. Experimental and calculated force vs. displacement curves obtained from the estimated hyperelastic parameters. The curve corresponding to the initial guess of the hyperelastic parameters is also shown to show the improved agreement between the experimental curve and that calculated based on the estimated parameters.

Appendix 2: Submitted abstract and paper

Abstract: Peer reviewed abstracts and conference papers listed in the reportable outcomes have been included in our previous annual reports. The following abstract which was submitted recently will be included in this report.

> Samani A, Sack I and Plewes D. Constrained Non-linear Elasticity Reconstruction Technique for Breast MRI Elastography. Submitted to the International Society for Magnetic Resonance in Medicine: Eleventh Annual Meeting, 2003.

Papers:

1) Samani A, Bishop J and Plewes DB. Measuring the Elastic Modulus of Ex-vivo Small Breast Tissue Samples. Submitted to the Physics in Medicine and Biology, 2003.
2) Sciarretta J, Samani A, Bishop J and Plewes DB. MR Validation of Soft Tissue Mimicking Phantom Deformation as Modeled by Nonlinear Finite Element Analysis. Medical Physics, **29**(1):65-72, 2002.
3) Samani A, Bishop J, Yaffe MJ and Plewes DB. Biomechanical 3-D finite Element Modeling of the Human Breast Using MRI Data. IEEE Transactions on Medical Imaging 20(4):271-279, 2001.
4) Samani A, Bishop J and Plewes DB. A Constrained Modulus Reconstruction Technique for Breast Cancer Assessmant. IEEE Transactions on Medical Imaging, vol. 20(9):877-885, 2001.
5) Bishop J, Samani A, Sciarretta J, Luginbhul C and Plewes DB. A Signal/Noise Analysis of Quasi-static MR Elastography. IEEE Transactions on Medical Imaging, 20(11):1183-1187, 2001.
6) Plewes DB, Bishop J, Samani A and Sciarretta J. Visualization and Quantification of Breast Cancer Biomechanical Properties with Magnetic Resonance Elastography. Phys. Med. Biol. **45**:1591-1610, 2000.
7) Bishop J, Samani A, Sciarretta J and Plewes DB. Two-dimensional MR Elastography: Methodology and Noise Analysis. Phys. Med. Biol. **45**:2081-2091, 2000.

Constrained Non-linear Elasticity Reconstruction Technique for Breast MRI Elastography

A. Samani[1], I. Sack[1], D. Plewes[1]

[1]University of Toronto, Sunnybrook and Women's College Health Sciences Centre, Toronto, Ontario, Canada

Synopsis To increase the displacement SNR in breast MR elastography, tissues are compressed significantly. As a result, breast tissues undergo large deformations. This leads to significant geometric and material nonlinearities. In this study, methods for treating these nonlinearities are presented and their impact on elasticity reconstruction is investigated. For elasticity reconstruction, a constrained elastography method is used where tissues are treated as hyperelastic materials. The tissue hyperelastic parameters are calculated using inversion techniques with a nonlinear finite element (FE) model for forward modeling. Simulations indicate the feasibility of reconstructing the tissue hyperelastic parameters using displacement data with moderate SNR.

Introduction Tissue elasticity alteration is well known to be associated with the presence of cancer. This has led to the development of elastography techniques for imaging tissue elasticity over the past decade. There are two MR elastography (MRE) methods: harmonic and quasi-static. In harmonic elastography, small amplitude harmonic actuation with frequencies ranging from 50-500 Hz is applied to deform the tissue whereas in quasi-static elastograpy, the tissue undergoes relatively large deformations with very low frequency. Large deformations increase the SNR of displacement, which lead to better quality of elasticity reconstruction. However, under large deformations, soft tissues become nonlinear. Beside geometric nonlinearity, breast tissues exhibit significant material nonlinearity under strains greater than 0.02 [1]. In our previous work, we have introduced a constrained reconstruction technique for breast MR elastography [2]. In that work, tissues are assumed to be linear elastic. The aim of this work is to extend our previous model by adding material and geometric nonlinearities. The purpose is two folds: to investigate the impact of these nonlinear effects on the reconstruction, and to explore ways of improving specificity based on the nonlinear parameters.

Methods As in [2], the breast elastography experiment is preceded by a contrast enhanced MRI imaging to obtain the geometry of each tissue type. Thus, a quasi-static sinusoidal compression is applied to the breast while resulting displacement data of the breast tissues are acquired using a stimulated echo (STEAM) pulse sequence [3]. The forward model in this reconstruction technique is a nonlinear Finite Element (FE) model of the breast, where breast tissues are assumed to be hyperelastic undergoing finite deformations. To obtain a constitutive model for hyperelastic materials, a strain energy function with a set of coefficients called the hyperelastic parameters is defined. The following expression represents a polynomial form widely used to represent strain energy functions:

$$U = \sum_{i+j=1}^{n} C_{ij}(I_1 - 3)^i (I_2 - 3)^j \qquad (1)$$

where C_{ij} represents the hyperelastic parameters and I_1 and I_2 are the strain invariants. With n=2, the above represents the Mooney Rivlin form widely used with incompressible materials. Following the principle in the constrained reconstruction [2], it is assumed that the C_{ij} parameters are uniform throughout the volume of each tissue type. Two methods are proposed to reconstruct the hyperelastic parameters. The first uses nonlinear optimization to calculate the set of C_{ij} parameters that minimizes the difference between the measured displacements and displacements calculated using the FE model. The other calculates C_{ij} using an iterative procedure where each iteration involves stress calculation using the FE model followed by C_{ij} parameters updating. For updating, the C_{ij} parameters are calculated for each finite element by solving a nonlinear constitutive equation derived from (1). The average of C_{ij} over the set of finite elements within each tissue will represent the updated hyperelastic parameters of the tissue.

Results For breast MRE, we used a volunteer's breast MRI image to create a 3D FE mesh. A sagittal slice of this mesh, where a simulated tumor is added, is depicted in Figure 1. Normal tissues are assumed to be Mooney Rivlin hyperelastic materials with C_{ij} parameters obtained in our lab [1]. The tumor is assumed to be linear elastic with a Young's modulus of 12.0 kPa which corresponds to an invasive carcinoma. The tumor's linear elasticity was assumed because of the relatively low strains the tumor undergoes as a result of its higher stiffness. According to these assumptions, displacements resulting from 5 mm compression normal to the breast's sagittal plane were calculated using a nonlinear contact FE model. The displacement component in the compression direction was contaminated by normally distributed noise to simulate an SNR value of 30. This displacement component was used with the optimization technique for tissue elasticity reconstruction. Starting with an arbitrary initial guess of C_{ij} parameters and a Young's modulus of 4.0 kPa, the hyperelastic parameters of the normal tissues and the tumor's Young's modulus were reconstructed. Figure 1 depicts the stress-strain curves of the true and reconstructed parameters, which indicate a very good agreement.

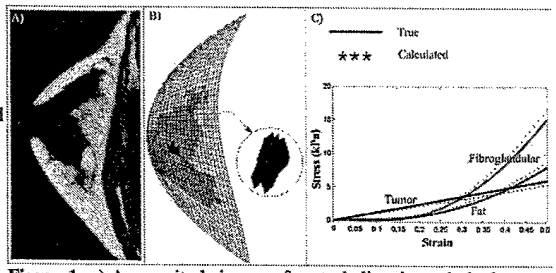

Figure 1: a) A magnitude image of central slice through the breast. b) FE mesh of the slice shown in (a) with a simulated tumor. c) true and reconstructed stress-strain curves of the fat, fibroglandular and tumor tissues.

Conclusions This article presents a constrained MRE technique, that can be potentially used to detect breast cancer. In this technique, quasi-static finite compression is assumed to be used for actuation. As such, large tissue deformation is expected which leads to significant material and geometric nonlinearities. To account for these nonlinearities, two inversion methods were proposed. The purpose of this work is two folds: to investigate the impact of these nonlinear effects on the elasticity reconstruction and to explore ways of improving specificity based on the nonlinear parameters. Due to the fact that breast tissues are highly nonlinear, conventional elastography methods, which assume linear elasticity, lead to elastograms that are dependent on the amount of applied compression. One advantage of hyperelastic parameter reconstruction is eliminating this dependence. The latter paves the way for reading elastograms in a consistent way. The presented breast elastography example, indicate that hyperelastic parameter reconstruction is possible with moderate SNR values. Further studies will be conducted using experimental displacement data.

References

[1] A. Samani, C. Luginbuhl and D. B. Plewes, ''Measuring the Elastic and Hyperelastic Properties of Breast Tissues'', *Department of Defense Breast Cancer Research Meeting* P24-17, 2002.

[2] D. B. Plewes, J. E. Bishop, A. Samani and J. Sciarretta, ''Visualization and Quantification of Breast Cancer Biomechanical Properties with Magnetic Resonance Elastography'', *Phys. Med. Biol.* **45**:1591-1610, 2000.

[3] T. L. Chenevert, A. R. Skovoroda, M. O'Donnell and S. Y. Emelianov, ''Elasticity Reconstructive Imaging by Means of Simulated Echo MRI'', *Magn Reson. Med.*39:482-490, 1998.

Measuring the Elastic Modulus of *Ex-vivo* Small Tissue Samples

Abbas Samani[(1)], Jonathan Bishop[(2)] and Donald B. Plewes[(1)]

[(1)]Dept. of Medical Biophysics, University of Toronto, 2075 Bayview Ave., Toronto, Ontario, Canada M4N 3M5

[(2)]Mouse Imaging Centre, Hospital for Sick Children, 555 University Avenue, Toronto, Ontario, Canada M5G 1X8

Submitted to: *Physics in Medicine and Biology*

Address correspondence to:
Abbas Samani, PhD
Department of Medical Biophysics
Imaging/Bioengineering Research Group
Sunnybrook and Women's College Health Sciences Centre
2075 Bayview Avenue, Toronto, Ontario, Canada M4N 3M5
phone: (416)480-6100, Ext. 3267
fax: (416)480-5714
e-mail: asamani@sten.sunnybrook.utoronto.ca

1. Abstract

Elastograhy techniques have been developed over the past decade to image tissue elasticity. To interpret elastography images, it is necessary to know the elastic properties of normal and abnormal tissues. A system was developed to measure the Young's modulus of small soft tissue specimens. This system was designed to accommodate biological soft tissue constraints such as sample size, geometry imperfection and heterogeneity. The measurement technique consists of indenting an unconfined small block of tissue while measuring the resulting force simultaneously. In this paper, it is proven that the measured force-displacement slope can be transformed to the tissue Young's modulus via a conversion factor related to the sample's geometry and boundary conditions. Accordingly, to obtain the Young's modulus, the conversion factor was obtained using finite element modeling validated by experiments. Another measurement technique based on magnetic resonance elastography was also developed. In this technique, a tissue specimen encased in a gelatine-agarose block is compressed while resulting displacements are measured using a phase contrast MRI technique. The tissue Young's modulus is then reconstructed from the measured displacements using an inversion technique. Finally, preliminary elasticity measurement results of various breast tissues are presented and discussed.

Key words: Elasticity, Measurement, Elastography, Breast, Tissue.

2. Introduction

Mechanical properties of biological tissues have been a subject of interest in various medical applications. Based on the fact that many pathological processes alter tissue elasticity significantly, a new imaging technique, elastography, has been developed for imaging soft tissue elastic modulus [1, 2]. Recently, modeling soft tissue deformation has been incorporated in other medical imaging applications such as image coregistration [3, 4] and image guided surgery [5]. The reliability of such models is highly dependent on the accuracy of the measured tissue biomechanical parameters. In the context of elastography, elastic modulus images can be used as an effective tool for diagnosis provided that quantitative elastic moduli data of normal and various abnormal tissues are available. Moreover, having reliable data of tissue elastic modulus can be used in assessing the performance of developed elastography systems. The purpose of this paper is to introduce a measurement technique that can be used to measure biomechanical properties of breast tissues. Soft tissues are often assumed to be elastic, isotropic and incompressible. Given these assumptions, the linear response can be characterized by one parameter, the Young's modulus. A conventional approach to measure the Young's modulus of tissue samples is using a direct measurement technique where a cylindrical sample is deformed between two plates while the resulting forces are measured [6]. In this technique, both stress and strain can be considered uniform throughout the sample's volume, and the slope of the linear stress-strain curve portion will represent the Young's modulus. This approach can be used for muscle and liver tissues where excising a large homogeneous specimens is possible. With breast tissues, however, such specimens are very rare. To address this problem, indirect measurement methods were developed where small tissue samples can be tested. Krouskop *et al* 1998 [7] used a hydraulic servo Instron machine (Instron, Inc, Canton, MA) to apply low frequency sinusoidal indentation loading with thin breast tissue slices. The slices were modeled as semi-infinite elastic media under uniform load of a circular indenter for which a closed form solution is available. 142 normal tissue and tumor specimens were tested using various loading frequencies and precompression. It was concluded that while not very sensitive to differ-

ent loading frequencies, Young's modulus of various breast tissues increase $1-10$ folds with higher precompression levels. Erkamp *et al* 1998 [8] developed a system to measure the elastic Young's modulus of small tissue samples. In this system, a cylindrical sample was indented while it was attempted to fully constrain its sides boundaries using a mold and gelatine-agarose. The system consisted of a stepper motor for indentation and electronic scale for force measurement. To obtain the Young's modulus, the slope of force-displacement response was transformed to Young's modulus using a conversion factor. This factor was obtained experimentally and validated by finite element (FE) modeling. Preliminary results of canine kidney tissue were presented and reasonable reproducibility was concluded. While appealing, this method was found to be very difficult to apply in breast tissues. Due to high deformability of normal breast tissues, our attempts to cut the tissue into cylindrical samples were unsuccessful. Furthermore, fully constraining the side boundaries was found to be even more challenging. To adapt this system for breast tissue Young's modulus measurement, these difficulties must be addressed. In this paper, a system for accurate and repeatable measurement of small soft tissue specimens is presented. The method of Erkamp *et al* 1998 [8] was adapted while the said difficulties were addressed. To this end, instead of testing cylindrical samples, block shape samples were produced using a cutting technique developed for this purpose. Furthermore, to minimize boundary conditions uncertainties associated with constraining the sample's sides, it was decided to leave the sides unconstrained. To improve measurement accuracy, a measurement device was built using a computer controlled system consisting of a servo motor for tissue actuation and a load cell for force measurement in addition to a temperature control device to maintain tissue biological temperature. In addition, an FE based mathematical proof is provided for the linear relation required to transform the indentation force-deformation slope to the Young's modulus. Moreover, another tissue elasticity measurement technique based on magnetic resonance elastography (MRE) is presented where a small tissue specimen is encased in a gelatine-agarose block with known Young's modulus. Finally, preliminary results of the Young's modulus of various breast tissues will be presented and discussed.

3. Theory

A schematic of a linear elastic continuum is shown in Figure 1. This object is in an equilibrium state under a statically applied load P. As shown in this figure, P causes an elastic deformation Δ at the point of load application. For simplicity, Δ is considered to be in the same direction as P. FE modeling of the object leads to:

$$\mathbf{KU} = \mathbf{F} \tag{1}$$

where $\mathbf{K}$ is the stiffness matrix and $\mathbf{U}$ and $\mathbf{F}$ are the vectors of nodal displacements and applied forces respectively. For a homogeneous elastic object with a Young's modulus of E, this equation can be expressed as follows [9]:

$$E\begin{bmatrix} \bar{K}_{11} & \bar{K}_{12} & \cdots & \bar{K}_{1n} \\ & \bar{K}_{22} & \cdots & \bar{K}_{2n} \\ sym. & & \ddots & \vdots \\ & & & \bar{K}_{nn} \end{bmatrix} \begin{Bmatrix} U_1 \\ U_2 \\ \vdots \\ U_n \end{Bmatrix} = \begin{Bmatrix} F_1 \\ F_2 \\ \vdots \\ F_n \end{Bmatrix} \tag{2}$$

where n represents the number of degrees of freedom. For simplicity, we assume that $U_1 = \Delta$, thus:

$$E\begin{bmatrix} \bar{K}_{11} & \bar{K}_{12} & \cdots & \bar{K}_{1n} \\ & \bar{K}_{22} & \cdots & \bar{K}_{2n} \\ sym. & & \ddots & \vdots \\ & & & \bar{K}_{nn} \end{bmatrix} \begin{Bmatrix} \Delta \\ U_2 \\ \vdots \\ U_n \end{Bmatrix} = \begin{Bmatrix} P \\ 0 \\ \vdots \\ 0 \end{Bmatrix} \tag{3}$$

Lets assume that the inverse of the coefficients matrix $\bar{\mathbf{K}}$ can be expressed as follows:

$$\bar{\mathbf{K}}^{-1} = \begin{bmatrix} C_{11} & C_{12} & \cdots & C_{1n} \\ & C_{22} & \cdots & C_{2n} \\ sym. & & \ddots & \vdots \\ & & & C_{nn} \end{bmatrix} \tag{4}$$

From equations 3 and 4, it can be shown that:

$$\Delta = \frac{C_{11}}{E}P \Rightarrow E = C_{11}\frac{P}{\Delta} \tag{5}$$

$\frac{P}{\Delta}$ represents the force-displacement slope of loading. This means if a homogeneous tissue sample with an arbitrary geometry is indented, the force-displacement slope denoted by

s can be transformed to the tissue's Young's modulus E using the following equation:

$$E = \kappa s \tag{6}$$

where κ represents C_{11} in 4 which is clearly dependent on the object's geometry and boundary conditions.

4. Materials and Methods

4.1. Unconstrained Indentation Measurement System

To measure the Young's modulus of breast tissues, a system was developed that indents a small circular area on the top surface of a small tissue block while measuring resulting forces. The indenter's area was chosen small enough so as full contact with the sample's surface is maintained with a minimal preloading while large enough not to pierce the sample. Applying force on part of the top surface yields nonuniform stress and strain distribution. As a result a slope of stress-strain plot does not directly represent the Young's modulus. To obtain Young's modulus, equation 6 is used in which κ is estimated by FE modeling validated by calibrated samples.

Specimen preparation

Breast tissue samples obtained from breast reduction or mastectomy were provided. Relatively homogeneous specimens with a minimum size of $30 \times 30 \times 20$ mm were excised and immediately transported to our lab. To obtain $15 \times 15 \times 10$ mm block shape specimens for testing, a cutting system shown in Figure 2 was developed. This system consists of a plexi glass cylinder with orthogonal slits to guide the cutting blade for obtaining planar block sides. To prevent tissue deformation throughout the cutting process, the tissue specimen was embedded inside 2.5% agarose as shown in Figure 2. For this purpose the tissue was cut free hand to a size slightly larger than the desired $15 \times 15 \times 10$ mm size. This block was placed on top of a 10 mm layer of ~ 37°c agarose solution inside a small beaker. Next, the ~ 37°c agarose solution was poured slowly in the beaker until the tissue was submerged entirely. The agarose was then allowed to solidify for 10 minutes. One end of the cylindrical cutting device is sharp and capable of cutting through agarose without cracking its volume. This end was placed on top of

the encased tissue sample inside the beaker and pressed down through the agarose until the beaker's bottom is reached. After crushing the agarose around the cutting device, the cutting device containing the encased tissue specimen can be released. The cylinder prevents deformation in its radial direction. To prevent deformation in the longitudinal direction throughout the cutting process, as shown in Figure 2, the encasing agarose was constrained by two solid cylindrical pistons (plungers). One of the plungers has a longitudinal slit to guide the blade for cutting the tissue block sides. After constraining all sides of the encasing agarose, first the top and bottom surfaces were cut using the blade through the two parallel slits shown in Figure 2 and the then the four sides using the orthogonal slits. A photo of a block of adipose tissue obtained through this process is shown in Figure 2.

Experimental set-up

Indentation experiments of breast tissues were performed using a testing system shown in Figure 2. This system is a custom made computerized electro-mechanical machine which consists of a servo actuator with a controller for tissue actuation, load cell for force measurement and a temperature control system to maintain the tissue under biological temperature. The actuator is a linear servomotor LAL-30 (SMAC, Carlsbad, CA, USA) with a motion range of 25 mm. This actuator is controlled by a 6K2 motor controller (Parker Hannifin Corporation, Rhonert Park, CA, USA). The load cell is a LC601-5 (OMEGA ENGINEERING INC, Stamford, CT, USA) with a capacity of 5 lb. The temperature control component is a CSi32 (OMEGA ENGINEERING INC, Stamford, CT, USA). This unit is a bench top controller model set to maintain a temperature of 37°c to within ± 0.1°c. As depicted in Figure 2, the load cell is mounted underneath a pivoted solid platform which transports the tissue indentation force to the load cell. The actuation and force measurement systems are controlled by a single computer (PC) via a LabVIEW program. The servomotor is driven by the 6K2 controller through an RS232 serial port to receive LabVIEW program commands that specifies the actuation profile. For force data acquisition, the load cell signal is first amplified by an amplifier, then received by an NI 6020E analog input card (National Instruments, Austin, TX, USA) for digitization. The LabVIEW program is responsible for preloading the

tissue sample, evoking the servo motor for actuation using user input parameters of a predefined motion profile and finally it is responsible for force and displacement data acquisition. During the test, the tissue specimen is placed in a sample holder where it is surrounded by a thin layer of saline to maintain its moisture and biological temperature. The temperature control system, in addition to the CSi32 temperature feedback component, consists of a thermal element glued to the exterior sides of the sample holder and a small probe immersed in the saline. The apparatus is placed on sponge cushions to minimize force reading errors resulting from platform vibration.

Conversion factor determination

Equation 6 indicates that the conversion factor κ is not dependent on the Young's modulus. Only the sample geometry and boundary conditions influence this factor. This means that with the same geometry and boundary conditions, objects with arbitrary Young's moduli have the same conversion factor. Accordingly, two methods of conversion factor estimation were evaluated, one is experimental and the other is based on FE simulation. In the experimental method, homogeneous $15 \times 15 \times 10$ mm block shape samples were constructed from plastisol PVC (M-F Manufacturing Company, Fort Worth, TX) with different amounts of softener. To measure the Young's modulus of each sample, cylindrical samples with 7 mm radius and lengths of $60 - 85$ mm were constructed using the same plastisol patches. These samples underwent tensile uniaxial tests using the same indentation system. This system was slightly modified to stretch the cylindrical samples. The ends of these samples were glued to small unplasticized PVC (UPVC) disks attached to the actuator and load cell system. Each sample was first prestretched with 10 g force to ensure that it was fully straight. At that point, the piston was used as a reference point for deformation. Five cycles of sinusoidal stretching with a 2 mm amplitude and 0.1 Hz frequency was performed and linear force-displacement plots obtained. This experiment was performed twice for each sample and with the obtained force-displacement slope $\frac{F}{\Delta l}$, the sample's Young's modulus was calculated using the following relation:

$$E = \frac{l}{\pi r^2} \frac{F}{\Delta l} \tag{7}$$

where l and r are the length and radius of the cylindrical sample respectively. After the Young's modulus measurement, each $15 \times 15 \times 10$ mm block was placed in the sample holder as depicted in Figure 2, and using a 2.5 mm radius indenter, 5 sinusoidal cycles of indentation with 0.5 mm amplitude and 0.1 Hz frequency were applied. The slope of force-displacement curves s was found, and since the samples' Young's moduli are known from the previous experiment, the conversion factor can be determined using equation 6.

To determine the conversion factor using FE modeling, the indentation test of a $15 \times 15 \times 10$ mm block with an arbitrary Young's modulus was simulated with the FE technique. In this simulation, a 3-D FE mesh was created and a static loading corresponding to 1.0 indentation with a 2.5 mm radius indenter was simulated. Slipping boundary conditions were assumed at the indenter's contact area and the bottom. Figure 3 depicts the resulting deformed shape of the block's FE model. Similar to the experimental technique, the force-displacement slope was obtained and the conversion factor calculated using equation 6.

Testing protocol

After excising the tissue specimen, it is transformed to the elasticity measurement lab within two hours after the surgery. The specimen is excised and an approximately $15 \times 15 \times 10$ mm block shape sample is obtained using the cutting technique discussed earlier. As a result of their own weight, the blocks dimensions often change slightly; therefore, the dimensions are measured and recorded after the tissue is cut and prepared for testing. The tissue block is inspected for having gross inhomogeneity and possible macro tears that render the specimen inappropriate for elasticity measurement. To test the tissue block, it is placed in the sample holder where a thin layer of saline is poured to maintain moisture and biological temperature. The indenter is then lowered until it is nearly in contact with the sample's top surface. At this point, the LabVIEW program is executed after setting parameters such as preload, number of sinusoidal cycles, amplitude and frequency. The purpose of preloading is to establish a full contact between the indenter and the sample's top surface and it is chosen to be $0.5 - 2.0$ g depending on the surface smoothness and tissue stiffness. The amplitude is set to 0.5

mm and frequency to $0.02-0.1$ Hz to provide static loading conditions. Before gathering force-displacement data, the number of cycles is set to 25 for tissue preconditioning [10]. After preconditioning and reaching biological temperature, the number of cycles is set to 5 for which force-displacement data is acquired. This test is repeated 4 times where the sample is rotated and allowed to relax for a few minutes prior to the next test. After the measurement, the tissue sample is sent for histology to identify the tissue type.

4.2. MRE Measurement Technique

This technique is based on the constrained MRE technique described in [4] which assumes that the geometry of the encased tissue is known from a MRI image. The technique uses quasi-static actuation, measures resulting displacement in a single slice using a STEAM sequence [11] and finally calculates the Young's modulus of each tissue using an iterative reconstruction procedure [4]. To implement this technique in the context of breast tissue modulus measurement, a piece of tissue is first dissected and encased in a block of 4% gelatine and 1.5% agarose mixture. To encase the tissue, a $30 \times 30 \times 40$ mm mold is made. About half of the mold is filled with the gelatine-agarose mixture while it is still liquid. The mixture is then allowed to solidify, after which the tissue is placed on its top surface and the rest of the mold is then filled with the mixture. Encasing the tissue sample takes place while the mixture is $\sim$ 37°c to prevent any damage or alteration to the tissue elasticity while the mixture is still liquid. After solidifying, a small block of this mixture, which was cast simultaneously, undergoes a uniaxial test to measure its elasticity modulus. In the meantime the encased tissue undergoes an MRE experiment where a quasi-static sinusoidal compression of 1.5 mm is applied at the surface using an MR compatible device illustrated in Figure 4. In this device, the block is placed inside a birdcage coil. This is a low pass 16-rung coil with 50 mm diameter and 90 mm length tuned to 63.85 MHz and 50Ω . This coil was constructed from etched printed circuit board ($40\mu m$ copper thickness) and ceramic capacitors. The block is compressed by a piston driven by a shaft connected to a rotating eccentric disk driven by an ultrasonic MR compatible motor (USR60-N4, Shinsei Corp, Tokyo, Japan). Prior to compression, MRI images of the block are acquired for FE modeling.

The block is then compressed and displacements of a single slice measured using a STEAM sequence. To obtain the elasticity ratio of the tissue sample to the gelatine-agar, the displacement data is processed using the MRE technique. This procedure is iterative and consists of stress calculation followed by elasticity modulus updating. Finally, the tissue elasticity is obtained from the calculated ratio and the gelatine-agar modulus known from a uniaxial compression test.

5. Results

Six pairs of plastisol $15 \times 15 \times 10$ mm blocks and cylindrical samples with a radius of 7 mm were constructed using different amounts of softener to obtain various elastic moduli. Tensile uniaxial tests were performed to measure the Young's modulus of the cylindrical samples while indentation tests were performed on the block shape samples to obtain their force-displacement slopes. The results of these experiments are summarized in Table 1.

According to this table, the average κ is 133.5. In the mean time a FE model was developed to simulate the indentation experiment. A FE mesh for a $15 \times 15 \times 10$ mm block was constructed and the material was assumed to be incompressible ($\nu = 0.495$) with an arbitrary Young's modulus (E). A static loading corresponding to 1.0 mm indentation with a 2.5 mm radius indenter was simulated and the force-displacement slope obtained. This simulation led to a conversion factor κ of 138 which indicates a disagreement of only 3%. This disagreement is mainly due to the full slipping boundary conditions assumed at the sample's bottom and the indenter's contact area. The experiments indicate that this condition is closer to the theoretical full slipping condition with soft plastisol blocks. Since real breast tissues are very soft, a better agreement is expected. To demonstrate the performance of the indentation technique for breast tissue Young's modulus measurement, three tissue specimens were tested. Two specimens were obtained from a 61 and 41 year old breast reduction patients. After histology, these specimens were later identified as normal adipose and fibroglandular tissues respectively. The third specimen was dissected from a large ($\sim$ 8 cm) tumor obtained from a 42 year old patient who under went mastectomy. This was later confirmed to be a high grade

ductal carcinoma. These specimens were cut into 15 × 15 × 10 mm blocks and each was tested at least 4 times after preconditioning to make sure the measurements were repeatable. With a preload of 1 g and frequency of 0.1 Hz, force-displacement curves were obtained. The curve of the last cycle of these specimens are depicted in Figure 5.

As seen, these curves are nonlinear. To obtain the force-displacement slope required for Young's modulus calculation, the least squares linear fit of the data corresponding to deformations less than 0.2 mm was obtained for each curve. Each calculated slope was then transformed to the tissue Young's modulus using a conversion factor of 138. The young's modulus results of the tested tissues are summarized in Table 2.

To demonstrate the performance of the MRE measurement technique, the adipose tissue specimen used in the indentation test was immediately encased in a 30 × 30 × 37 mm gelatine-agarose block as described earlier. Prior to the MRE experiment, the Young's modulus of the gelatine-agar was measured using a uniaxial test resulting in 12.2 kPa. To perform the MRE experiment, the encased tissue was placed inside the birdcage coil, slightly preloaded to ensure full contact between the compressing plates, and advanced inside the bore of a GE SIGNA 1.5 Tesla scanner (GE Medical Systems, Milwakee, WI, USA). Sagittal MRI images of the block were acquired using a 2-D spin-echo sequence with 256 × 128 resolution, 1 mm slice thickness, $TR/TE = 300/14$ ms and $FOV = 50$ mm. The block then underwent a sinusoidal compression of 1 Hz and a 1.5 mm amplitude. A STEAM pulse sequence with $TR/TE = 950/12$ ms and a mixing time T_m of 500 ms was used to acquire the displacement data of a central plane. The strain distribution obtained from these displacements and the corresponding magnitude image are shown in Figure 6. Starting with a Young's modulus of 1 kPa, as an initial guess, convergence was achieved after 5 iterations. As shown in Figure 6, the final reconstructed modulus is 6.7 kPa.

Figure 5(a) indicates that within the strain range of this experiment, the behavior of the adipose tissue is nonlinear . As such, using the best cubic polynomial fit of the last cycle's data, the tangential Young's modulus was evaluated at point E shown in Figure 5(a) resulting in 5.6 kPa. According to Figure 6(b), the strain in the adipose tissue region is slightly inhomogeneous and averages around 0.05. As such, it is reasonable to

compare the Young's modulus obtained from the MRE technique with that of point E. This comparison indicates a 16% disagreement.

6. Discussion and Conclusions

A system for breast tissue Young's modulus measurement was developed. In this system, small block shape tissue samples are indented while the sides are unconstrained. The Young's modulus measurement technique is based on an indirect method where the force-displacement indentation response is transformed to the tissue's Young's modulus via a theoretical relationship. A mathematical proof based on FE modeling was presented which indicates that the slope of the force displacement response is linearly related to the Young's modulus as seen in equation 6. In this equation, κ only depends on the geometry and boundary conditions of the sample. Two methods of estimating κ were presented, experimental and theoretical using FE modeling. In this system, attempts were made to provide *in-vivo* conditions using a temperature control system to maintain biological temperature and by placing the sample in a shallow bath of saline to preserve tissue moisture.

The FE simulation method agreed very well with the experiment and comparison indicates a disagreement of only 3%. This small disagreement is due to the insignificant uncertainty associated with slipping boundary conditions at the sample's bottom and indentation contact area used in the FE model. Erkamp *et al* 1998 [8] showed that slippage at the side boundary significantly increases the conversion factor. Controlling the side boundary slippage was found to be very difficult. As such, to avoid uncertainties associated with the resulting boundary conditions, it was decided to leave the side boundaries unconstrained. Calibration and tissue test results indicate that this system leads to highly repeatable measurements. Furthermore, with constrained cylindrical samples, FE analysis indicates that 20% error is produced as a result of 0.5 mm radius deviation [8]. FE modeling of unconstrained block shape samples, however, indicates only 1% error resulting from 0.5 mm deviation in the block's size. This implies that small geometry imperfection leads to insignificant conversion factor errors. Based on our experience, using the cutting technique presented earlier rarely results in more than 0.5

mm size deviation. Due to the accuracy and efficiency of FE modeling and its flexibility in modeling block shape samples with various dimensions, it is clear that the FE method of estimating the conversion factor is more practical compared to the experimental way of using calibrated samples.

The purpose of this research is to present a measurement technique that can be reliably used in measuring the Young's modulus of various breast tissues. These measurements can provide a foundation for the interpretation of elastography images. Figure 5 demonstrates that breast tissues are significantly nonlinear. The Young's modulus results of breast tissues presented in this article were found by fitting lines to the initial portion of force-displacement curves where the displacement is less than 0.2 mm. Furthermore, given the nonlinearity of the tissues, it can be concluded that the measured Young's modulus is sensitive to the amount of precompression. The amount of used precompression in such experiments is a very significant factor which must be consistent with the precompression levels used in elastography. For example, in MRE, very little precompression is usually used unlike with US breast elastography where the breast is compressed significantly while displacement data is acquired. In our measurements, very little precompression was applied. This kind of measurement protocol can provide a data base suitable for MRE image interpretation. The results obtained from such measurements can still be useful for other elastography modalities provided the tangential Young's modulus is estimated at points corresponding to the applied precompression in the elastography experiment.

In addition to the indentation measurement technique, a novel method to measure tissue Young's modulus using an MRE technique was also developed. With this method, it is possible to measure the Young's modulus of tissue samples with an arbitrary size and shape. Results obtained from this method indicate a good agreement with results obtained using the indentation technique.

Although the focus of this research is breast tissues, the presented technique can be applied for other soft tissues such as the prostate. The indentation measurement system will be used to measure the Young's modulus of a large number of breast tissue samples to obtain a reliable data base that can be used for MRE image interpretation. Figure 5

indicates that there is a significant clearance between the loading and unloading curves within a cycle. This indicates that viscosity effects are significant in breast tissues. Based on the force displacement data obtained from the indentation tests, it is possible to estimate tissue viscosity parameters via an inverse problem model.

References

[1] Ophir J, Cespedes I, Ponnekanti H, Yazdi Y, and Li X. Elastography: A quantitative method for imaging the elasticity of biological tissues. *Ultrasonic imaging* 1991; **13**:111–134.

[2] Muthupillai R, Lomas D. J, Rossman P. J, Greenleaf J. F, Manduca A, and Ehman R. L. Magnetic resonance elastography by direct visualization of acoustic strain waves. *Science* 1995; **269**:1854–1857.

[3] Hagemann A, Rohr K, Stiehl H. S, Spetzger U, and Gilsbach J. M. Biomechanical modeling of the human head for physically based, nonrigid image registration. *IEEE Transactions on Medical Imaging* 1999; **18**(10):875–884.

[4] Samani A, Bishop J. B, and Plewes D. B. A constrained modulus reconstruction technique for breast cancer assessment. *IEEE Trans. Med. Imag.* 2001; **20**(9):887–885.

[5] Miga M. I, Paulsen K. D, Lemery J. M, Eisner S. D, Hartov A, Kennedy F. E, and W R. D. Model-updated image guidance: Initial clinical experiences with gravity-induced brain deformation. *IEEE Transactions on Medical Imaging* 1999; **18**(10):866–874.

[6] Chen E. J, Novakofski J, Jenkins W. K, and O'Brian W. D. Young's modulus measurements of soft tissues with application to elasticity imaging. *IEEE Trans. Ultrason. Ferroelec. Freq. Contr.* 1996; **43**:191–194.

[7] Krouskop T. A, M W. T, Kallel F, Garra B. S, and Hall T. Elastic moduli of breast and prostate tissues under compression. *Ultrasonic Imaging* 2001; **20**:260–274.

[8] Erkamp R. Q, Wiggins P. W, Skovoroda A. R, Emelianov S. Y, and O'Donnel M. Measuring the elastic modulus of small tissue samples. *Ultrasonic Imaging* 1998; **20**:17–28.

[9] BATHE K.-J, "Finite Element Procedures in Engineering Analysis". Prentice Hall, Englewood Cliffs, NJ, 1996.

[10] FUNG Y. C, "Biomechanics. Mechanical Properties of Living Tissues". Springer, NY, 1981.

[11] Chenevert T. L, Skovoroda A. R, O'Donnell M, and Emelianov S. Y. Elasticity reconstructive imaging by means of stimulated echo MRI. *Magn. Reson. Med.* 1998; **39**:482–490.

Table 1: Experimental conversion factor κ results obtained using plastisol PVC material with different amounts of softener.

Table 2: Young's modulus results of three breast tissue types. These values were obtained using the indentation technique by averaging the results of at least four tests.

Figure 1: An elastic continuum under a point static load P.

Figure 2: The unconstrained indentation system. a) schematic of the indentation experiment apparatus. b) photo of the indentation apparatus. c) cutting device, d) photo of an adipose tissue sample prepared using the cutting device shown in c).

Figure 3: FE model of a block shape sample under indentation. The deformed shape of the sample under 1.0 mm indentation can be seen.

Figure 4: MRE compression apparatus. This apparatus applies a quasi-static sinusoidal compression to a soft block encasing the tissue placed in a birdcage coil to achieve high signal to noise ratio.

Figure 5: Force displacement curves of indentation tests obtained for a) adipose tissue, b) fibroglandular tissue and c) high grade ductal carcinoma samples. In a), the best cubic polynomial fit of the last cycle's points is shown.

Figure 6: MRE technique results. a) A sagittal image of a central slice of the encased breast adipose tissue. b) Measured strain in the same slice. The measured strain indicates that the adipose tissue undergoes an average compressional strain of 0.05. c) Graph of the tissue Young's modulus iterative calculation.

Table 1

sample no.	cylindrical sample height (mm)	Young's modulus (E)	$\kappa = \frac{E}{s}$
1	70	181.1	128
2	70	182	129
3	85	41	136
4	60	40	135
5	60	40	136
6	60	40	137

Table 2

	adipose tissue	fibroglandular tissue	high grade ductal carcinoma
s (N/m)	10.3	16.5	58.9
E (kPa)	1.4	2.3	8.1

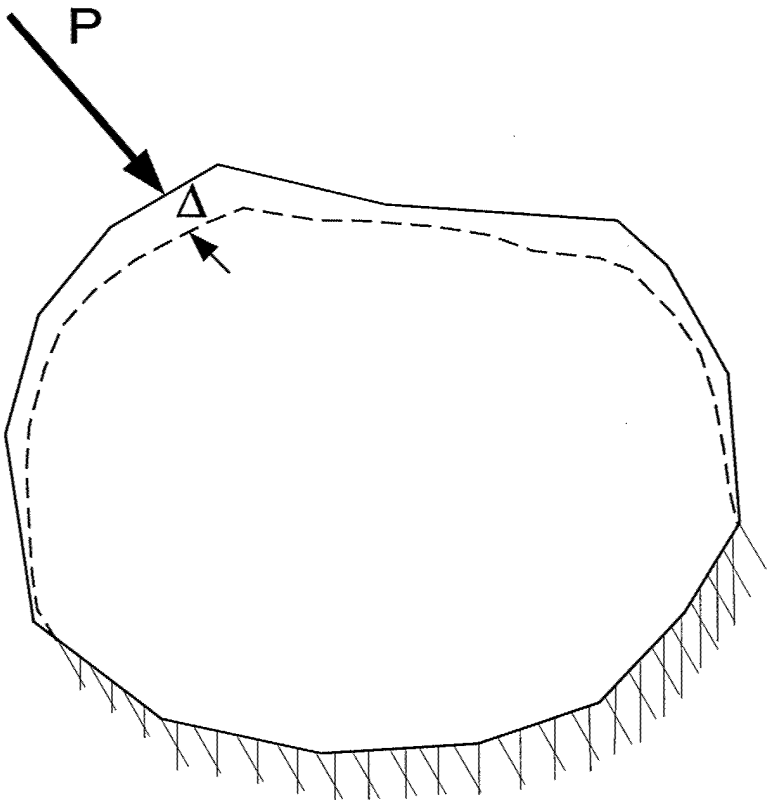

Figure 1.

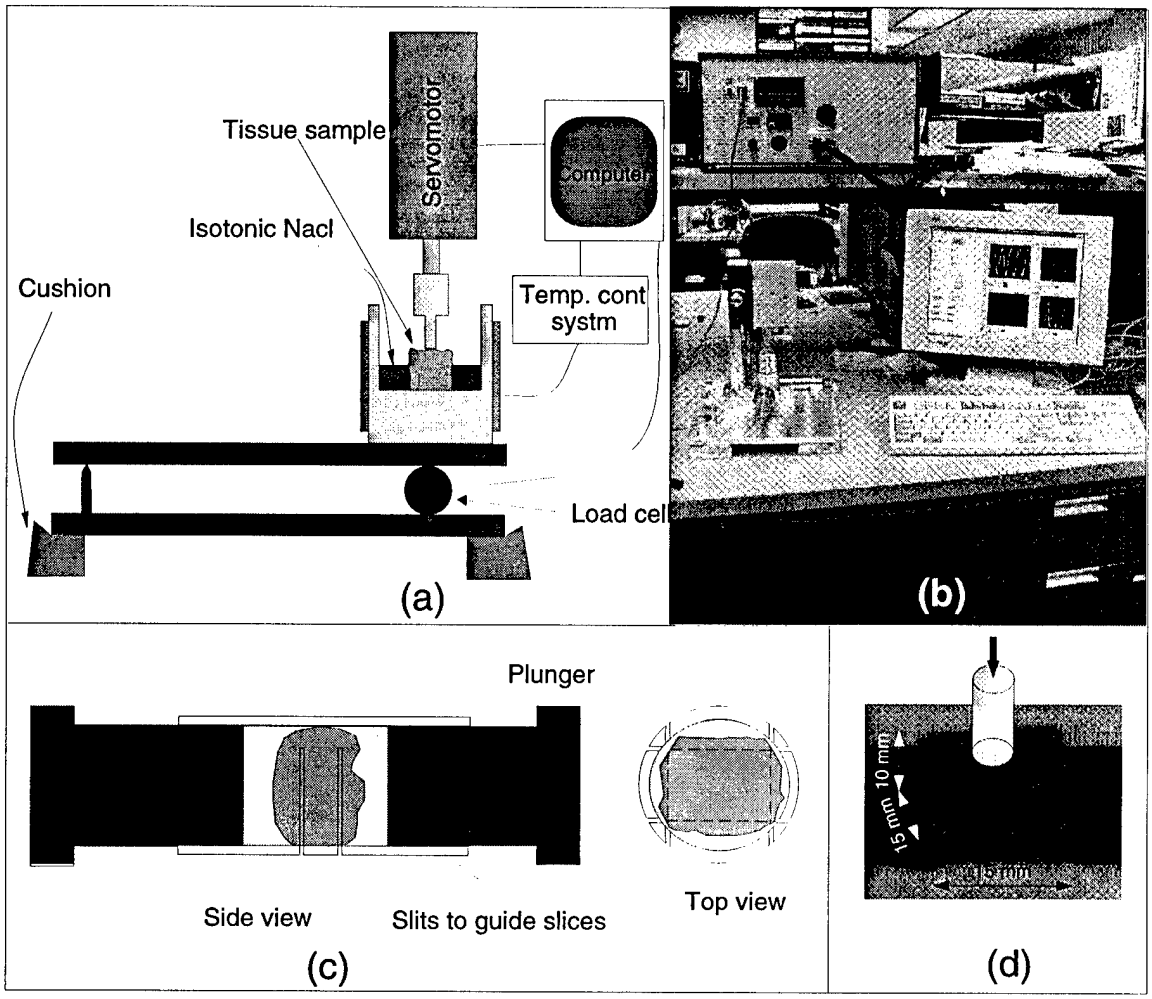
Tissue sample
Servomotor
Computer
Isotonic Nacl
Cushion
Temp. cont
systm
Load cel
(a)
(b)
Plunger
Side view
Slits to guide slices
Top view
(c)
15 mm
10 mm
(d)

Figure 2.

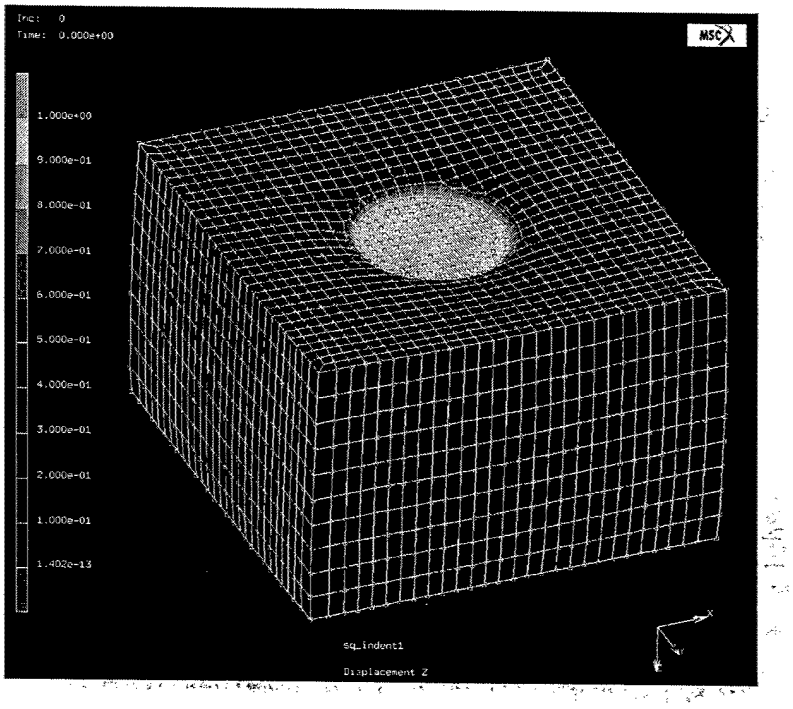

Figure 3.

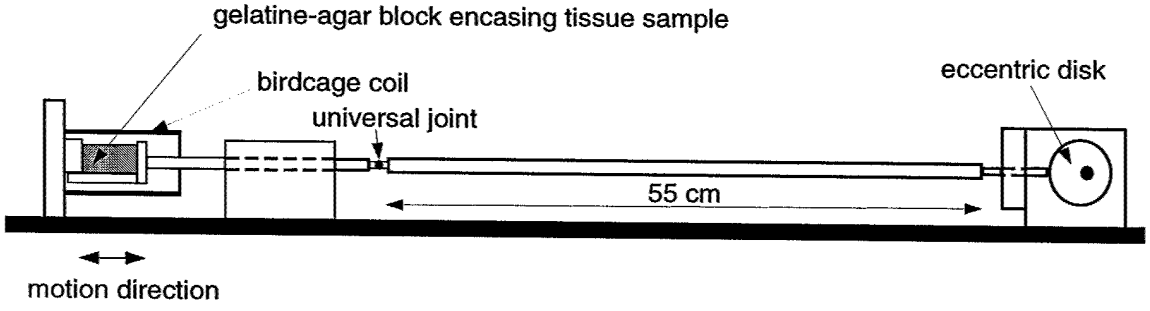

Figure 4.

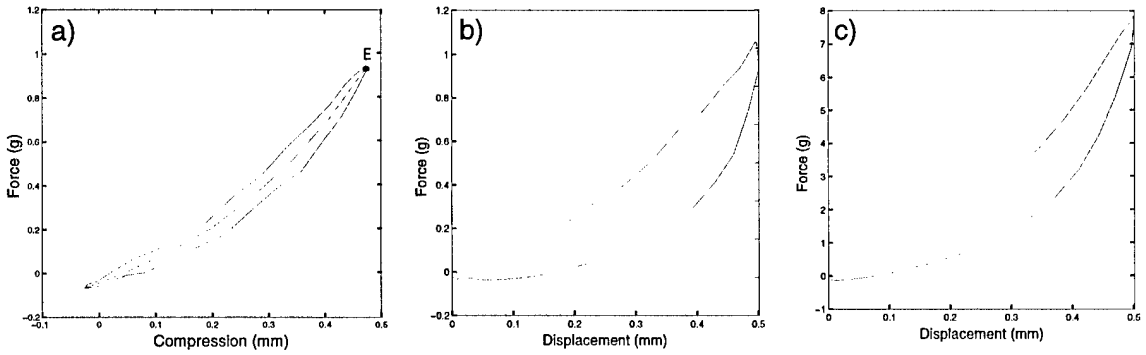
a)
E
Force (g)
Compression (mm)
b)
Force (g)
Displacement (mm)
c)
Force (g)
Displacement (mm)

Figure 5.

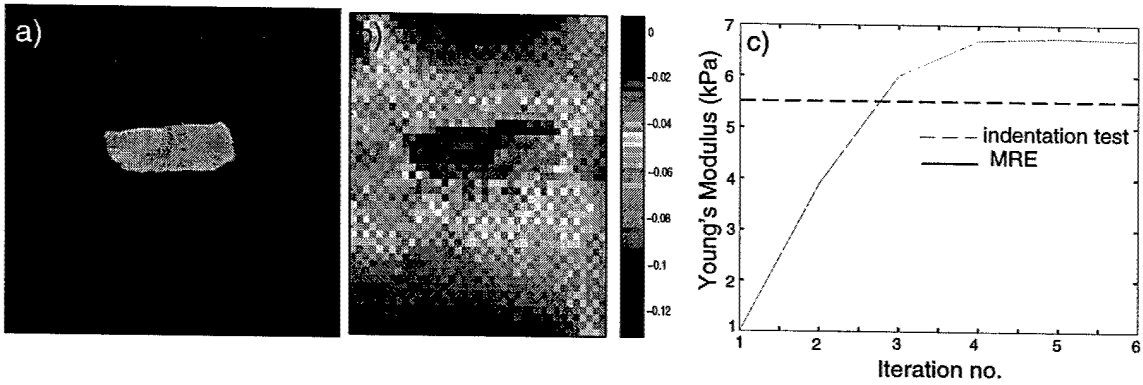
a)
b)
0
-0.02
-0.04
-0.06
-0.08
-0.1
-0.12
c)
Young's Modulus (kPa)
indentation test
MRE
Iteration no.
1
2
3
4
5
6
7

Figure 6.

MR validation of soft tissue mimicing phantom deformation as modeled by nonlinear finite element analysis

Justin Sciarretta, Abbas Samani, Jonathan Bishop,[a] and Donald B. Plewes[b]
Department of Medical Biophysics, University of Toronto, 2075 Bayview Ave., North York, Ontario M4N 3M5, Canada

(Received 20 November 2000; accepted for publication 17 September 2001; published 26 December 2001)

A study of the applicability of nonlinear finite element analysis (FEA) to predict soft tissue deformation was validated with phase contrast magnetic resonance velocity imaging. A phantom of varying stiffness was placed in a special purpose, computer controlled MR compatible compression apparatus which provided precise, time varying compression with surface deformations on the order of 11%. The resulting motion was measured with MR velocity images acquired throughout the cycle of compression. The phantom geometry was modeled with a finite element mesh and the mechanical properties of the phantom material were measured and incorporated in the FEA model. The motion as calculated by the FEA model was compared to the motion measured with MRI and the results were found to vary with the material's Poisson's ratio and the coefficient of friction. A minimum difference was reached when the Poisson's ratio and coefficient of friction were set to 0.485 and 0.3, respectively. Under these conditions, the root mean square difference was found to be 14.4%. © *2002 American Association of Physicists in Medicine.* [DOI: 10.1118/1.1420733]

I. INTRODUCTION

In recent years there has been a renewed interest in the biomechanical properties of soft tissue. This interest is motivated by a number of emerging applications in medical imaging and tissue simulation. In imaging applications, it is clear that multimodality imaging is becoming increasingly important as a means of detecting both functional and anatomic elements of disease. A good example would be in breast imaging where mammography, US, MRI, and scintimammography data are acquired, each reporting different aspects of tissue morphology and physiology. However, images taken with these four modalities occur in different geometries, thereby making comparison difficult. In order to ensure meaningful correlation of these data, a means of mapping or co-registering one image into another in a biomechanically accurate manner is needed.[1] Accordingly, knowledge of the constitutive properties of normal and diseased tissues and the means for accurate finite element analysis (FEA) modeling are required. Furthermore success in this application offers further opportunities for FEA modeling for surgical simulation and predicting reconstructive surgical outcomes.

Another interesting application is in the area of disease diagnosis. It is well recognized that different pathologies can be manifest as local variations in tissue stiffness, a concept which is routinely used in clinical palpation for breast cancer. The details of the biomechanical properties may reflect the molecular features of the underlying components of the tissue and may be influenced by the alterations in the tissue microvasculature associated with cancer. Changes in microvasculature may in part be responsible for the observed increases in tissue interstitial pressure[2] which in turn influences apparent stiffness. Previous ex-vivo studies have demonstrated variations in the elastic modulus of tissue as much as 15-fold between normal breast parenchyma and highly calcified breast carcinomas.[3] To exploit the potential for detection and characterization intrinsic in these biomechanical variations, many investigators[4–6] have attempted to develop imaging methods which visualize and/or calculate the distribution of stiffness throughout the anatomy. This imaging concept, often referred to as Elastography, was developed by the US community[7] and has more recently become an active area of investigation in the MR community.[8–11] Frequently Elastography requires the use of inverse solutions[12–14] to reconstruct tissue modulus on the basis of tissue deformation which in turn implies an understanding of the underlying response of tissue to known loads. Some of these inversion processes[15–17] utilize FEA methods and therefore an understanding of the applicability of FEA will facilitate the development of inverse solutions.

Thus an understanding of the applicability of FEA to modeling heterogeneous structure is required. In this paper, we develop a heterogeneous tissue equivalent phantom, apply known time dependent compression and measure the motion with MR. In parallel, FEA modeling of the phantom was conducted and a comparison of the calculated motion and the measured motion was completed. The purpose of this paper is to present a validation study of using the FEA in predicting soft tissue deformation. This study consists of two components. One is the consideration and details that must be taken into account to have a reliable FEA model and the other is studying the errors associated with MRI measurement of motion and how they can be corrected. Accordingly, in this paper we explore the accuracy of FEA modeling to soft tissues based on a validation with MR motion tracking.

II. MATERIALS AND METHODS

A. Phantom development and MR motion tracking

A heterogeneous soft tissue equivalent phantom was constructed using gelatin agar materials and distilled water

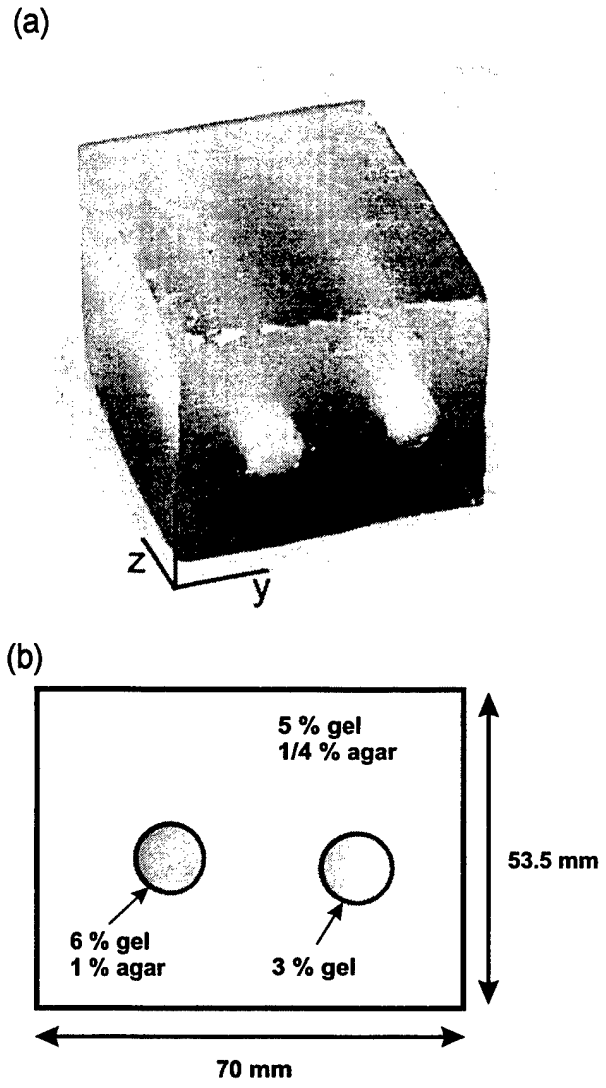

FIG. 1. A typical phantom with dual agar inclusions (a). Schematic cross section of the phantom used in the experiment (b).

(SIGMA–ALDRICH CANADA LTD.). These materials are commonly used in MR experiments as a tissue equivalent material.[9,12] The phantom consisted of two cylindrical inclusions of varying stiffness embedded in a cubic phantom as shown in Fig. 1. The two inclusions were composed of a mixture of 6% gelatin 1% agar, and 3% gelatin, respectively. The main body of the phantom was a mixture of 5% gelatin 0.25% agar. Agar concentration was varied to create materials with a range of stiffness. Gelatin was used to provide strong coupling and prevent slippage between the inclusions and the main body during the motion cycle. The material stiffness of the gels were representative of values previously measured in soft tissue.[3]

The phantom was placed in a MR compatible mechanical compression device which was capable of applying highly repeatable and controlled compression. As shown in Fig. 2, the motion was delivered by an ultrasonic motor coupled to the compressor cam through a timing belt. An ultrasonic motor was used as it contains no ferromagnetic components and was found to not produce artifacts when placed greater than

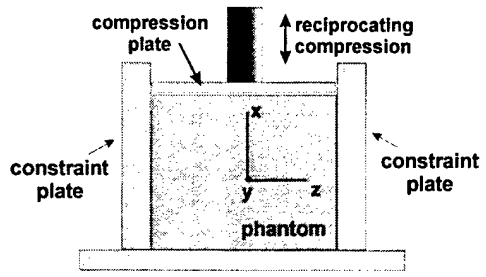

FIG. 2. Geometry of the phantom and compressor system.

50 cm away from the object being imaged. The motor was computer controlled and generated a synchronization signal at the start of each compression cycle which was used to trigger the MR pulse sequence. The amplitude of the longitudinal motion can be controlled by adjusting the geometry of the cam. The phase of the cam relative to the motor's TTL timing signal is also adjustable. The phantom motion was constrained by two plates along the z direction as shown in Fig. 2 to minimize motion parallel to the axis of the cylindrical inclusions and thereby better simulate a two-dimensional motion geometry. The phantom was placed on paper which was used to absorb moisture and prevent slipping. A surface coil was mounted in the compression device adjacent to the phantom and used to deliver high SNR.

Imaging was done on a 1.5 Tesla whole-body imager (GE Medical Systems SIGNA). The velocity of the voxels was measured with a spoiled gradient recalled pulse sequence that incorporated bipolar motion sensitizing gradients during the TE interval. The imaging parameters used were a TR and TE of 76 ms and 16 ms, 10 mm slice thickness, 10 cm field of view, 256×128 pixels, and a 10° tip angle. All of the imaging was done in the axial (x–y) plane (Fig. 1). The frequency of oscillation of the compressor plate was 0.75 Hz.

A preliminary experiment was conducted to test the sinusoidal nature of the time varying motion of the compressor plate. This was done by attaching a thin piece of gelatin to the compressor plate and tracking its velocity during the cycle of motion. The maximum velocity to achieve a π phase rotation (Venc) was set to 20 mm/s.

Velocity images for the inclusion phantom were acquired for both the x and y directions during cyclical motion with Venc set at 20 mm/s and 18 mm/s, respectively. The overall motion of the phantom at the compressor plate was 5.9 mm along the x direction. This corresponds to an average strain of 0.11. The duration of the bipolar gradients were 10 ms and their strength were varied to achieve the appropriate motion sensitivity. To remove offsets due to B_0 inhomogeneity from the final phase data, two averages for each line of k space were acquired and subtracted while alternating the polarity of the bipolar gradients.

B. Velocity tracking algorithm

The velocity data acquired during the compression cycle was used to calculate spin displacement using an algorithm similar to that described by Pelc *et al.*[18] In our implementa-

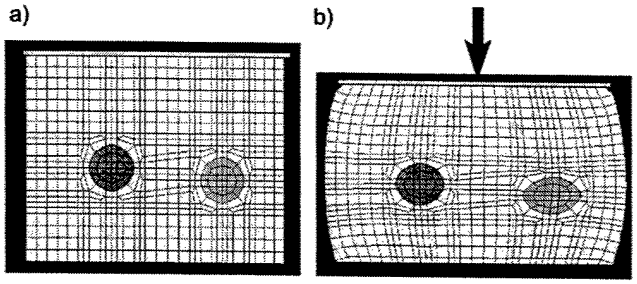

FIG. 3. Uncompressed (a) and compressed finite element mesh (b) used to model the phantom with the hard and soft inclusions (left and right, respectfully).

tion of the algorithm, the velocity data was integrated over time based on first and second order motions derived from a Taylor expansion of the motion trajectory and an iterative estimation of acceleration. The integration was conducted both forward and backward in time and the paths were averaged.[18] To test the effectiveness of this technique, we compared the motion of the compressor plate to that calculated by the tracking algorithm and the degree to which the trajectory fits a sinusoidal temporal profile.

C. Material stiffness measurements

The mechanical properties of the materials which were incorporated in the FEA model were obtained using a uniaxial loading experiment. Samples of each of the phantom components measuring approximately 5 cm×5 cm×3 cm were placed on an electronic balance and a uniform compression was applied to the upper surface. Strain was varied in multiple small increments to a maximum of approximately 0.11 using a calibrated vernier. The time between each strain increment was 3 seconds and a balance measurement was obtained immediately after each strain increment. The stress was calculated for each strain increment by dividing the electronic balance measurement of total force by the initial cross sectional area of the sample. From these data, a stress–strain plot was obtained for each material. To test for strain rate effects in stiffness, a second set of stress–strain measurements were obtained in which the strain increments were increased by a factor of 5 to the same maximum strain values. A third experiment to detect tissue hysteresis was conducted by comparing the modulus while increasing and decreasing the applied stress. These stress–strain measurements were incorporated into the FEA model of the phantom.

D. FEA model

A finite element mesh (Fig. 3) was manually generated using the known geometry of the phantom. The mesh that was produced was two-dimensional since the motion was assumed to be insignificant along the third dimension due to the applied constraints. The mesh was composed of 728, 4-noded elements. Small imperfections on the perimeter of the phantom were not modeled.

To model a continuum, constitutive assumptions are used to describe the response of the material to applied forces. Material theories based on linear and nonlinear stress–strain relations were used in the analysis.

For the linear material theory, the Young's modulus of the materials that was determined through a linear fit of the uniaxial loading experiment was implemented in the model. For the nonlinear behavior modeling, a hyperelastic incompressible model was used in conjunction with the large deformation theory to account for geometrical nonlinearities. For this purpose a Mooney–Rivlin strain energy function[19] was used to model the material stress–strain relationship defined as

$$E(\lambda_1,\lambda_2,\lambda_3)=C_{10}(I_1-3)+C_{01}(I_2-3)+D^{-1}(J-1)^2. \tag{1}$$

C_{10} and C_{01} are constants (ABAQUS/Standard User's Manuals, Version 5.7 (1998), Hibbitt, Karlsson, and Sorenson, Inc.) that are related to the stress–strain relationship of the material such that

$$\sigma=6\epsilon\{C_{10}+C_{01}-(C_{10}+2C_{01})\epsilon\}, \tag{2}$$

where σ and ϵ are the stress and strain in the uniaxial directions. I_1 and I_2 are defined as

$$I_1=J^{-2/3}(\lambda_1^2+\lambda_2^2+\lambda_3^2), \tag{3}$$

$$I_2=J^{2/3}(\lambda_1^{-2}+\lambda_2^{-2}+\lambda_3^{-2}). \tag{4}$$

λ_i are the principal stretches which are the eigenvalues of the square root of $\mathbf{F}^{\mathbf{T}}\mathbf{F}$.[20] $\mathbf{F}$ is the material deformation gradient which physically describes the motion that each point incurs during the compression. J is the determinant of the deformation gradient $\mathbf{F}$.[20] For infinitesimal strain, D is related to the bulk modulus of compression through the equation

$$D=2/K_0. \tag{5}$$

For infinitesimal strain, the bulk modulus of compression is defined as

$$K_0=2(C_{01}+C_{10})/(1-2\nu), \tag{6}$$

where ν is the Poisson's ratio.

Accordingly, we calculated these parameters by fitting the stress–strain relationships from the uniaxial experiments to a second order equation in strain and solved for the parameters C_{01} and C_{10} through Eq. (2).

Both material theories assumed that the material properties were isotropic, meaning that stiffness and compressibility are independent of the choice of reference frame. Compressibility in the linear material theory was modeled directly through Poisson's ratio. Compressibility in the hyperelastic (nonlinear material) model is determined through the D parameter. It was assumed that the compressibility of each material was the same and independent of strain. Since the Poisson's ratio of the gel was not measured experimentally, this parameter was adjusted to achieve a minimum difference in calculated and measured displacement over the area of the phantom.

Unlike the slow cyclical compression delivered in the MR experiment, the compression for the FEA was modeled as a single step compression of 5.9 mm as applied in the MR experiment. This choice was made since acceleration induced forces within the phantom are negligible compared to the stress distribution arising from the applied loading. Accordingly, a static FEA model is a reasonable approximation. Other studies have shown that mechanical behavior is influenced significantly by the slippage condition of loaded surfaces.[21] In Hall *et al.*,[21] two slippage boundary conditions were applied in the FE model, one with free slippage and the other with no slippage. This led to a significant difference in the predicted mechanical behavior obtained from these two models. In our FE model, we used a more realistic model to simulate the slippage between the top of the phantom and the moving compression plate. For this purpose, an isotropic coefficient of Coulomb friction was applied in the FEA model (ABAQUS User Manuals). This allows for slipping once the shear stress σ_s on a surface is greater than the critical stress. In the Coulomb friction model, this relationship is described through the contact pressure p and the coefficient of friction f

$$\sigma_s > fp. \tag{7}$$

The coefficient of friction was fit using a minimum difference in the displacement comparison. The boundary condition modeled for the bottom of the phantom was nonslip.

E. Comparison analysis of experimental and FEA data

To compare the measurements of displacement determined from the experiment to that calculated with the FEA model, we calculated the average RMS difference. Specifically, this amounted to

$$\lambda = N^{-1}\Sigma|(u_x^M - u_x^F)/u_x^M|, \tag{8}$$

$$\theta = N^{-1}\Sigma|(u_y^M - u_y^F)/u_y^M|, \tag{9}$$

where u_x^M and u_x^F stand for the displacements along the x direction calculated from the MR velocity images and the FEA model, respectively. In order to maximize the significance of this error parameter, pixels were excluded in the analysis that underwent very small motions less than 0.4 millimeters. This number corresponds to a motion approximately 10 times that expected from noise in the NMR images[22] and represents a lower limit of motions for which the FEA was tested. The overall root mean square difference Δ is defined as

$$\Delta = (\lambda^2 + \theta^2)^{1/2}. \tag{10}$$

F. Phantom empirical displacement simulation

The results from the above comparison analysis will be influenced by real differences in motion predicted by FEA and that seen in the MR tracking experiment as well as noise in the experimental data. Thus even in the case where no differences in the FEA and experimental tissue motions were to occur, the comparison analysis in the presence of noise would yield a finite error. Thus to obtain an estimate of the size of this effect, a numerical simulation was conducted. A numerical phantom undergoing known motion was created and the comparison analysis was completed with the same phantom with added noise typical of that expected from the MR experiment.

The simulation was based on empirical observations made from previous experimental velocity data sets and FEA displacement calculations of similar phantoms. In general, the internal displacements of the phantom that were calculated by FEA can be approximated as decreasing linearly from the compressor plate to the bottom of the phantom. Linearity was also observed in the velocity images hence a linear change of displacement was incorporated into the simulation. The simulation consisted of a square two-dimensional object made up of 151×151 pixels (0.3906 mm/pixel). The object underwent sinusoidal time varying compression with a maximum amplitude of 6 mm at the top of the phantom. The temporal and spatial variation in displacement along the direction of compression (x axis) was given as

$$x_d(x) = 3(\cos(\Omega t) - 1)x_\beta(x), \tag{11}$$

where $\Omega = 2\pi/1.333\ \mathrm{s}^{-1}$. The x_β function varies linearly from 0 at the bottom of the phantom to 1 for the top of the phantom. The spatial and temporal variation in displacement perpendicular to the direction of compression (y) was given as

$$y_d(x,y) = 3(\cos(\Omega t) - 1)y_\beta(x,y), \tag{12}$$

$$y_\beta(x,y) = [0.0271y - 0.8]^* \times \exp(-(|x - 29.5|)^{1/2}/3.13 \times 10^8). \tag{13}$$

y_β was maximum near the sides of the phantom, 0 along the center of the phantom and varied along the direction of compression (x) to model the bulging effect (Fig. 4) seen experimentally at the center of the phantom during compression. From these formulas for displacement, the velocity was calculated by taking the temporal derivatives. A velocity image was created every 76 ms using a MATLAB linear interpolation function. Gaussian noise was randomly added through a standard deviation of the velocity (α_v) to each velocity image to create a realistic simulation. The standard deviation in the velocity added to the data is given as

$$\alpha_v = v_{\max}/(\pi \mathrm{SNR}_{\mathrm{MAG}}), \tag{14}$$

where $v_{\max}$ is the maximum velocity encoded by the MR pulse sequence and $\mathrm{SNR}_{\mathrm{MAG}}$ is the magnitude of the signal-to-noise ratio in the magnitude image. This equation is based on the premise that noise in the velocity image is proportional to the phase noise, which is inversely proportional to $\mathrm{SNR}_{\mathrm{MAG}}$. The parameters used in the simulation were $v_{\max} = 20$ mm/s and $\mathrm{SNR}_{\mathrm{MAG}} = 40$, matching those in the experimental conditions.

The MR velocity data had a background offset phase, which meant that even when there was no motion a nonzero velocity was recorded. To simulate this effect, a spatially variable background offset ranging from 0 to 1.5 mm/s was added to each image in the velocity data set. The offset was

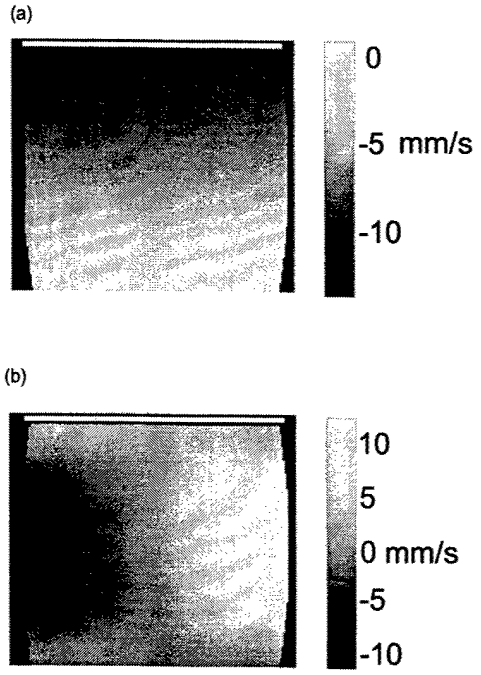

FIG. 4. Simulated velocity image at 304 ms for the displacement along the x direction (a) and along the y direction (b).

similar to the magnitude of the offset measured in the MR velocity data set. The simulated velocity data is illustrated in Fig. 4 which is an image of velocity data at 304 ms into the cycle. Note in Fig. 4(a), the velocity in the x direction is greatest near the top of the phantom and is close to zero at the bottom.

III. RESULTS

A. MR motion tracking

The displacement tracking method was first applied to the MR velocity images of a rigid cylinder that were acquired while tracking the motion of the compressor plate. The forward and backward integration however yielded different paths. For cyclical motion, the material's initial starting point should equal its final calculated position, however as shown in Fig. 5 the calculated finish point at time 1.333 s did not correspond to the initial starting point at time 0 s. This is due to a slowly varying phase offset throughout the image plane which causes an offset velocity. This phase offset was measured by acquiring velocity data while a phantom was stationary. The source of this offset may be related to gradient induced eddy currents. It was found that the phase offset corresponds to approximately an overall velocity variation of 1.5 mm/s across the phantom. This phase offset was effectively removed by incorporating the weighted averaging of the forward and backward integration as shown in Fig. 5(b). After weighted averaging, the overall maximum average pixel displacement of the cylinder was 4.91 mm. This calculation compares well to the applied displacement amplitude of 4.80 mm.

The motion MR tracking method was then applied to the phantom undergoing the sinusoidal compression. From the

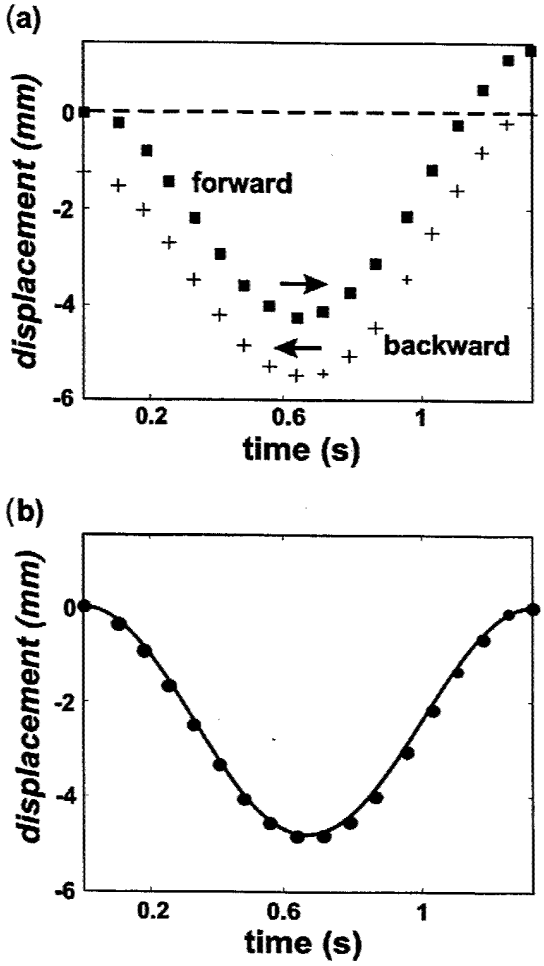

FIG. 5. The forward (■) and backward (+) path for a pixel undergoing a rigid body displacement of −4.80 mm. Note that the final position at $t = 1.33$ s is not equal to the initial position (a). The weighted average between the forward and backward path (●) together with the true sinusoidal motion (—). The start and end points are set to 0 (b).

experimental velocity data, the displacement was calculated for the majority of the phantom at maximum compression as shown in Fig. 6. Displacement tracking near the edges of the phantom was inaccurate due to offset effects and lower SNR and therefore 87% of the overall area of the phantom was used for the comparison of the FEA and MR data. The effect the inclusions have on the displacement fields is seen as a subtle shift in symmetry on the displacement field from the left to right side of the phantom.

B. FEA model

The data collected from the uniaxial experiment on the phantom material is shown in Fig. 7, resulting in a Young's modulus as determined for a linear fit to the stress-strain data as indicated in Table I. Using our apparatus, we found that applying different strain rates did not lead to statistically significant variations in Young's modulus measurement.

The uniaxial experiment for larger strain rates intervals produced similar stress–strain curves when compared to the stress–strain data generated for a lower strain rate. Furthermore, from the stress–strain data acquired during repeated

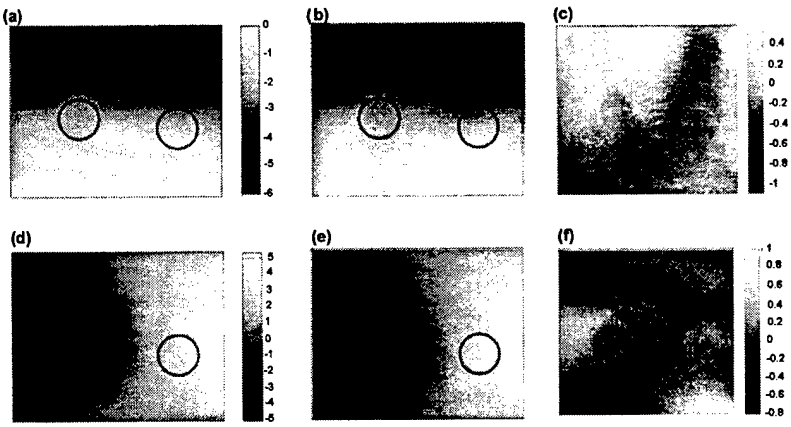

FIG. 6. The displacement along the x direction for the FEA calculation (a), the MRI measurement (b) and the image of the difference between them (c). The displacement along the y direction for the FEA calculation (d), the MRI measurement (e), and the image of the difference between them (f). The FEA calculation of displacement used a Poisson's ratio of 0.485 and a coefficient of friction of 0.3. The black circles in each figure indicate the position of the inclusions.

cycles of increasing and decreasing the stress, it was found that the hysteresis of the materials was insignificant. In addition, these nonlinear data were fit to the Mooney–Rivlin constants C_{01} and C_{10} which are shown in Table I.

C. FEA analysis

The constitutive properties of the materials listed in Table I were incorporated in the FEA model and the displacements were calculated. The Young's modulus of the second and third materials in this table compare well with the findings of Hall *et al.*[21] while the first material cannot be compared since the agar concentration is out of the range investigated in the said paper. Figure 6 illustrates the displacements obtained for a FEA model with a Poisson's ratio of 0.485 and a coefficient of friction of 0.3. Note that the displacement image for the FEA has been linearly interpolated to a pixel resolution of 0.5 mm for visual comparison. Each pixel in the displacement image corresponds to the displacement that occurred at maximum compression for that particular point. Overall, there is a qualitative agreement between the displacement fields.

Poisson's ratio and the coefficient of friction of the phantom were estimated through a minimization of the RMS difference Δ as previously defined. Using the RMS difference to fit Poisson's ratio and the coefficient of friction, Figure 8(a) illustrates Δ as a function of Poisson's ratio for a coefficient of friction of 0.3. Clearly Δ is minimum for a Poisson's ratio close to 0.485. By plotting Δ as a function of the coefficient of friction for a Poisson's ratio of 0.480, 0.485, and 0.49 [Fig. 8(b)], the coefficient of friction was determined to be 0.3. The effect of slipping on the FEA model was found to be relatively limited to only the upper portions of the phantom.

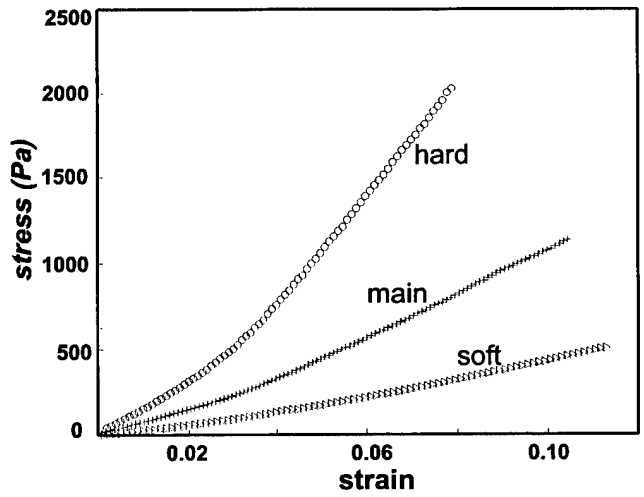

FIG. 7. Stress–strain relationship of the three phantom materials.

The RMS difference Δ is listed in Table II for both the nonlinear material model and the linear material model. The results in Table II are for a linear material model with a Poisson's ratio $\nu=0.485$. Using this value of Poisson's ratio, it results in a nonlinear material model with $D=26.1\,(\mathrm{N/mm^2})^{-1}$ for the main body (corresponding to a Poisson's ratio of 0.485 for small strains). From Table II, one would expect the RMS difference to be slightly better for the nonlinear theory, however the slight increase could be due to the difference in the representation of compressibility.

The error calculated through the comparison of the MR data set and the FEA model however is influenced by the noise in the MR images. This effect was studied on the simulated phantom velocity data set. The tracking method was initially applied on the noise free velocity data set from the simulation and the displacement was calculated at $t=684$ ms. An error analysis was used to compare the true displacement to the calculated displacement at $t=684$ ms with the root mean square difference over N pixels defined as

$$\xi=(\Pi^2+\Theta^2)^{1/2}, \tag{15}$$

$$\Pi=N^{-1}\Sigma|(u_x^C-u_x^T)/u_x^C|, \tag{16}$$

$$\Theta=N^{-1}\Sigma|(u_y^C-u_y^T)/u_y^C|, \tag{17}$$

TABLE I. Young's modulus and Mooney Rivlin coefficients of the phantom materials calculated by fitting uniaxial data.

Phantom material	C_{01} (Pa)	C_{10} (Pa)	Young's modulus (Pa)
6% gelatin, 1% agar	26 300	−23 300	26 800
5% gelatin, 0.25% agar	5400	−4200	11 200
3% gelatin	2200	−1700	4500

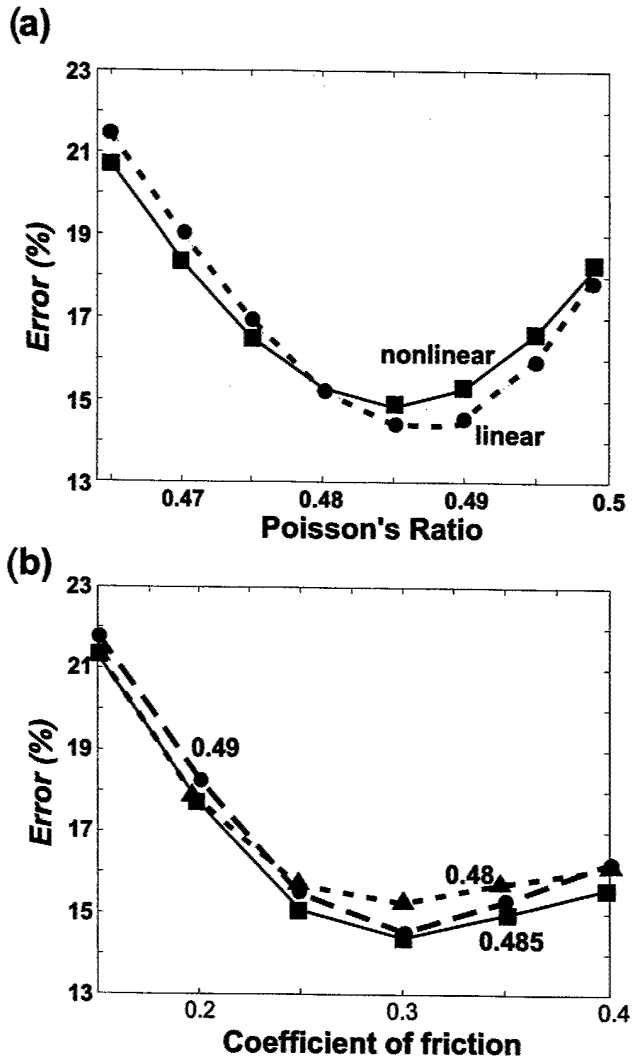

FIG. 8. The root mean square difference Δ as a function of Poisson's ratio for the linear (●) and nonlinear (■) FEA models for a coefficient of friction of 0.3 (a). The root mean square difference Δ for a linear FEA model with a Poisson's ratio of 0.48 (●), 0.485 (■) and 0.49 (▲) (b).

where u_x^T is the value obtained from Eq. (11) and u_x^C is the displacement calculated with the tracking algorithm along the x direction. Using this definition, the RMS difference ξ for the two sets of data was 1.5%. This result illustrates that ignoring the higher order terms in the Taylor expansion as well as having a time of 76 ms between each velocity frame is sufficient to obtain an accurate estimation of displacement.

The tracking algorithm was then used to estimate the RMS difference that occurs due to noise and offset. The displacement was calculated from the simulated velocity set with noise and offset and then compared to the noise free displacement. To be consistent with the error as indicated in Sec. II E, pixels whose motion were less than 0.4 mm were not considered in the error. For the representative noise and offset levels included in the simulation, the calculated RMS difference ξ was 2.9%.

Finally, the effect of misalignment between the experimental phantom set of data and the FEA calculation of motion was studied with the simulation. When a comparison of the same sets of displacement data was made with an offset of 1 pixel (0.39 mm), the RMS difference ξ as previously defined was 3.5%. For an offset of 0.78 mm, the RMS difference ξ increased to 7%.

The RMS difference due to pixel misalignment of the MR and the FEA displacement data and noise inherent to the MR measurement of displacement hence affect the results seen in Table II. The results then in Table II reflect the true differences in displacement intrinsic to the FEA model as well as errors associated with misalignment and MR noise.

TABLE II. NB, for λ and θ, N is 625 and 596, respectively.

	Linear	Nonlinear
λ	9.4%	9.8%
θ	10.9%	11.2%

IV. DISCUSSION

Through series of experiments using MR velocity imaging, it is evident that for simple geometry and material used in our experiments, finite element analysis accurately predicted soft tissue deformation for moderate surface deformations. However, certain assumptions regarding the modeling of compressibility may have produced differences between the FEA model and the MR measurement. Furthermore, a smaller error possibly could have resulted from the differences in the application of the compression between the experiment and the FEA model. Finally, the MR measurement of motion had an associated noise level that also caused differences between the FEA model of the displacement and the MR measurement.

For both material models, it was assumed that compressibility was independent of material and strain and this may have caused some error since material compressibility was not measured. Experimental measurements of compressibility are extremely difficult and cannot be made with any degree of accuracy. In general, researchers working in this field have estimated the Poisson's ratio of soft tissue to be near incompressible and our initial assumption was similar. However, with the assumption of near incompressibility, the displacement errors were somewhat larger for both the nonlinear and linear material model, owing to the fact that the model displacements along the y direction were greater than the MR displacements. From Fig. 8, it is clearly evident that as the compressibility increases below the minimum (0.485), the error increases since the material in the model experiences smaller displacement than the actual phantom displacements along the y direction.

A second source of error was due to the difference in the application of the compression between the actual experiment and the FEA model of the motion. In the experiment, the compression was cyclical however in the FEA model the compression was assumed to be static. The overall error due to this difference is small since the maximum kinetic energy is at least two orders of magnitude less than the energy due to the elastic forces. Another time dependent factor was vis-

cous effects, which were assumed to be negligible for driving frequencies of 0.75 Hz. Bishop *et al.*,[23] however, measured wave attenuation in gels due to viscous effects at higher driving frequencies (100 Hz) and also noted that wave attenuation was an order of magnitude higher for tissue than for gel.

For elasticity reconstruction experiments with high frequency motion, modeling viscous effects in the force equations is required and errors in the accurate inclusion of these effects can potentially result in poor elasticity reconstruction. This problem however may be overcome by using low frequency oscillations since the viscous effects may be minimal in tissue for quasistatic motions. For a driving frequency of 1 Hz, Kallel *et al.*[24] reported that the phase shift between the driving force and the displacement wave form for a kidney was 3 degrees, suggesting that the viscous component was small.

A third source of error was in the MR displacement tracking measurement. This source of error was directly due to noise, offset and a finite number of velocity images. Through simulation, this source of error was estimated to be approximately 2.9%. As this value is smaller than the difference detected by our experiment, we conclude that the presence of noise does not significantly contribute to our results.

Both the nonlinear and linear material models produced similar minimal errors in the comparison of displacement. This was expected since the linear fit to the stress-strain data was a relatively accurate representation of the data over the strain range. For example, breast tissue is likely to illustrate nonlinear stress–strain relationship over larger strain ranges hence a linear material model may produce greater differences than a nonlinear model. As well, the stress–strain relations are likely anisotropic. Once further measurements of the actual stress–strain relationship for breast tissue are completed, these issues can be further investigated through a FEA model of a breast undergoing compression with both a nonlinear and linear stress–strain relationship.

A somewhat unexpected finding was that the gel was slightly compressible. The FEA fit of the parameter yielded similar results of Poisson's ratio for both material theories. In the strictest sense, the Poisson's ratio of any material is only defined for infinitesimal deformations, however the experiment used large deformations on the order of 11%. Thus the FEA fit of the Poisson's ratio parameter can be interpreted as an effective or average Poisson's ratio over the range of strain.

In conclusion, these results have demonstrated that FEA can accurately predict motion, thus it is worthwhile to further investigate the use of FEA in data fusion applications, soft tissue modeling for tissue simulation, and elasticity reconstruction.

ACKNOWLEDGMENTS

This work has been partially supported by a Natural Sciences and Engineering Research Council PGS A scholarship and the Terry Fox Foundation. This paper was presented in part at the Eighth Meeting of the International Society of Magnetic Resonance in Medicine, Philadelphia, PA, 1999.

[a]J. Bishop was with the Department of Medical Biophysics, University of Toronto, Toronto, Canada. He is now with Colorado, MEDtec, Inc., Boulder, CO 80301.

[b]Author to whom correspondence should be addressed. Electronic mail: dbp@sten.sunnybrook.utoronto.ca

[1] A. Samani, J. Bishop, M. J. Yaffe, and D. B. Plewes, "Biomechanical 3-d finite element modeling of the human breast using MRI data," IEEE Trans. Med. Imaging **20**, 271–279 (2001).

[2] J. S. Young, C. E. Lumdsden, and Al. Stalker, "The significance of the 'tissue pressure' of normal testicular and of neoplastic tissue in the rabbit," J. Pathol. Bacteriol. **62**, 313–333 (1990).

[3] A. P. Sarvazyan *et al.*, Elasticity imaging as a new modality for cancer detection, Proceeding of International Workshop on Interaction of Ultrasound with Biological Media, Valenciennes, France, 1994, pp. 69–81.

[4] B. Garra *et al.*, "Elastography of breast lesions: Initial clinical results," Radiology **202**, 79–86 (1997).

[5] R. Muthupillai, D. J. Lomas, P. J. Rossman, J. F. Greenleaf, A. Manduca, and R. L. Ehman, "Magnetic resonance elastography by direct visualization of propagating acoustic strain waves," Science **269**, 1854–1857 (1995).

[6] R. Sinkus *et al.*, "MR-elastography applied to in-vivo MR mammography," Proc. Intl. Magn. Reson. Med. **7**, 259 (1999).

[7] J. Ophir *et al.*, "Elastography: A quantitative method for imaging the elasticity of biological tissues," Ultrason. Imaging **13**, 111–134 (1991).

[8] R. Muthupillai *et al.*, "Magnetic resonance imaging of transverse acoustic strain waves," Magn. Reson. Med. **36**, 266–274 (1996).

[9] D. B. Plewes, I. Betty, S. N. Urchuk, and I. Soutar, "Visualizing tissue compliance with MR imaging," J. Magn. Reson. **5**, 733–738 (1995).

[10] C. J. Lewa and J. D. de Certaines, "MR imaging of viscoelastic properties," J. Magn. Reson Imaging **5**, 242–244 (1995).

[11] J. B. Fowlkes *et al.*, "Magnetic resonance imaging techniques for detection of elasticity variation," Med. Phys. **22**, 1771–1778 (1995).

[12] T. Chenevert *et al.* "Elasticity reconstructive imaging by means of stimulated echo MRI," Magn. Reson. Med. **39**, 482–490 (1998).

[13] F. Kallel, M. Bertrand, and J. Ophir, "Fundamental limitations on the contrast transfer efficiency in elastography: An analytic study," Ultrasound Med. Biol. **22**, 463–470 (1996).

[14] J. Bishop, A. Samani, and D. B. Plewes, "Pressure/modulus inversion for MR elastography," Proc. Intl. Magn. Reson. Med. **7**, 2063 (1999).

[15] D. B. Plewes, J. Bishop, A. Samani, and J. Sciarretta, "Visualization and quantification of breast cancer biomechanical properties with magnetic resonance elastography," Phys. Med. Biol. **45**, 1591–1610 (2000).

[16] E. E. W. Van Houten *et al.*, "Elasticity reconstruction from experimental MR displacement data: initial experience with an overlapping subzone finite elementinversion process," Med. Phys. **27**, 101–107 (2000).

[17] A. Samani, J. Bishop, and D. B. Plewes, "A constrained modulus reconstruction technique for breast cancer assessment," IEEE Trans. Med. Imaging **20**, 877–885 (2001).

[18] N. J. Pelc *et al.*, "Tracking of cyclic motion with phase-contrast cine MR velocity data," J. Magn. Reson Imaging **5**, 339–345 (1995).

[19] M. A. Crisfield, *Non-linear Finite Element Analysis of Solids and Structures*, Vol. 2: Advanced Topics (Wiley, New York, 1997).

[20] D. S. Chandrasekharaiah and L. Debnath, *Continuum Mechanics* (Academic, New York, 1994).

[21] T. J. Hall, M. Bilgen, M. F. Insana, and T. A. Krouskop, "Phantom materials for elastography," IEEE Trans. Ultrason. Ferroelectr. Freq. Control **44**, 1355–1365 (1997).

[22] A. Lingamneni *et al.*, "Validation of Cline phase-contrast MR imaging for motion analysis," J. Magn. Reson Imaging **5**, 331–338 (1995).

[23] J. Bishop *et al.*, "Magnetic resonance imaging of shear wave propagation in excised tissue," J. Magn. Reson. **8**, 1257–1265 (1998).

[24] F. Kallel *et al.*, "Elastographic imaging of low-contrast elastic modulus distributions in tissue," Ultrasound Med. Biol. **3**, 409–425 (1998).

Biomechanical 3-D Finite Element Modeling of the Human Breast Using MRI Data

Abbas Samani*, Jonathan Bishop, Martin J. Yaffe, and Donald B. Plewes

Abstract—**Breast tissue deformation modeling has recently gained considerable interest in various medical applications. A biomechanical model of the breast is presented using a finite element (FE) formulation. Emphasis is given to the modeling of breast tissue deformation which takes place in breast imaging procedures. The first step in implementing the FE modeling (FEM) procedure is mesh generation. For objects with irregular and complex geometries such as the breast, this step is one of the most difficult and tedious tasks. For FE mesh generation, two automated methods are presented which process MRI breast images to create a patient-specific mesh. The main components of the breast are adipose, fibroglandular and skin tissues. For modeling the adipose and fibroglandular tissues, we used eight noded hexahedral elements with hyperelastic properties, while for the skin, we chose four noded hyperelastic membrane elements. For model validation, an MR image of an agarose phantom was acquired and corresponding FE meshes were created. Based on assigned elasticity parameters, a numerical experiment was performed using the FE meshes, and good results were obtained. The model was also applied to a breast image registration problem of a volunteer's breast. Although qualitatively reasonable, further work is required to validate the results quantitatively.**

Index Terms—**Breast, finite element analysis, image registration, mesh generation, MRI.**

I. Introduction

PREDICTING breast tissue deformation is of great significance in several medical applications such as surgery, biopsy and imaging. In breast surgery, surgeons are often concerned with a specific portion of the breast, e.g., tumor, which must be located accurately beforehand. Locating the portion of interest is done using imaging techniques which are done under tissue configuration of compression or body position that is often entirely different from that of surgery. In this case, nonrigid image registration is required to locate the portion of interest in the new configuration. In breast biopsy, the biopsy needle causes the breast tissue to deform which may lead the tumor to displace. This deformation renders the guiding images less accurate unless the displacements are determined and needle aiming is corrected accordingly. In multimodality imaging of the breast, images of different modalities are often obtained under different tissue configurations of compression, orientation, or body position. In this case, determining the tissue deformation is essential for facilitating data fusion [1]. FEM has been widely used in modeling biological tissues such as bone [2]–[4] and myocardium [5], and recently in modeling brain deformation [6]–[8]. This work is aimed at using FEM in modeling breast tissue deformation.

For a FE model to be satisfactory in predicting deformation and other relevant parameters, in addition to using accurate elasticity parameters and boundary conditions, a reasonably accurate FE geometry model is essential. As the breast is composed of soft tissues, large deformation is usually created while undergoing medical procedures. In this paper, large deformation is considered in the FE formulation, and soft tissues are modeled as incompressible hyperelastic materials based on the experimental data of [9]. Viscoelastic response is not taken into account in this model as we do not expect it to be important on the short time scales, such as in breast medical applications. Nevertheless, it is possible to incorporate viscoelasticity into our model provided that relevant parameters are available. Boundary conditions in medical applications are usually displacement type which are known relatively accurately. In multimodality imaging which involves X-ray mammography, the boundary conditions are not fully known as the contact surface cannot be identified easily. However, a contact problem formulation as presented in [1] can be used which only requires the magnitude of the compression plate movement.

For breast FE mesh generation, marching-cubes-based techniques such as [10] can be implemented. However, the tetrahedral elements used in these techniques are well known to have unfavorable characteristics, such as slow convergence with mesh refinement. Also, these elements may exhibit overstiffening and volumetric locking especially with incompressible material [11], [12]. Accordingly, with biological soft tissues which are known to be incompressible, using hexahedral elements in the FE model is cost effective and more accurate. To our knowledge, there has been no work done for patient-specific mesh generation of the breast using hexahedral elements. However, computed tomography (CT) has been used by a number of investigators to automate mesh generation in bone. Many investigators [2], [13]–[17] have applied edge-detection algorithms on CT images to generate boundary contours of the struc-

Manuscript received August 9, 2000; revised December 6, 2000. This work was supported by the Terry Fox Foundation under Program Project Grant 006886 and by the U.S. Army under Grant DAMD 17-99-19391. The Associate Editor responsible for coordinating the rewiew of this paper and recommending its publication was M. W. Vannier. *Asterisk indicates corresponding author.*

*A. Samani is with the Department of Medical Biophysics, Imaging/Bioengineering Research Group, Sunnybrook and Women's College Health Sciences Centre, University of Toronto, 2075 Bayview Ave., Toronto, ON, M4N 3M5, Canada (e-mail: asamani@sten.sunnybrook.utoronto.ca).

J. Bishop was with the Department of Medical Biophysics, Imaging/Bioengineering Research Group, Sunnybrook and Women's College Health Sciences Centre, University of Toronto, Toronto, ON, M4N 3M5, Canada. He is now with Colorado MEDtec, Inc., Boulder, CO 80301 USA.

M. J. Yaffe and D. B. Plewes are with the Department of Medical Biophysics, Imaging/Bioengineering Research Group, Sunnybrook and Women's College Health Sciences Centre, University of Toronto, Toronto, ON, M4N 3M5, Canada.

Publisher Item Identifier S 0278-0062(01)02773-2.

tures in each image, then employed some techniques to generate the internal mesh. This strategy often requires a significant investment of time by an expert user, and is incapable of automatically generating reasonably accurate meshes for heterogeneous and geometrically complex objects. Other investigators [18]–[20] developed techniques that directly convert image voxels to eight noded hexahedral elements. The resulting object surfaces in these techniques are characterized by abrupt transitions and right angles. As a result, FEM leads to less accurate results, especially on the surface [21], [22]. This paper presents two methods for generating three-dimensional (3-D) meshes of the breast using magnetic resonance imaging (MRI) data. The first method converts image voxels to hexahedral elements and is similar to the said methods except that edge detection is done semi-automatically via segmentation. The second method is based on the transfinite interpolation (TI) technique [23] which is more accurate and efficient in creating smooth surfaces.

To validate the mesh generation component of this model, a cubic agarose phantom with a cylindrical inclusion was constructed and imaged using MRI. Using these images, FE meshes were created using the meshing techniques presented in this paper. To assess the accuracy of these methods, another mesh was created manually based on the known geometry of the phantom. The FEM was applied to these meshes to calculate the deformation and stress distribution resulting from a lateral compression similar to X-ray mammography procedures. The results obtained from both meshes compare well with the manually created mesh results except for the inclusion's circular interface where, as expected, the TI-based mesh produced better results. To demonstrate a potential clinical application of this model, MR images of a healthy volunteer's breast was acquired and a FE mesh was created using the meshing techniques. A lateral compression similar to X-ray mammography procedures was simulated using the TI-based mesh, and calculated MR images are presented in the postcompression configuration.

II. Methods

A. Governing Equations

We use a 3-D FE model to predict breast tissue deformation based on the biomechanical parameters of the breast tissues. While undergoing medical procedures, the breast often deforms significantly. Accordingly, linear elasticity with the infinitesimal deformation formulation is not appropriate to formulate the FE model. As a result, we used a finite deformation formulation in conjunction with hyperelastic material. In a static condition, the equilibrium equation of a body under externally applied forces is

$$\frac{\partial \sigma_{i1}}{\partial x_1} + \frac{\partial \sigma_{i2}}{\partial x_2} + \frac{\partial \sigma_{i3}}{\partial x_3} + f_i = 0; \qquad i = 1, 2, 3 \tag{1}$$

where the σs denote the Cauchy (true) stress tensor components and f_i represents the body force. In the finite deformation formulation, the current position of a point $\mathbf{x}$ is obtained by adding the displacement $\mathbf{u}$ to the corresponding reference position of the same point $\mathbf{X}$, i.e.,

$$\mathbf{x} = \mathbf{X} + \mathbf{u}. \tag{2}$$

The stresses are related to displacements ($\mathbf{u}$) via a strain energy function U which is defined as a function of the strain invariants. These invariants are obtained based on the deformation gradient $\mathbf{F}$ as follows:

$$\mathbf{F} = \frac{\partial \mathbf{x}}{\partial \mathbf{X}}. \tag{3}$$

To separate the deviatoric and volumetric effects, $\overline{\mathbf{F}} = J^{-1/3}\mathbf{F}$ is defined, where $J = \det(\mathbf{F})$ is the third strain invariant which represents the total volume change at the point. Using $\overline{\mathbf{B}} = \overline{\mathbf{F}}.\overline{\mathbf{F}}^T$, the other strain invariants $\overline{I}_1$, $\overline{I}_2$ can be defined as follows:

$$\overline{I}_1 = \mathrm{tr}\left(\overline{\mathbf{B}}\right)$$
$$\overline{I}_2 = \tfrac{1}{2}\left(\overline{I}_1^2 - \mathrm{tr}\left(\overline{\mathbf{B}}.\overline{\mathbf{B}}\right)\right).$$

Assuming that a strain energy function $U = U(\overline{I}_1, \overline{I}_2, J)$ is selected, the true stress tensor can be obtained using the following equation [11]:

$$\sigma = \frac{2}{J}\left[\left(\frac{\partial U}{\partial \overline{I}_1} + \overline{I}_1 \frac{\partial U}{\partial \overline{I}_2}\right)\overline{\mathbf{B}} - \frac{\partial U}{\partial \overline{I}_2}\overline{\mathbf{B}}.\overline{\mathbf{B}}\right] + \frac{\partial U}{\partial J}\mathbf{I} \tag{4}$$

where $\mathbf{I}$ is the unit matrix. Considering the boundary conditions, (1) and (4) must be solved simultaneously to calculate the displacements $\mathbf{u}$. These equations are solved numerically through the FE method. In this method, after the domain is discretized into a number of homogeneous elements, a nonlinear system of equations is formed that is solved iteratively using Newton's method. This formulation is implemented in ABAQUS, a commercial FE software [11]. Discretization, i.e., mesh generation, especially in medical applications, is the most tedious step in a FE analysis. This step is described in the following sections.

B. Image Acquisition

We have developed meshing techniques which use MR images as an input to create FE meshes. In this work, two sets of MR images were acquired for a phantom and a volunteer's breast. The MR images were acquired using a GE SIGNA 1.5-T scanner (GE Medical Systems, Milwakee, WI). For the phantom, a 5.0-in surface coil was used to acquire T1-weighted axial images. A two-dimensional (2-D) spin-echo pulse sequence was used with 90° flip angle, TR/TE = 400.0/10.5 msec timing properties, 12 × 12 cm field of view (FOV), 256 × 128 resolution and 1.0-mm slice thickness. A magnitude image of this phantom is shown in Fig. 1, in which the inclusion can be seen with subtle contrast. For the breast, T1 weighted sagittal images were obtained using body coil. A 2-D spin-echo pulse sequence was used with 90° flip angle, TR/TE = 300.0/9.0 ms timing properties, 20 × 20 cm FOV, 256 × 128 resolution, 3.0-mm slice thickness, and three acquisitions.

C. Image Segmentation and Edge Detection

The purpose of segmentation is to separate different materials within the object of interest. This is done based on the MR signal intensity of different tissues. In the breast, the two main components, i.e., adipose and fibroglandular tissues, must be

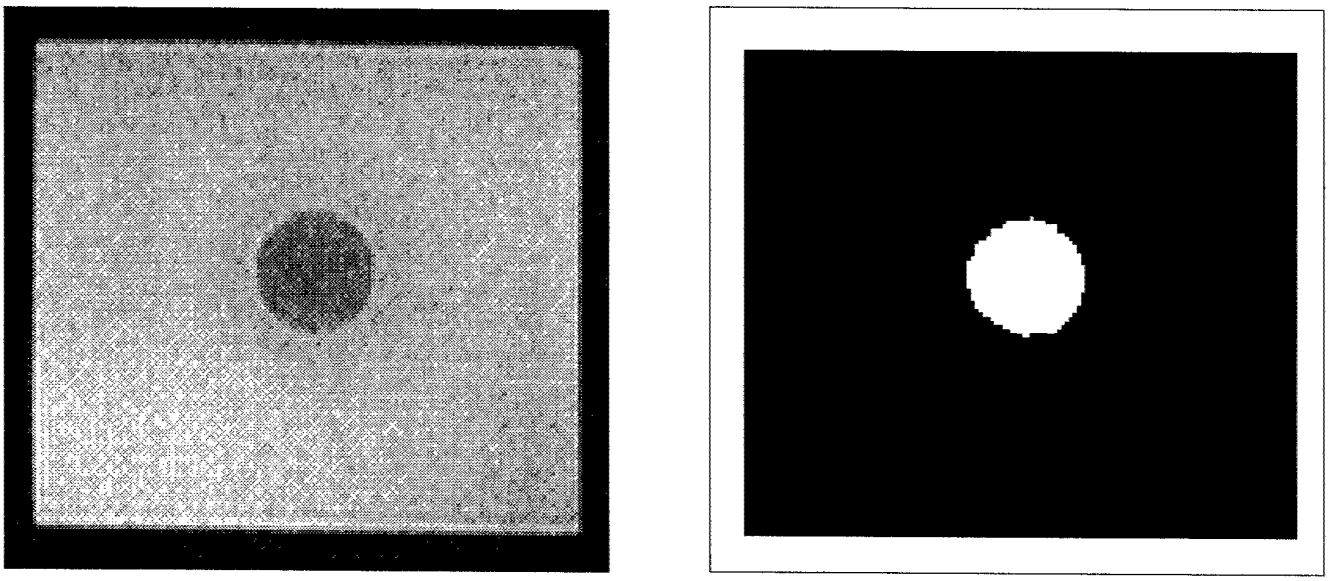

(a) (b)

Fig. 1. (a) A typical MR image and (b) a corresponding segmented image of the phantom.

segmented. For edge detection, as the breast tissues have significant signal intensity compared to the background with only noise signal, segmentation results in automatic breast edge detection. For segmentation, 3-D MRI data of the breast is converted into AnalyzeAVW 2.5 [24] database where a standard thresholding-based tool was used to yield segmented images that are suitable for FE mesh generation.

D. Voxel-Based (VB) Mesh Generation Technique

Because of the complex geometry of the breast and the structure of the fibroglandular tissue, common mesh generators require a significant amount of user interaction which is very time consuming. As an attempt to minimize user interaction throughout the mesh generation step, we have developed an automatic VB mesh generator with the aim of creating relatively accurate FE meshes of complex volumetric data efficiently. In fact, the only step which requires user interaction in this technique is the segmentation step. To construct the mesh, eight noded hexahedral elements are chosen. This type of element is well known to have many favorable characteristics over tetrahedral elements which can demonstrate overstiffening and locking behavior [12]. Right-angled hexahedrals, however, cannot model curved surface geometries which in turn leads to some inaccuracies in surface strains. To improve the mesh in this respect, we used the smoothing technique of Camacho *et al.* [25] which smooths irregular boundaries at model surfaces and material interfaces.

In the VB methods, since one FE is generated corresponding to each voxel, high resolution MR images may lead to huge FE meshes which, due to current computer power limitations, cannot be processed. Moreover, beyond a certain point, finer FE meshes do not practically improve the solution accuracy. Therefore, reducing image resolution is required to meet computational power constraints. For this purpose, a larger voxel size is selected and using the segmented images, the adipose and fibroglandular tissues voxels within each new voxel are counted. The new voxel will then be assigned to be as the one with the larger count.

After segmentation and resolution reduction, the mesh generation process is followed by node, and later element generation. For node generation, based on the pixel size, slice thickness and the coordinate system of the MR scanner, the nodes are arranged in the form of a 3-D rectangular lattice which confines the breast volume. The node coordinates of the lattice are calculated and placed in an array. Working with the regular lattice, later, facilitates element generation significantly because each neighbor node can be determined easily and accessed very quickly in the node array. The lattice, however, represents regions both inside and outside the breast. Regions outside the breast are determined during the element generation process and then discarded from the nodes array after element generation is done.

For element generation, the segmented image of each slice is loaded by the computer and stored in a 2-D array. To facilitate finding the boundary of each slice automatically, we assume that the fibroglandular tissue is surrounded by the adipose tissue portion. If this is not the case, a very thin one pixel size layer which represents adipose tissue can be added on the image manually using XV 3.10a image processor [26] to close the boundary where necessary. The boundary points are found by searching the image array line by line first from left to right and then from right to left until an adipose tissue pixel on the left and right boundaries is reached. These points are stored in two arrays that are later used in element generation. Elements corresponding to adipose and fibroglandular tissues are generated in each slice row by row starting from the left boundary point as the local first element node. Other nodes in each element are determined based on the local numbering scheme of hexahedral element. Element generation in a row is continued until the point prior to the right boundary point is reached. This process is repeated for each row to obtain a slice mesh and then for each slice to cover the entire breast. Slice meshes are then stacked to reconstruct a complete 3-D mesh. Skin elements are

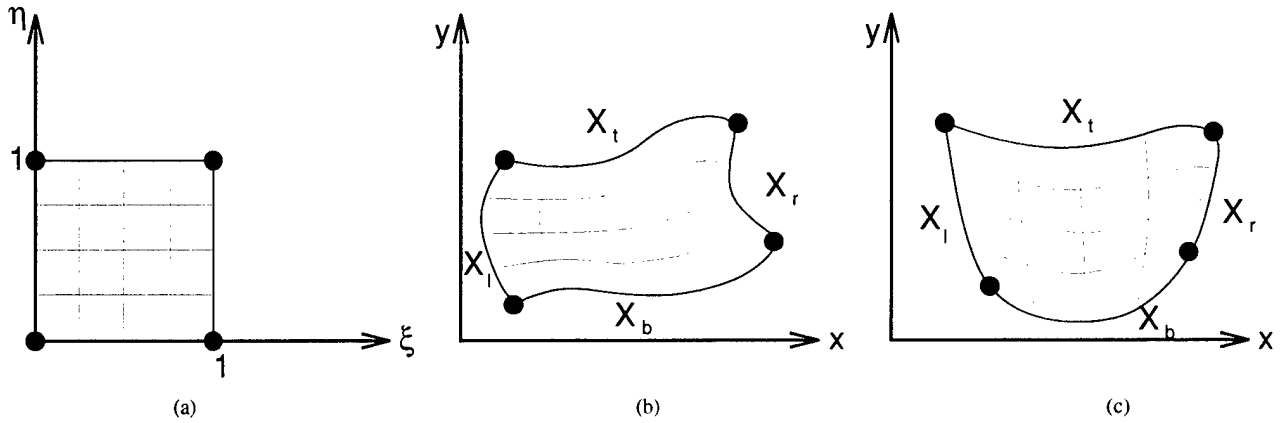

Fig. 2. (a) A unit square (logical space). (b) A typical physical space. (c) Breast boundaries in the TI meshing technique.

generated using four noded quadrilateral membrane elements. These elements are generated by identifying the outer face of elements on the breast surface. Finally, for smoothing, the node coordinates are modified using the smoothing technique of Camacho *et al.* [25]. In this technique, a smoothing coefficient which varies from zero for no smoothing to 0.5 for maximum smoothing, must be selected by the user. While higher factors result in smoother surfaces and interfaces, i.e., better geometry modeling, element distortion caused by this process leads to less accurate FE analysis. Therefore, to achieve optimal results, the smoothing coefficient must be selected or determined carefully. The meshing algorithm is implemented by creating a MATLAB program which inputs the segmented axial, coronal or sagittal images obtained from MRI data, generates the FE mesh, and outputs an input file compatible with ABAQUS FE software [11]. Henceforth, this meshing program will be referred to as VBMESH.

E. Transfinite Interpolation Mesh Generation Technique

This technique is based on the idea of mapping a unit square (logical space) to any given shape enclosed by four boundaries (physical space) [23]. To implement this idea in breast FE meshing, after image segmentation, the breast boundary in each slice is divided into three segments. Adding the boundary representing the chest wall, as shown in Fig. 2, the breast area will be enclosed by four boundaries. Although not necessary, these boundaries can be fitted by polynomials to smooth out the surface which is corrupted as a result of segmentation errors. After obtaining the breast boundaries in each slice image, the nodes are generated by mapping the nodes of the unit square grid to a set of nodes distributed inside the boundaries using the following equation:

$$\begin{aligned} X(\xi,\eta) = {} & (1-\eta)X_b(\xi) + \eta X_t(\xi) + (1-\xi)X_l(\eta) \\ & + \xi X_r(\eta) - \xi\eta X_t(1) - \xi(1-\eta)X_b(1) \\ & - \eta(1-\xi)X_t(0) - (1-\xi)(1-\eta)X_b(0) \end{aligned} \quad (5)$$

where ξ and η represent the unit square variables and X_b, X_t, X_l and X_r represent the breast's bottom, top, left and right boundaries respectively. Element connections determination in this technique is straight forward as it is done using the nodes of the unit square's grid. Using the same logic, the FE mesh of the skin is created by finding node connections of three of the unit square's circumferential lines corresponding to the breast's surface. After elements in each slice are generated, as in the previous method, they are stacked to construct a 3-D mesh.

Compared to the VB technique, this method requires a significantly smaller number of elements to represent the true geometry of the breast's surface. Furthermore, this method is capable of locally refining the mesh at an ROI by choosing smaller intervals in the corresponding logical space. Similar to VBMESH, this algorithm was implemented by a MATLAB program which will be, henceforth, referred to as TIMESH.

III. Results

A. Meshing Techniques Validation and Comparison

To validate the meshing techniques, the agarose phantom illustrated in Fig. 3 was constructed. This phantom consists of a block of agar (2%) with a hard cylindrical inclusion made of a mixture of 2% agar and 10% glass beads centered at (32.8, 30.5). The glass beads were used to enhance the contrast in the MR image for segmentation purposes. We assume that the Young's moduli of the block and the inclusion are respectively 11.0 Kpa and 55.0 Kpa. The block is also assumed to undergo a static loading due to 9.0-mm compression resulting from a laterally moving rigid plate toward another stationary plate as illustrated in Fig. 3. The phantom was scanned using a 5.0-in surface coil and a set of 60 MR images was acquired. These images were segmented and the resolution was reduced by a factor of four in the x and y directions and to 16 slices in the z direction. An MR image of the phantom and a corresponding segmented image are shown in Fig. 1. The obtained images were processed by VBMESH using a smoothing coefficient of 0.3 and a FE mesh was created. By dividing the inclusion's circumference into four segments and fitting each segment with a quadratic polynomial, another mesh was created using TIMESH. Finally, based on the known geometry of the phantom, a mesh was created manually as a bench mark. Corresponding to each mesh, an input file compatible with ABAQUS was created. These input files were preprocessed and their corresponding meshes are displayed in Fig. 4. Based on the nonlinear finite deformation FE formulation, the meshes were analyzed using ABAQUS 5.8.1, and as a result, the displacements, strains and stresses were calculated. It is well known that in FE analysis the most significant errors are encountered at material interfaces and curved surfaces which

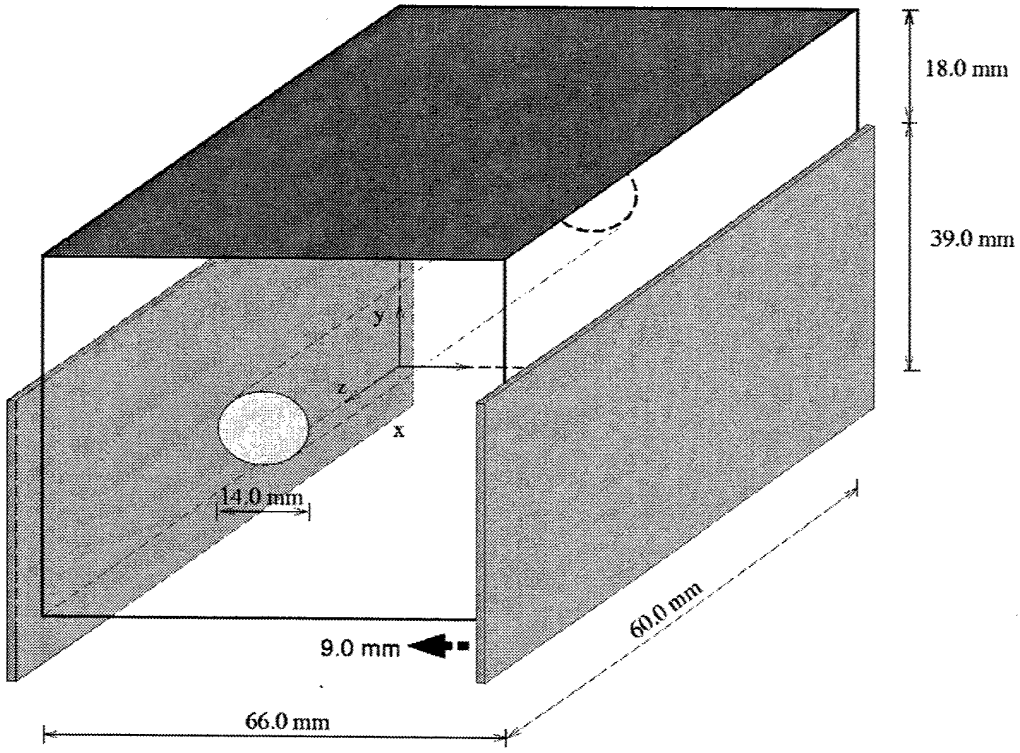

Fig. 3. A schematic of the phantom and its compression model.

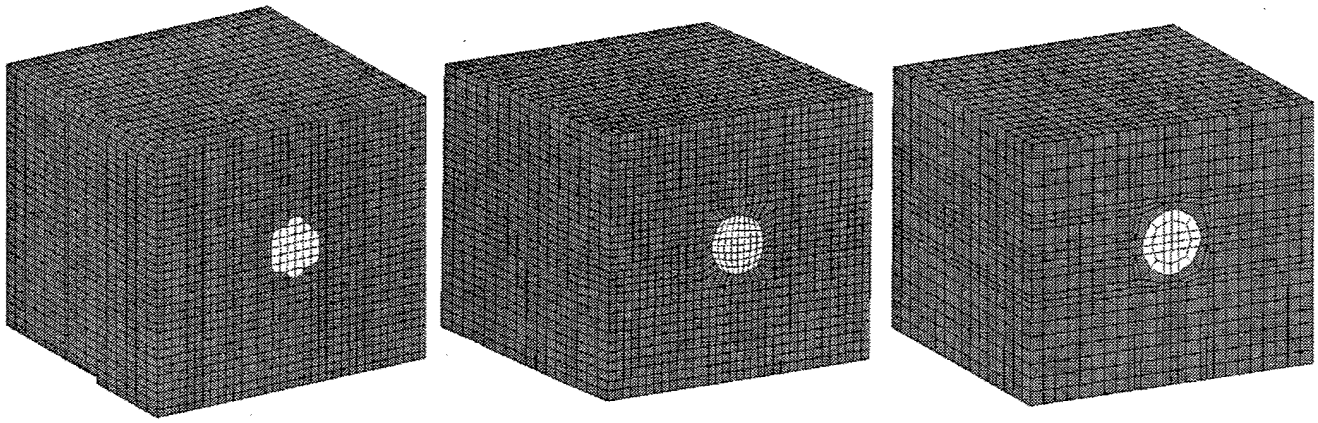

Fig. 4. (a) VB FE mesh, (b) TI-based FE mesh, and (c) A manually created FE mesh of the phantom.

are not represented appropriately by the FE mesh [22]. Therefore, to assess the accuracy of the presented meshing techniques, we will focus on the nodal values at the inclusion's circumference. As an example, the results of a displacement, a strain, and a stress component at this region in the middle plane are displayed in Fig. 5, which qualitatively indicates the better performance of the TI-based technique. To make a quantitative comparison, the average $\overline{E}$ and standard deviation σ of the relative error of the displacement, strain and stress over the inclusion's circumferential nodes are calculated and summarized in Table I. The results clearly indicate that the TI-based technique leads to more accurate FE meshes. Moreover, compared to the displacements errors, the strain and stress errors are significantly larger. This can be justified based on the fact that calculating both strains and stresses involves calculating the derivatives of displacements which leads to error magnification.

B. Breast Image Nonrigid Registration

To examine our model in a complex clinical problem, we applied it to a breast image registration problem where the breast was compressed by two plates causing nonrigid deformation. For this purpose, sagittal MR images of a breast of a healthy volunteer were acquired at 6-mm intervals at a resolution of 0.625 mm/pixel. These images were segmented with AnalyzeAVW 2.5 and the resulting images were processed to create FE meshes. A typical sagittal MR image of the breast and a corresponding segmented image are shown in Fig. 6(a) and (b). The objective here was to calculate MR images of

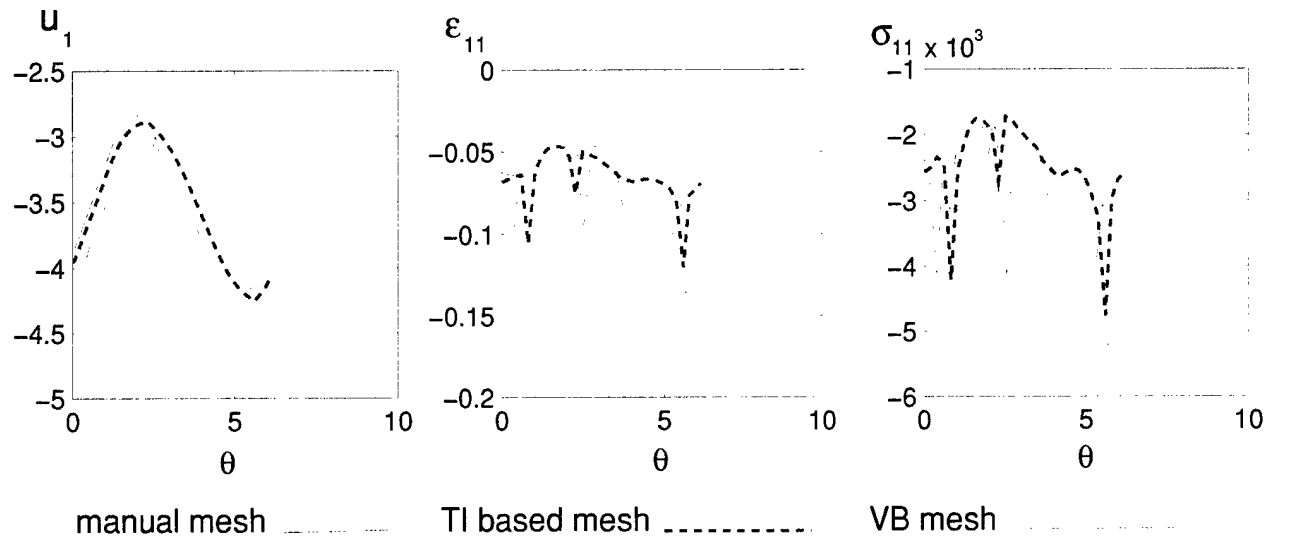

Fig. 5. Variations of the displacement, normal strain, and normal stress in the compression direction around the inclusion's circumference.

TABLE I
AVERAGE RELATIVE ERRORS $\bar{E}$ AND STANDARD DEVIATION σ OF DISPLACEMENTS, STRAINS, AND STRESSES OF THE CALCULATED MESHES AT THE INCLUSION'S SURFACE

Displacements	u_1	u_2	u_3	-	-	-
VB Mesh: $\bar{E}$ (%)	7.50	7.93	5.67	-	-	-
σ (%)	1.38	4.07	3.07	-	-	-
TI Mesh: $\bar{E}$ (%)	1.70	2.04	0.84	-	-	-
σ (%)	0.50	1.69	0.78	-	-	-
Strains	ϵ_{11}	ϵ_{22}	ϵ_{33}	ϵ_{12}	ϵ_{13}	ϵ_{23}
VB Mesh: $\bar{E}$ (%)	18.14	16.94	6.32	16.56	20.86	20.89
σ (%)	7.00	9.79	4.79	11.00	15.23	20.91
TI Mesh: $\bar{E}$ (%)	14.24	8.08	9.82	17.89	13.10	16.33
σ (%)	11.25	7.17	2.83	12.83	10.21	17.27
Stresses	σ_{11}	σ_{22}	σ_{33}	σ_{12}	σ_{13}	σ_{23}
VB Mesh: $\bar{E}$ (%)	17.15	14.55	9.37	16.56	20.86	20.89
σ (%)	9.32	14.89	10.32	11.00	15.23	20.91
TI Mesh: $\bar{E}$ (%)	13.20	8.21	12.03	17.89	13.10	16.33
σ (%)	10.70	8.31	5.36	12.83	10.21	17.27

this breast as if it underwent 8.0-mm compression. For this purpose, two FE meshes were first created using the VB and TI-based techniques. After image segmentation and resolution reduction by a factor of 4 in each direction, the resulting images were processed by VBMESH using a smoothing coefficient of 0.3. The resulting mesh consists of 16 841 elements and 15 939 nodes and is characterized by an abrupt surface. Using the segmented images, the TI-based mesh was created using TIMESH. This mesh was calculated by fitting a third-order polynomial to the boundary representing the chest wall while fitting quadratic polynomials to the breast surface's three segments. The resulting mesh consists of 2280 elements and 2059 nodes and, unlike the VB mesh, has a smooth surface. The FE meshes of one slice created using the VB and the TI-based techniques are depicted in Fig. 6(c) and (d). Fig. 7 depicts the VB mesh, the TI-based mesh of the entire breast, and the breast FE model undergoing compression. The adipose and fibroglandular tissues were assumed to be incompressible and hyperelastic, and the corresponding parameters were obtained by fitting experimental data [9] to a hyperelastic Neo–Hookean model. For this purpose, the data represented as Young's modulus versus strain were converted to stress versus strain by first fitting quadratic and third-order polynomials to the adipose and fibroglandular tissues data, respectively, then integrating over the strain. The resulting fitting polynomials of the Young's modulus versus strain of the adipose and fibroglandular tissues are as follows:

$$E = 0.5197\epsilon^2 + 0.0024\epsilon + 0.0049; \quad \text{for fat}$$

$$E = 123.8889\epsilon^3 - 11.7667\epsilon^2 + 0.6969\epsilon + 0.0121; \quad \text{for parenchyma.}$$

To the authors' knowledge, the experimental data [9] are the only available breast tissue hyperelastic properties data obtained based on the large deformation theory considerations. Nevertheless, as the standard deviation of this data is high, more accurate and reliable data is required to produce better image registration results. Skin, in general, is well known to be anisotropic and hyperelastic [27]. However, it can be approximated by an isotropic and linear elastic model provided that the strain does not exceed 50% [27], [28]. Accordingly, as the skin strain in this application is expected to be well below 50%, it was assumed to be elastic with a Young's modulus of 10.0 kPa [28] and a thickness of 1.0 mm. The chest wall was assumed to provide zero displacement boundary conditions while the specified displacement or force boundary conditions on the breast's surface is not known because the contact surface between the breast and the plates increases over the course of compression. Accordingly, this problem was formulated as a 3-D contact problem and ABAQUS' contact solver with the finite deformation theory formulation was used. This highly nonlinear problem was solved iteratively and, as a result, the breast tissue displacements were calculated. These displacements, in combination with the MR images of the uncompressed breast, were used to obtain simulated MR images of the compressed breast. A number of consecutive sagittal MR images of the breast before compression, along with their corresponding simulated images after compression, are depicted in Fig. 8. In this figure, reasonable translation and tissue expansion can be observed by comparing the two sets of images. For example, image (g′) from the simulated set and

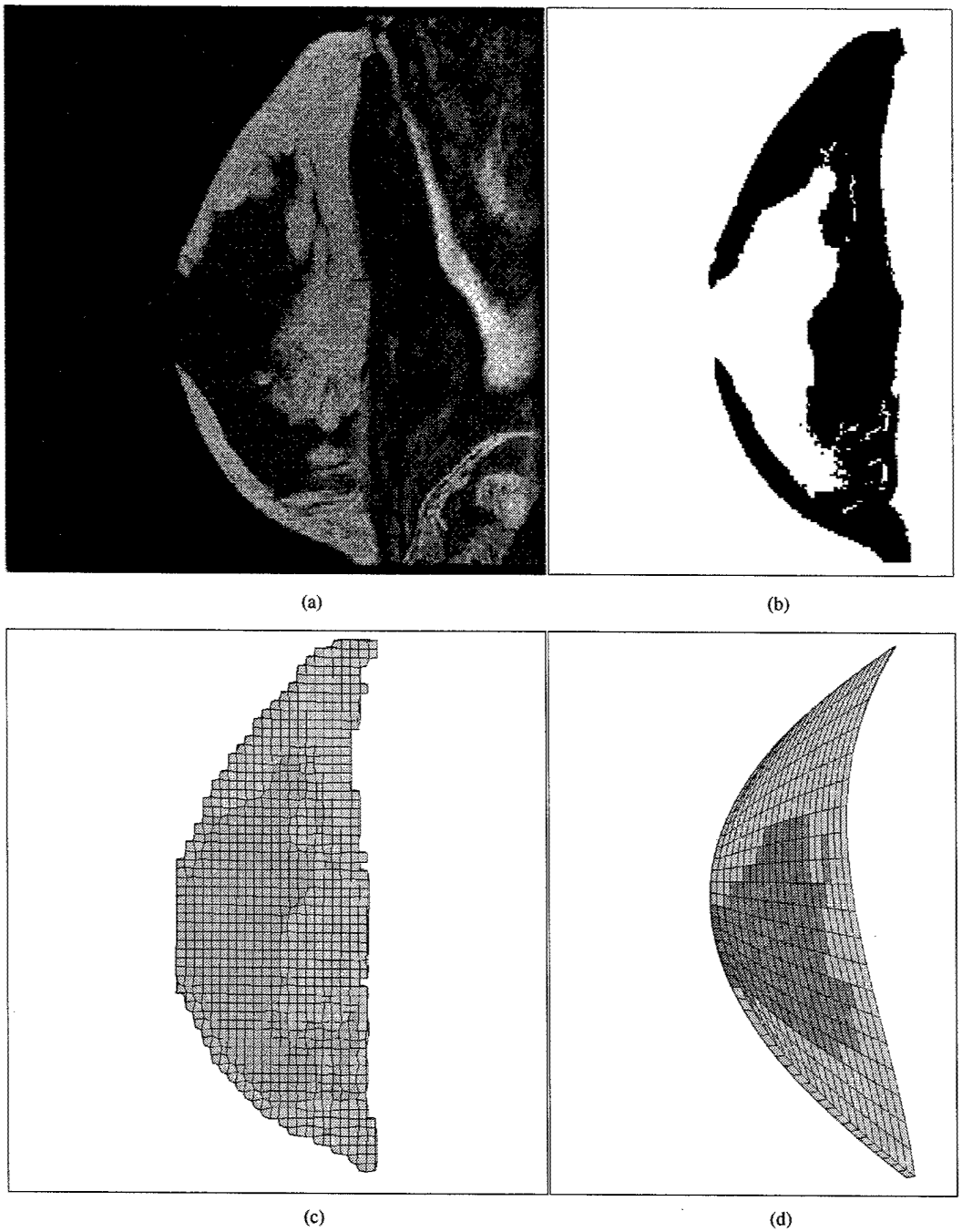

Fig. 6. (a) A MR image and (b) a corresponding segmented image, (c) VB FE mesh, and (d) TI-based FE mesh of one breast slice.

image (f) from the MR image set, which approximately correspond to the same slice, depict similar anatomical features. The same can be observed in other image pairs such as (a, b'), (b, c'), etc.

IV. Discussion

We have presented a FE model, based on biomechanical principles, to predict breast tissue deformations. This model can serve as a guideline in numerous clinical applications, such as breast image registration, multimodality data fusion, breast surgery, and biopsy. The first component of this model is FE meshing, for which two meshing techniques were presented and evaluated. These techniques, which require minimal user interaction, use MRI images of the breast to produce patient-specific FE meshes. Using a numerical experiment, the TI-based meshing technique, which requires fewer elements to represent the geometry of curved surfaces relatively accurately, proved to generate more accurate displacements and stresses. Moreover, unlike the VB technique, this technique is capable of refining the mesh at an arbitrary ROI. The adipose and fibroglandular tissues are modeled as incompressible and hyperelastic materials while the skin is modeled using membrane elements with linear elastic properties. These tissues are assumed to

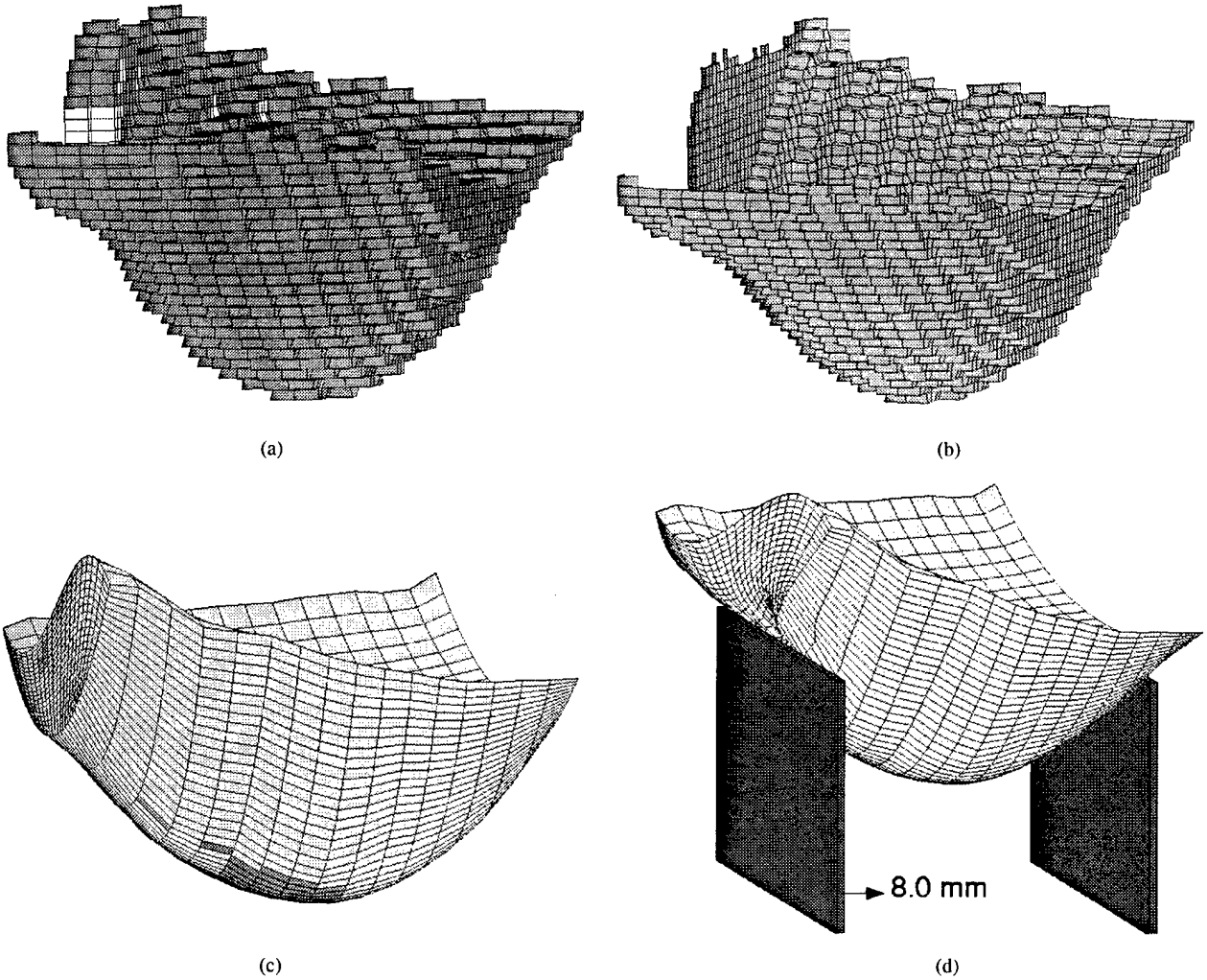

Fig. 7. (a) VB 3-D FE mesh of the breast slice excluding the skin, (b) corresponding skin mesh, (c) TI-based FE mesh of the breast, and (d) the deformed shape of the breast under compression.

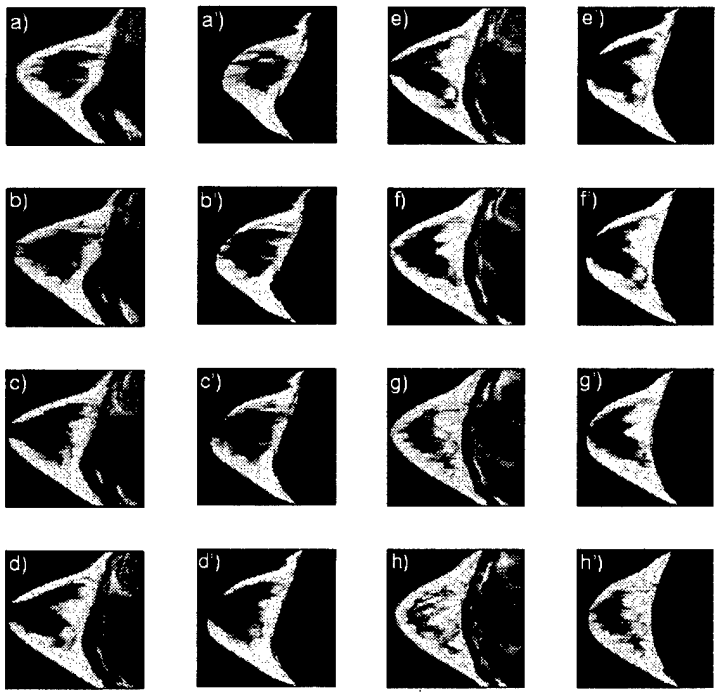

Fig. 8. MR images of the breast before compression (a, b, c, etc.) and simulated images of the compressed breast (a', b', c', etc.).

undergo large deformations. As for boundary conditions, the chest wall region is assumed to provide zero displacements boundary conditions while the specified boundary conditions depend on the clinical application. For example, in the breast image registration problem, as was previously presented, this boundary condition type is not known explicitly and the problem is formulated as a 3-D contact problem. An image registration example was presented to evaluate the FE model's effectiveness in complex clinical applications. The results summarized in Fig. 8 qualitatively prove the merits of this model. Quantitative validation, however, is beyond the scope of this paper as it requires more reliable breast tissue hyperelastic properties data. Research is underway in our laboratory to acquire such data which will pave the way for conducting this validation.

REFERENCES

[1] A. Samani, J. Bishop, E. Ramsay, and D. Plewes, "Breast tissue deformation finite element modeling for MRI/X-ray mammography data fusion," presented at the 5th Int. Workshop Digital Mammography, Toronto, ON, Canada, 2000.

[2] J. H. Keyak, J. M. Meagher, H. B. Skinner, and C. D. Mote, "Automated three-dimensional finite element modeling of bone: A new method," *J. Biomed. Eng.*, vol. 12, pp. 389–397, 1990.

[3] R. Müller and P. Rüegsegger, "Three-dimensional finite element modeling of noninvasively assessed trabecular bone structure," *Med. Eng. Phys.*, vol. 17, no. 2, pp. 126–133, 1995.

[4] W. Krach, T. J. Rammerstorfer, T. J. Reiter, and P. Zenz, "*In vivo* CT-based 3-D-modeling of human bones with respect to inhomogeneity," in *Proc. ASME Bioengineering Conf.*, vol. BED-29, 1995, pp. 57–58.

[5] J. M. Guccione, K. D. Costa, and A. D. McCulloch, "Finite element stress analysis of left ventricular mechanics in the beating dog heart," *J. Biomech.*, vol. 28, pp. 1167–1177, 1995.

[6] S. K. Kyriacou, C. Davatzikos, S. J. Zinreich, and R. N. Bryan, "Nonlinear elastic registration of brain images with tumor pathology using a biomechanical model," *IEEE Trans. Med. Imag.*, vol. 18, pp. 580–592, July 1999.

[7] M. I. Miga, J. M., K. D. Paulsen, Lemery, S. D. Eisner, A. Hartov, F. E. Kennedy, and W. R. D., "Model-updated image guidance: Initial clinical experiences with gravity-induced brain deformation," *IEEE Trans. Med. Imag.*, vol. 18, pp. 866–874, Oct. 1999.

[8] A. Hagemann, K. Rohr, H. S. Stiehl, U. Spetzger, and J. M. Gilsbach, "Biomechanical modeling of the human head for physically based nonrigid image registration," *IEEE Trans. Med. Imag.*, vol. 18, pp. 875–884, Oct. 1999.

[9] P. S. Wellman, "Tactile imaging," Ph.D. dissertation, Harvard Univ., Cambridge, MA, 1999.

[10] J. M. Sullivan Jr., G. Charron, and K. D. Paulsen, "A three-dimensional mesh generator for arbitrary multiple material domain," *Finite Elements Anal. Design*, vol. 25, pp. 219–241, 1997.

[11] *ABAQUS, Theory Manual*, Hibbit, Karlsson, and Sorenson, Pawtucket, RI, June 1998.

[12] T. J. R. Hughes, *The Finite Element Method, Linear Static and Dynamic Finite Element Analysis*. Englewood Cliffs, NJ: Prentice-Hall, 1987.

[13] R. T. Hart, V. V. Hennebel, N. Thongpreda, W. C. Van Buskirk, and R. C. Anderson, "Modeling the biomechanics of the mandible: A three-dimensional finite elemeny study," *J. Biomech.*, vol. 25, pp. 261–286, 1992.

[14] M. J. Rudert and T. D. Brown, "Toward automation of finite element models for bone grafting of femoral head osteonecrosis," in *Proc. ASME Bioengineering Conf.*, vol. BED-28, 1994, pp. 145–146.

[15] V. K. Goel, H. Park, and W. Kong, "Investigation of vibration characteristics of the ligamentous spine using the finite element approach," *J. Biomech. Eng.*, vol. 116, pp. 377–383, 1994.

[16] E. H. II Moor, D. A. Schauer, and J. A. Weiss, "Mesh generation for a finite element model of the human leg," in *Proc. ASME Bioengineering Conf.*, vol. BED-29, 1995, pp. 51–52.

[17] L. Voo, J. A. Denman, N. Yoganandan, and F. Pintar, "A 3-D model of the cervical spine with ct-based geometry," *Adv. Bioeng.*, vol. 29, pp. 323–324, 1995.

[18] D. P. Fyhrie, M. S. Hamid, R. F. Kuo, and S. M. Lang, "Direct three-dimensional finite element analysis of human vertebral cancelous bone," in *Proc. 38th Annu. Meeting Orthopedic Research Society*, vol. 17, 1992, p. 551.

[19] S. J. Hollister and N. Kikuchi, "Direct analysis of trabecular bone stiffness and tissue level mechanics using an element by element homogenization method," in *Proc. 38th Annu. Meeting Orthopedic Research Society*, vol. 17, 1992, p. 559.

[20] B. van Rietbergen, H. Weinans, R. Huiskes, and A. Odgaard, "A new method to determine trabecular bone elastic properties and loading using micromechanical finite-element models," *J. Biomech.*, vol. 28, pp. 69–81, 1995.

[21] C. R. Jacobs, J. A. Mandell, and G. S. Beaupre, "A comparative study of automatic finite element mesh generation techniques in orthopedic biomechanics," in *Proc. ASME Bioengineering Conf.*, vol. BED-24, 1993, pp. 512–514.

[22] R. E. Guldberg and S. J. Hollister, "The accuracy of digital image-based finite element models," *J. Biomech. Eng.*, vol. 120, no. 2, pp. 289–295, 1998.

[23] P. Knupp and S. Steinberg, *Fundamentals of Grid Generation*. Boca Raton, FL: CRC, 1994.

[24] "AnalyzeAVW, Ver. 2.5," Mayo-Foundation, Rochester, MN, 1998.

[25] D. L. A. Camacho, R. H. Hopper, G. M. Lin, and B. S. Myers, "An improved method for finite element mesh generation of geometrically complex structures with application to the skullbase," *Biomechanics*, vol. 30, no. 10, pp. 1067–1070, 1997.

[26] *XV, Ver. 3.10a*, J. Bradley, 1994.

[27] P. Tong and Y. C. Fung, "The stress-strain relationship for the skin," *J. Biomechanics*, vol. 9, pp. 649–657, 1976.

[28] J. E. Bischoff, E. M. Arruda, and K. Grosh, "Finite element modeling of human skin using an isotropic, nonlinear elastic constiutive model," *J. Biomech.*, vol. 33, pp. 645–652, 2000.

A Constrained Modulus Reconstruction Technique for Breast Cancer Assessment

Abbas Samani*, Jonathan Bishop, and Donald B. Plewes

Abstract—**A reconstruction technique for breast tissue elasticity modulus is described. This technique assumes that the geometry of normal and suspicious tissues is available from a contrast-enhanced magnetic resonance image. Furthermore, it is assumed that the modulus is constant throughout each tissue volume. The technique, which uses quasi-static strain data, is iterative where each iteration involves modulus updating followed by stress calculation. Breast mechanical stimulation is assumed to be done by two compressional rigid plates. As a result, stress is calculated using the finite element method based on the well-controlled boundary conditions of the compression plates. Using the calculated stress and the measured strain, modulus updating is done element-by-element based on Hooke's law. Breast tissue modulus reconstruction using simulated data and phantom modulus reconstruction using experimental data indicate that the technique is robust.**

Index Terms—**Breast, elastography, iterative, MRI, quasi-static.**

I. Introduction

IT is well known that variations in tissue elasticity properties, defined by Young's modulus, are associated with the presence of cancer. Recent studies suggest a sixfold increase in the Young's modulus of breast carcenoma compared to normal fibroglandular tissue while fibroadenomas are only a factor of three stiffer than normal breast parenchyma [1]. These observations have stimulated the development of breast magnetic resonance elastography (MRE) techniques such as [2], [3] which are aimed at imaging tissue Young's modulus.

The general basis of MRE is to induce motion within the tissue by mechanical stimulation, measure the resulting deformation using MRI techniques, and, finally, calculate elasticity modulus distribution using an inversion technique. The mechanical actuation used for elastography can be either quasi-static or harmonic. In quasi-static elastography, compressional actuation with very low-frequency (0–5 Hz) is used and the displacements are measured using a stimulated echo sequence. In this sequence, a long mixing time is used to allow dissipation of small elastic vibrations before spatial encoding, as described by Chenevert *et al.* [4]. The other alternative is harmonic actuation in which tissues are perturbed at frequencies of 50–1000 Hz generating compressional or shear waves throughout the tissue. In this case, an oscillating magnetic field is used to induce spin phase in proportion to the amplitude of the tissue motion [5]. More recently, Sinkus *et al.* [6] used a spin-echo sequence with sinusoidal flow-encoding gradients to measure the steady-state motion. For elasticity modulus reconstruction, the static-state and steady-state partial differential equations governing the tissue deformation are used in the quasi-static and harmonic techniques, respectively. Many investigators have attempted to solve the elastography problem while assuming fully heterogeneous tissue. Among these investigators, Skovoroda *et al.* [7], Kallel and Bertrand [8], Ophir *et al.* [9], Chenevert *et al.* [4] and, more recently, Bishop *et al.* [10] and Doyley *et al.* [11] have used the quasi-static technique. Also, Manduca *et al.* [12] have used harmonic shear actuation while more recently van Houten *et al.* [13] and Sinkus *et al.* [6] have used harmonic compressional actuation for tissue stimulation. The full heterogeneity approach leads to highly ill-conditioned inverse problem which, especially in three-dimensional (3-D) cases, is very difficult to solve. To achieve a better conditioned problem, beside filtering the measured displacements and using regularization, the majority of investigators have limited their elastography studies to two-dimensional (2-D) plain strain situations. The plain strain idealization, however, is seldom valid in real clinical applications due to complex anatomy. As an alternative, we have, recently, introduced the idea of a quasi-static constrained elastography technique (Samani *et al.* [14] and Plewes *et al.* [15]) where we assumed a uniform elasticity modulus distribution throughout each tissue volume. Furthermore, we assumed that the elasticity moduli of normal tissues are known while that of suspicious lesions are unknown.

In this paper, we present a detailed description and experimental validation of a constrained elastography technique in which the elasticity moduli of both normal and suspicious tissues are assumed to be unknown. In contrast to unconstrained techniques, this technique can easily accommodate 3-D tissue distribution. This technique uses the nonuniform stress distribution throughout the tissue to reconstruct the elasticity modulus from measured displacements. The stress distribution is iteratively calculated using the finite element method (FEM), and is used to update the elasticity modulus distribution based on Hooke's law. For mechanical stimulation, the breast is placed between two rigid plates, one of which is moved toward the other. As a result, the stress can be calculated using the known

Manuscript received November 27, 2000; revised June 20, 2001. The Associate Editor responsible for coordinating the review of this paper and recommending its publication was A. Manduca. *Asterisk indicates corresponding author.*

*A. Samani is with the Department of Medical Biophysics, University of Toronto, 2075 Bayview Ave., Toronto, ON M4N 3M5, Canada (e-mail: asamani@sten.sunnybrook.utoronto.ca).

J. Bishop was with the Department of Medical Biophysics, Imaging/Bioengineering Research Group, Sunnybrook and Women's Health Sciences Centre, Toronto, ON M4N 3M5, Canada. He is now with Colorado MEDtec, Inc., Boulder, CO 80301 USA

D. B. Plewes is with the Department of Medical Biophysics, Imaging/Bioengineering Research Group, Sunnybrook and Women's College Health Sciences Centre, Toronto, ON M4N 3M5, Canada.

Publisher Item Identifier S 0278-0062(01)08660-8.

displacement boundary conditions of the plates in a 3-D contact problem context [16]. As a result, displacement data acquisition is required in only one direction. Alternatively, measured displacements on the boundaries of a tissue region containing the suspicious lesion region of interest (ROI) can be used as boundary conditions to calculate the stress. In the latter case, data acquisition is required in all directions in order to obtain the required displacement boundary conditions on the ROI's boundaries. The novel feature of the method is the use of anatomical constraints to impose a discrete modulus distribution in the reconstruction. These constraints can be obtained by segmenting a 3-D contrast-enhanced MRI volume into a small number of discrete tissue types with uniform elasticity properties. Through the use of this constraint, it is possible to employ a simple element-by-element computation to perform the updated modulus estimation at each iteration step. This contrasts with previous unconstrained iterative methods which employ nonlinear least squares algorithms [8], [11], in which the inversion of a Hessian matrix must be performed at each step of the iteration.

The proposed reconstruction method is focused on answering a very specific question: What is the relative elasticity modulus, on average, in a focal lesion whose geometry and location are previously identified, compared to the background of normal fibroglandular or adipose tissue? To answer this question, we have developed this iterative reconstruction technique which is computationally efficient and highly insensitive to noise.

II. Theory

Biological tissues can be idealized as continua. As a result of undergoing static loading, tissue deformation is governed by the equations of equilibrium, strain–displacement, and a material constitutive law. The equilibrium equation of a continuum under a static loading is [17]

$$\frac{\partial \sigma_{i1}}{\partial x_1} + \frac{\partial \sigma_{i2}}{\partial x_2} + \frac{\partial \sigma_{i3}}{\partial x_3} + f_i = 0; \quad i = 1, 2, 3 \tag{1}$$

where the σs denote the stress tensor components and f_i represents the body forces/unit volume. To avoid having deformations governed by nonlinear elasticity, mechanical actuation must be applied in such a way that the resulting strains do not exceed 0.05. In this case, the strain ϵ is related to displacements through the following equation:

$$\epsilon_{ij} = \frac{1}{2}\left(\frac{\partial u_i}{\partial x_j} + \frac{\partial u_j}{\partial x_i}\right) \tag{2}$$

where u_i is a component of the displacement vector $\mathbf{u} = (u_1, u_2, u_3)$ in Cartesian coordinates $\mathbf{x} = (x_1, x_2, x_3)$. Assuming isotropic and linear elastic material, Hooke's law relates the strains to stresses as follows:

$$\sigma_{ij} = \frac{E}{1+\nu}\left(\epsilon ij + \frac{\nu}{(1-2\nu)}\delta_{ij}\epsilon_{kk}\right) \tag{3}$$

where E and ν represent Young's modulus and Poisson's ratio and δ_{ij} is the Kronecker delta. Assuming nearly incompressible tissues, we follow other investigators and consider $\nu = 0.499$. As a result, the goal of elastography will be the calculation of E distribution throughout the tissue which is governed by (1)–(3). This is an inverse problem which can be solved using direct [7], [10] or iterative [8], [9], [11] techniques. One component of an iterative inversion algorithm is the forward model. In this context, the forward model is used to calculate displacements and subsequently strains and stresses resulting form a static loading on a tissue with known Young's modulus distribution. This can be done through solving (1)–(3) simultaneously. Since there is no analytical solutions for these equations, particularly in 3-D cases with complex geometries, we solve these equations using the FEM. In this method, the domain is first discretized into a number of homogeneous elements, each of which has a number of nodes where the displacements are defined. The displacements within each element are obtained based on the nodal displacements through interpolation. Using an approximation [18], the governing equations yield a small set of linear equations for each element called the element stiffness equation. The elements' stiffness equations are calculated and then assembled to form a linear system of equations called the global stiffness equation

$$\mathbf{K}\mathbf{u} = \mathbf{f} \tag{4}$$

where

- $\mathbf{K}$ global stiffness matrix;
- $\mathbf{u}$ unknown displacement vector;
- $\mathbf{f}$ force vector.

After applying the boundary conditions, this system is solved to calculate $\mathbf{u}$ and, subsequently, the strains and stresses. This formulation is implemented in ABAQUS: a commercial FE software [19] which we use for the forward model. The second step of the iteration is to update the modulus estimate using the measured displacement vector $\mathbf{u}$. Unlike other investigators [8], [9], [11] who use costly and noise-sensitive nonlinear least squares algorithms, we update the modulus using (3). From this matrix equation, it can be seen that the elasticity modulus can be computed from any one strain component and the three normal stress components. At the ith iteration with ϵ^0 denoting the experimentally measured strain, we can write one of several possible equations for computing an elasticity modulus update

$$\frac{1}{E^{i+1}} = \frac{\epsilon_{11}^0}{\sigma_{11}^i - \nu\sigma_{22}^i - \nu\sigma_{33}^i}. \tag{5}$$

By substituting the measured strain and stress components computed at the current iteration i, the elasticity modulus E^{i+1} of each element is updated. As is usual in near-incompressible material, we assume that $\nu = 0.499$. It must be noted that the equation is expressed as a reciprocal of elasticity modulus for reasons related to random noise, as discussed later. As a final step, we apply the discrete modulus constraint by averaging the calculated moduli over each segmented tissue type and use the result as a uniform elasticity modulus. The discrete modulus constraint yields a stable and rapidly converging inversion algorithm.

The presence of noise in experimental measurement of strain will result in a distribution of reconstructed values in the iteration. To analyze noise propagation and its effect on Young's

modulus reconstruction throughout the iterative procedure, we rewrite (5) in terms of Lame constants λ and μ

$$\frac{1}{E^{i+1}} = \frac{\epsilon_{11}^0}{(1-2\nu)\lambda\epsilon_{kk}^i + 2\mu(\epsilon_{11}^i - \nu\epsilon_{22}^i - \nu\epsilon_{33}^i)}. \quad (6)$$

The first term of the denominator is the product of two small terms and one large term as $\nu - \rightarrow 0.5$. Assuming this product is negligible

$$\frac{1}{E^{i+1}} \simeq \frac{\epsilon_{11}^0}{2\mu(\epsilon_{11}^i - \nu\epsilon_{22}^i - \nu\epsilon_{33}^i)}. \quad (7)$$

Eliminating ϵ_{22}^i and ϵ_{33}^i using the incompressibility condition leads to

$$\frac{1}{E^{i+1}} \simeq \frac{\epsilon_{11}^0}{2\mu(1+\nu)\epsilon_{11}^i} = \frac{\epsilon_{11}^0}{E^i\epsilon_{11}^i}. \quad (8)$$

Thus, the correction to the modulus estimate reduces to the ratio of a single strain component plus the current modulus estimate. This means that the reconstructed modulus E^{i+1} at each iteration is not only degraded by the noisy measured strain but also degraded by the low quality modulus E^i, which was reconstructed in the previous iteration. However, due to the use of the geometrical constraint to enforce a discrete modulus distribution at each step of the iteration and ignoring the variation of ϵ_{11}^i within the tissue, the variance of the modulus estimate σ_E^2 at any iteration step is related to the measured strain component ϵ_0 and its variance $\sigma_{\epsilon^0}^2$ by

$$\frac{\sigma_E^2}{E^2} = \frac{\sigma_{\epsilon^0}^2}{N\langle\epsilon^0\rangle^2} \quad (9)$$

where N is the number of elements contained in the tumor ROI and angle brackets represent mean value. In terms of strain and reconstructed modulus signal-to-noise ratio (SNR) (SNR_ϵ and SNR_E), we have

$$\mathrm{SNR}_E = \sqrt{N}\mathrm{SNR}_\epsilon. \quad (10)$$

The normal tissue volumes also contribute noise to the modulus estimate, but the effect is usually negligible since many more FEs are involved in the averaging compared to tumor. Equation (5) has been deliberately arranged so that the numerator contains the experimentally measured quantity; in this way the noise tends toward zero mean when averaged over the segmented tissue regions, and an unbiased estimate of modulus is then obtained by taking the reciprocal. If the geometric constraint were not enforced, then there would be an accumulation of correlated noise terms, and the SNR of the modulus estimate would decrease at each iteration. The use of the geometric constraint is, therefore, highly advantageous in the treatment of noise. The strain SNR quantity, which was introduced in (10), may not be well understood; it is, therefore, highly desired to be related to the well-known magnitude SNR. For this purpose, assume that the sensitivity of motion encoding is set to ϕ_d cycles/unit displacement. Accordingly, the displacement u is related to the measured phase θ by

$$u = \frac{\theta}{2\pi\phi_d}. \quad (11)$$

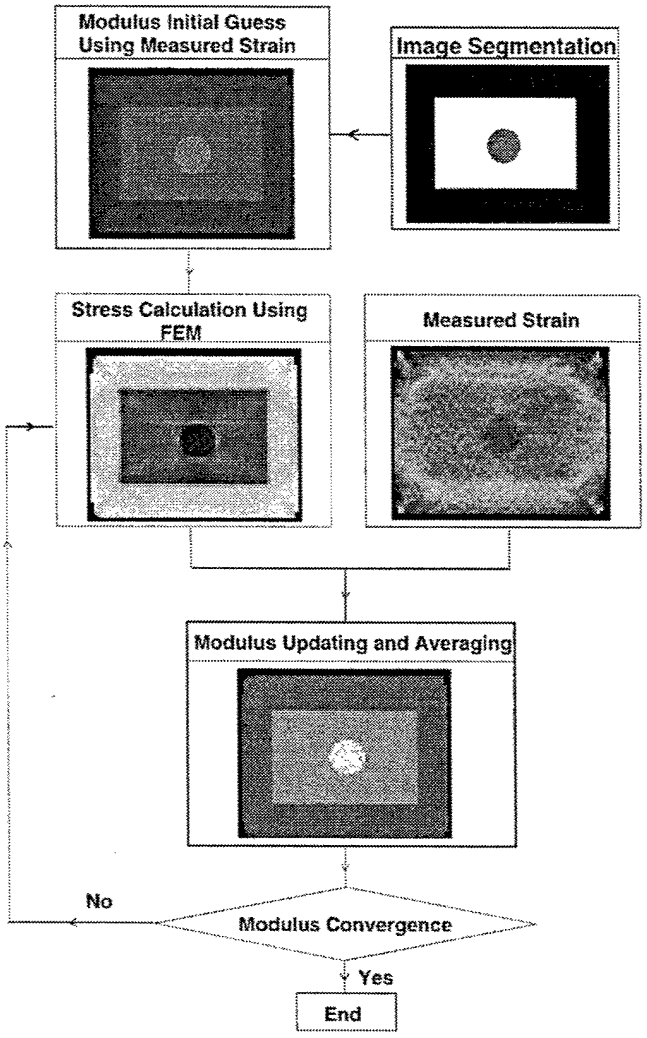

Fig. 1. Flow chart illustrating the iterative procedure for modulus reconstruction.

Given that the strain is calculated from the displacements u through differentiation based on (2) and choosing the forward difference scheme for this purpose, it can easily be shown that the standard deviation of the phase and the strain (σ_p and σ_ϵ) are related by

$$\sigma_\epsilon = \frac{\epsilon}{\mathrm{SNR}_\epsilon} = \frac{\sqrt{2}\sigma_p}{2\pi\phi_d h} \quad (12)$$

where h and ϵ represent the FE size and average strain, respectively. Since phase contrast imaging is usually conducted with two acquisitions subtracted to remove B_0 inhomogeneity offsets, the phase noise is related to the signal magnitude SNR as follows:

$$\sigma_p = \frac{1}{\sqrt{2}\mathrm{SNR}}. \quad (13)$$

Finally, combining (12) and (13) leads to the following equation:

$$\mathrm{SNR} = \frac{\mathrm{SNR}_\epsilon}{2\pi\phi_d h\epsilon}. \quad (14)$$

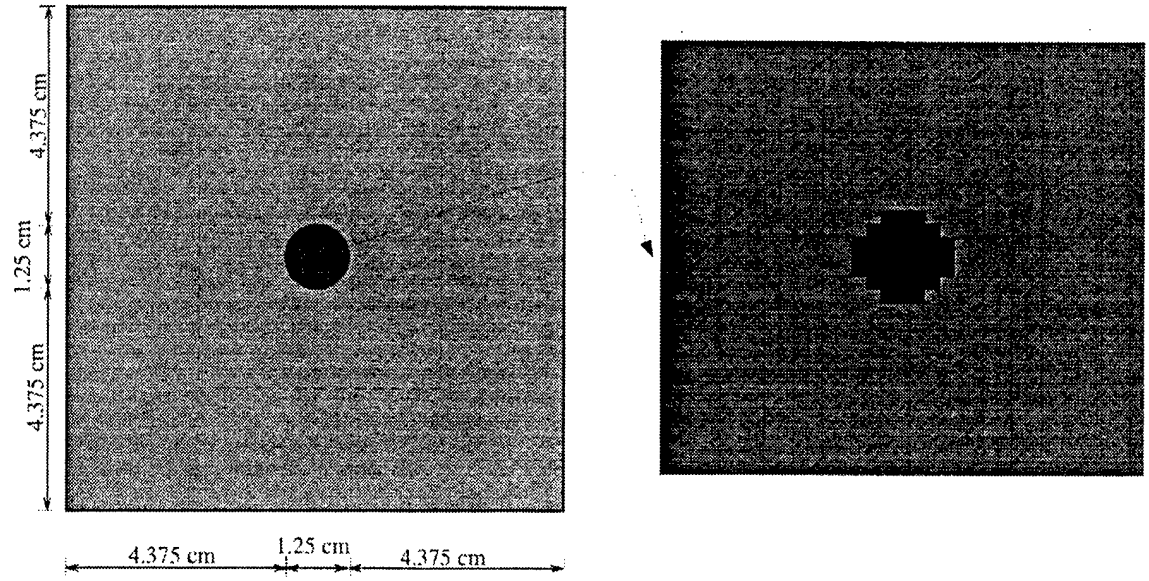

Fig. 2. Two-dimensional simulated phantom. (a) Schematic of the phantom. (b) FE mesh of the 32 × 32 central region shown in (a).

Using the discrete modulus constraint and evaluating (5) in specific tissue segments raises one additional difficulty. The MRI imaging, upon which the tissue segmentation is based, will typically be in Langrangian coordinates (in the uncompressed state) while the displacement, as measured with phase contrast, is obtained in Eulerian coordinates (in the compressed state). If the deformation can be treated as infinitesimal, then the Lagrangian segmentation can be registered to the Eulerian strain using linear interpolation. In the case of finite deformation, however, a coordinate transformation is necessary. In the latter case, the displacement-gradient tensor in the Lagrangian description $\nabla^0\mathbf{u}$ is obtained from the Eulerian displacement-gradient tensor $\nabla\mathbf{u}$ by [20]

$$\nabla^0\mathbf{u} = [\mathbf{I} - \nabla\mathbf{u}]^{-1} - \mathbf{I}. \tag{15}$$

The Lagrangian strain corresponding to the segmented volume is computed directly from $\nabla^0\mathbf{u}$.

III. Methods

The complete iterative elastography procedure is summarized in Fig. 1. The first step is MRI imaging of tissue which is followed by image segmentation to obtain the geometry of each tissue volume. AnalyzeAVW V 2.5 [21]: an image analysis package was used for image segmentation on the basis of image signal level. After MRI imaging, displacement data is acquired while the tissue undergoes quasi-static deformation. This data is acquired using a stimulated-echo phase contrast method [4]. It must be noted that unlike the previous step where MRI image of the entire tissue volume must be acquired, displacement data must be acquired only for a single slice which contains substantial regions of each of the discrete tissue types. Thus, we need only measure the strain in a single plane through the lesion. The iterative procedure begins with an initial guess for the tissues' Young's moduli. To provide an initial guess, we use the average values of the measured strain reciprocals obtained over the area of each tissue type. The ratio of these values are, thus, used as the initial Young's modulus ratios. To create a FE mesh, we process the segmented images using meshing techniques described in Samani *et al.* 2001 [16]. Using the created mesh and the tissues' Young's moduli, we employ ABAQUS for stress calculation. After stress calculation, the procedure is followed by modulus updating using (5). This equation yields a Young's modulus reciprocal value for each FE. The average of these values over each tissue volume is then calculated and its reciprocal obtained and used as the updated Young's modulus. At this stage, convergence is checked using two consecutive Young's modulus values E_{i+1} and E_i as follows:

$$\left\| \frac{E^{i+1} - E^i}{E^i} \right\| < tol \tag{16}$$

where tol is a small number. If this criteria is satisfied, the updated set of Young's modulus values is considered to be final, otherwise the iterative procedure is followed by stress calculation and then modulus updating. It must be noted that for stress calculation in 3-D cases, the updated modulus values obtained in the plane of interest are applied to the entire 3-D FE model. Moreover, stress calculation is done using the well-controlled compression plate motion as boundary conditions. We also demonstrate an alternate approach in which displacement data is acquired over an ROI in the slice containing the suspicious tumour rather than the entire slice. In this approach, stress calculation can be done over the ROI using the experimentally acquired displacement data to provide the boundary conditions. As a result, stress calculation can be done easily since the ROI and boundary conditions are straight forward. Assuming plane-strain conditions, it is necessary to obtain two components of displacement in a single plane to completely specify the boundary conditions. In terms of data acquisition, this is double the minimum requirement of the 3-D modeling approach described above. Beside stress errors resulting from the noisy boundary conditions, the other disadvantage of this approach is,

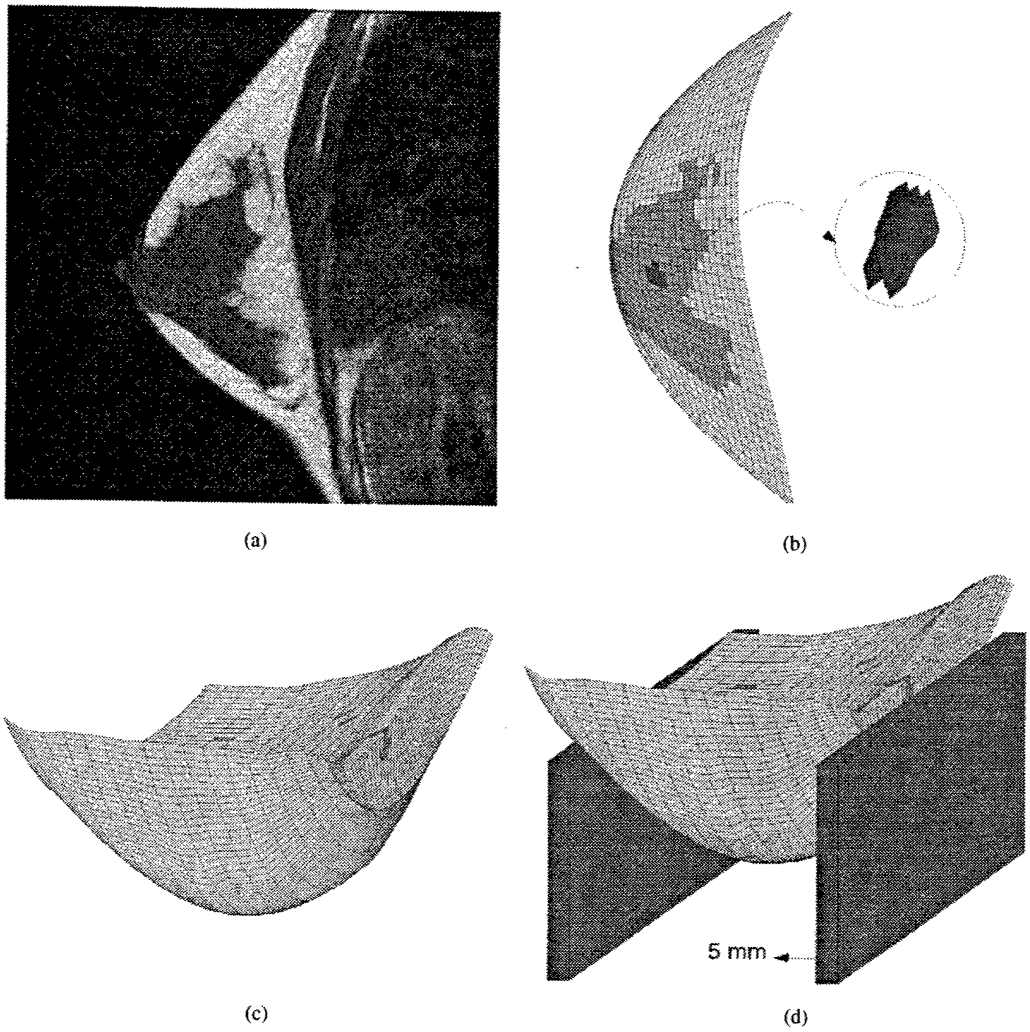

Fig. 3. FE model of the breast. (a) Magnitude image of a central slice through the breast. (b) FE mesh corresponding to the slice shown in (a) where the tumour shown in the circle is added. (c) FE mesh of the breast. (d) FE contact problem model for compression simulation.

therefore, the greater data acquisition requirement compared to former approach.

Simulations were performed in two and three dimensions to demonstrate various aspects of the method. In two dimensions, a simple circular inclusion phantom illustrated in Fig. 2 was simulated using a 64×64 grid. A 5% compression was applied with zero displacement boundary conditions in the plane of compression plates, displacement data was obtained using a plain strain FE model, and the central 32×32 grid of displacement data was extracted for analysis using the alternate reconstruction approach. In three dimensions, T1 weighted breast images of a healthy volunteer were acquired using a GE SIGNA 1.5-T scanner (GE Medical Systems, Milwakee, WI). Using body coil, a 2-D spin-echo pulse sequence was employed with $TR/TE =$ 300/9 ms and $\theta = 90°$ to acquire 16 sagittal images. A typical sagittal image of the breast is shown in Fig. 3(a) where regions of adipose tissue (bright) and fibroglandular tissue (dark) are easily resolved with high SNR. After image segmentation, an FE mesh illustrated in Fig. 3(b) and (c) was created. In Fig. 3(b), the FE mesh corresponding to the sagittal slice of Fig. 3(a) is depicted where a tumour is added. The presence of the tumour was simulated by altering the Young's modulus of appropriate elements in the 3-D model as shown in Fig. 3(b). To simulate a 5-mm compression resulting from two rigid plates, we used a 3-D FE contact problem model described in [16] as shown in Fig. 3(d). From this model, 3-D displacement data was calculated and used for Young's modulus reconstruction.

To test this technique with experimental data, a plastisol PVC phantom was constructed. The magnitude image of a central slice through this phantom is shown in Fig. 4(a). In this T2-weighted image, the central hard inclusion is seen as a dark hemi-circle, while the intermediate layer appears bright. This phantom was constructed in two stages, beginning with a 12-mm spherical "tumour", embedded in a surrounding layer representing "fibroglandular" tissue. This first surrounding layer was cut, gouged and sliced in a random fashion at many angles, and then encased in a second surrounding layer now representing "adipose". The resulting phantom had thus three separate volumes of distinct elasticity modulus, and presented both a complex strain field and realistic segmentation problem. The Young's moduli of the individual layers was measured independently using a uniaxial benchtop experiment, resulting in 48.0, 24.3, and 12.4 kPa for the inclusion, middle layer, and outer layer, respectively. The FE mesh of a slice corresponding

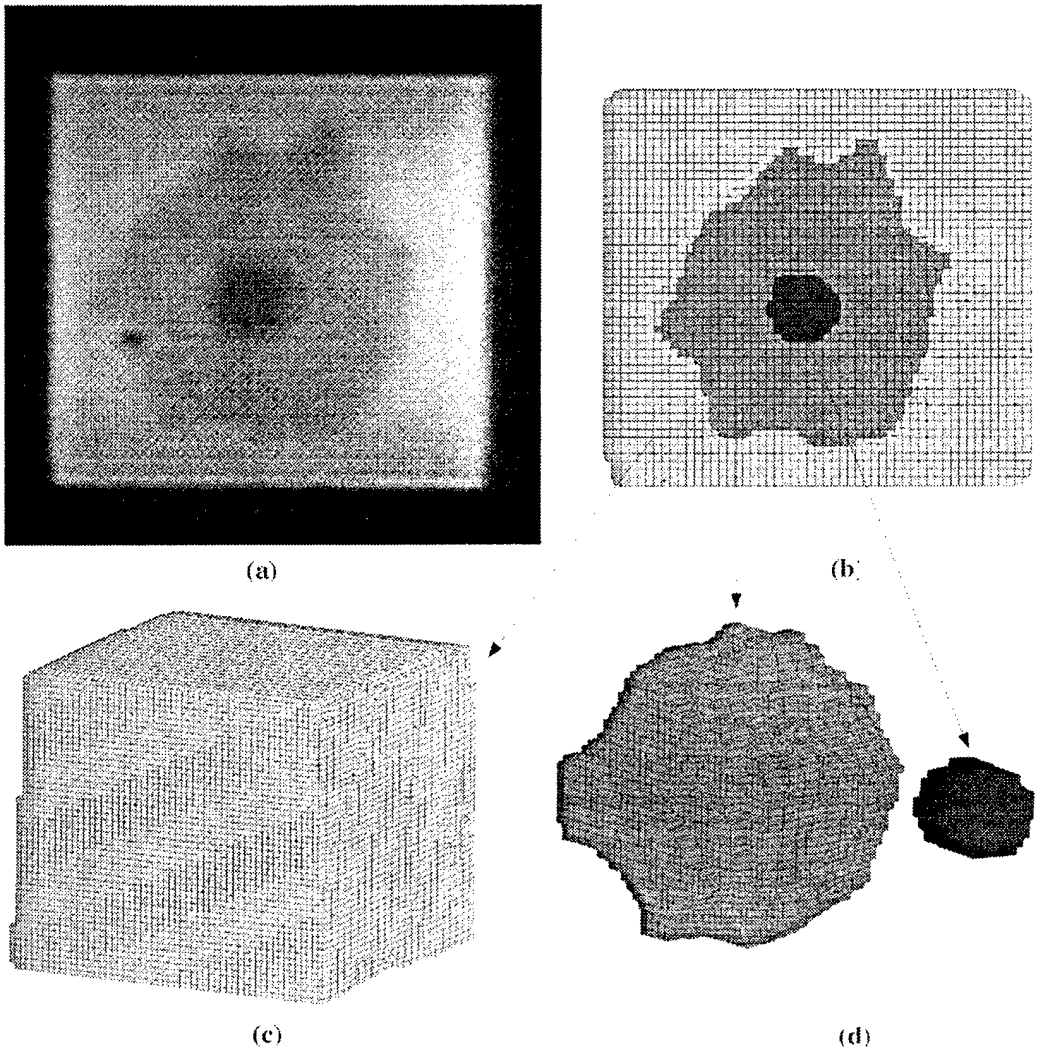

Fig. 4. FE model of the 3-D phantom. (a) Magnitude image of a central slice through the phantom where the circular inclusion and middle layer are shown. (b) FE mesh corresponding to the slice shown in (a). (c) Three-dimensional FE mesh of the phantom. (d) Three-dimensional FE mesh of the middle layer and inclusion.

to the image shown in Fig. 4(a), the phantom and its different layers are depicted in Fig. 4(b)–(d), respectively.

For image segmentation purposes, 3-D fast-spin echo imaging with $TR/TE = 2000/85$ ms and 48 echoes was performed over the entire volume of the phantom while in the uncompressed state. Using a compression device driven by an MR compatible ultrasonic motor as described in [15], quasi-static MR elastography with phase-contrast displacement encoding was performed on the phantom using a compression of 3.5 mm at the surface of the phantom, at a frequency of 1.5 Hz. For displacement data acquisition, we used a STEAM pulse sequence described in [15], with $TR/TE = 660/12$ ms and a mixing time T_m of 300 ms. All images and displacement data were acquired using a five-inch diameter surface coil.

IV. Results

The noise-free convergence of the 2-D simulation is shown in Fig. 5. Fig. 5(a) and (a′) depicts the reconstruction results where the inclusion was assumed to have a uniform modulus of three relative to the background. As it is shown in these graphs, convergence to the exact relative modulus was achieved using the strain reciprocals as initial guess. A second case was also studied where the inclusion was assumed to have a smooth 2-D Gaussian relative modulus with mean value of three. As shown in Fig. 5 (b) and (b′), the process converged to an average value of 3.2 which is slightly higher than three. Finally, the results of the unconstrained iteration where modulus averaging was not performed are shown in Fig. 5(c) and (c′). The latter result shows that after ten iterations, convergence is not only not achieved but also unlikely if the iteration is continued. This confirms our conclusion from (8) and indicates that the proposed method is appropriate only for the geometrically constrained problem.

To investigate the propagation of noise throughout the iterations and its impact on the reconstructed values, we have conducted a numerical experiment in which the simulated displacement data of the 2-D plane strain case was contaminated with noise. Two different levels of magnitude SNR were considered and their corresponding strain SNR values were calculated using (14). Based on each strain SNR value, the displacement data was

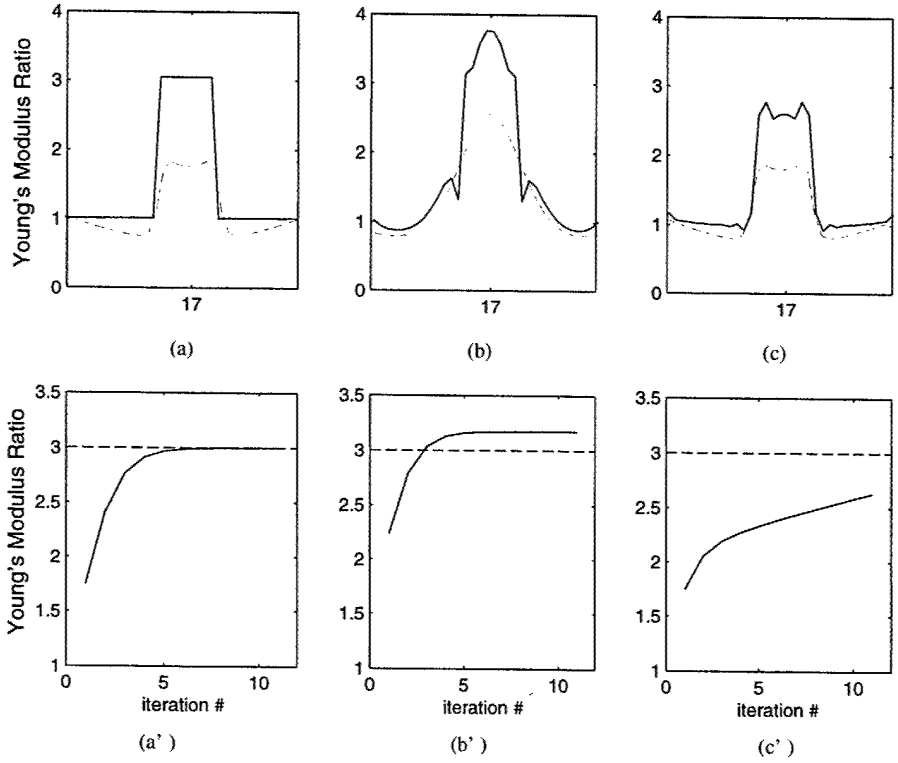

Fig. 5. Demonstration of convergence in 2-D noise-free simulation. (a) and (b) Profiles of the reconstructed modulus ratio through the inclusion (solid lines) and their corresponding strain reciprocal ratio profile (dashed lines) for the discrete and normal modulus distribution. (c) Profiles of the modulus ratio (dashed lines) and its corresponding strain reciprocal ratio obtained from incomplete reconstruction when averaging is not performed. (a′), (b′), and (c′) Modulus ratio versus iteration number correponding to (a), (b), and (c). (a′) indicates that convergence is rapid and exact where true modulus distribution is discrete while (b′) shows systematic error relative to the mean value of true modulus, and (c′) indicates that convergence cannot be achieved if modulus averaging is not performed.

TABLE I
SIMULATION OF THE EFFECTS OF EXPERIMENTAL NOISE ON THE RECONSTRUCTED MODULUS VALUES IN TWO DIMENSIONS

strain SNR	magnitude SNR	input modulus SNR	output modulus SNR
3.1	6.3	26.17	26.07
12.6	25.7	94.54	92.81

Two levels of SNR ranging from 6.3 to 25.7 were selected. For each SNR level, ten noise instances were generated and, with a set of initial guess modulus values, a sequence of ten iterations was executed. The modulus SNR, is defined as the ratio of the mean value to the standard deviation of the modulus set values of the inclusion, in the first and final iterations. These values suggest that, statistically, there is no significant change in the noise throughout the course of iteration.

contaminated by ten independent normally distributed noise instances. The strategy here, is to input a set of modulus values into the iterative process, calculate the corresponding output values and, thus, compare the input and output sets in a statistical sense. As such, with an inclusion size of $N = 51$ pixels, we calculated a set of ten modulus values based on (10) corresponding to each SNR value. These values (input) were used as initial guess with the ten displacement data sets contaminated by noise and after ten iterations another modulus value set (output) was obtained. We define modulus SNR as the ratio of the mean value to the standard deviation of a set of the inclusion's modulus values. These values are calculated for the input and output modulus sets and summarized in Table I. The results in this table indicate that there is no statistically significant difference between the input and output SNR values. This suggests that, with moderate SNR values, the geometrically constrained iteration procedure does not accumulate noise.

For 3-D breast elastography using simulated data, we assumed Young's modulus values of 2.0, 10.0, 50.0, and 25.0 kPa for fat, fibroglandular tissue, tumour, and the skin, respectively. Accordingly, 5-mm compression was simulated using the 3-D FE contact problem model, and the displacement component of the slice containing the tumour in the compression direction was calculated. These displacements were contaminated by normally distributed noise to simulate SNR values of 30 and 10. Using this iterative technique, as shown in Fig. 6(a) and (b), convergence was achieved after eight iterations where each iteration took about 30 min. This result indicates that with a tumour size of $N = 13$ elements accurate relative modulus can be achieved with this level of SNR.

The experimental results obtained with the PVC plastisol phantom under 2-D plane strain analysis are presented in Fig. 6(c) and (d). Fig. 6(c) depicts the vertical component of the measured strain from which initial modulus ratios were calculated. Using the measured strain, the reconstruction procedure converged after 11 iterations where each iteration took about 100 min. As shown in Fig. 6(d), the final reconstructed modulus ratio is roughly 3.4:2.2:1 which indicates a maximum error of 12%.

V. CONCLUSION AND DISCUSSION

We have described an iterative method for deriving modulus distributions from displacement vector fields obtained with MR elastography. The key feature of the method is the application of geometrical constraints at each step of the iteration. It is our

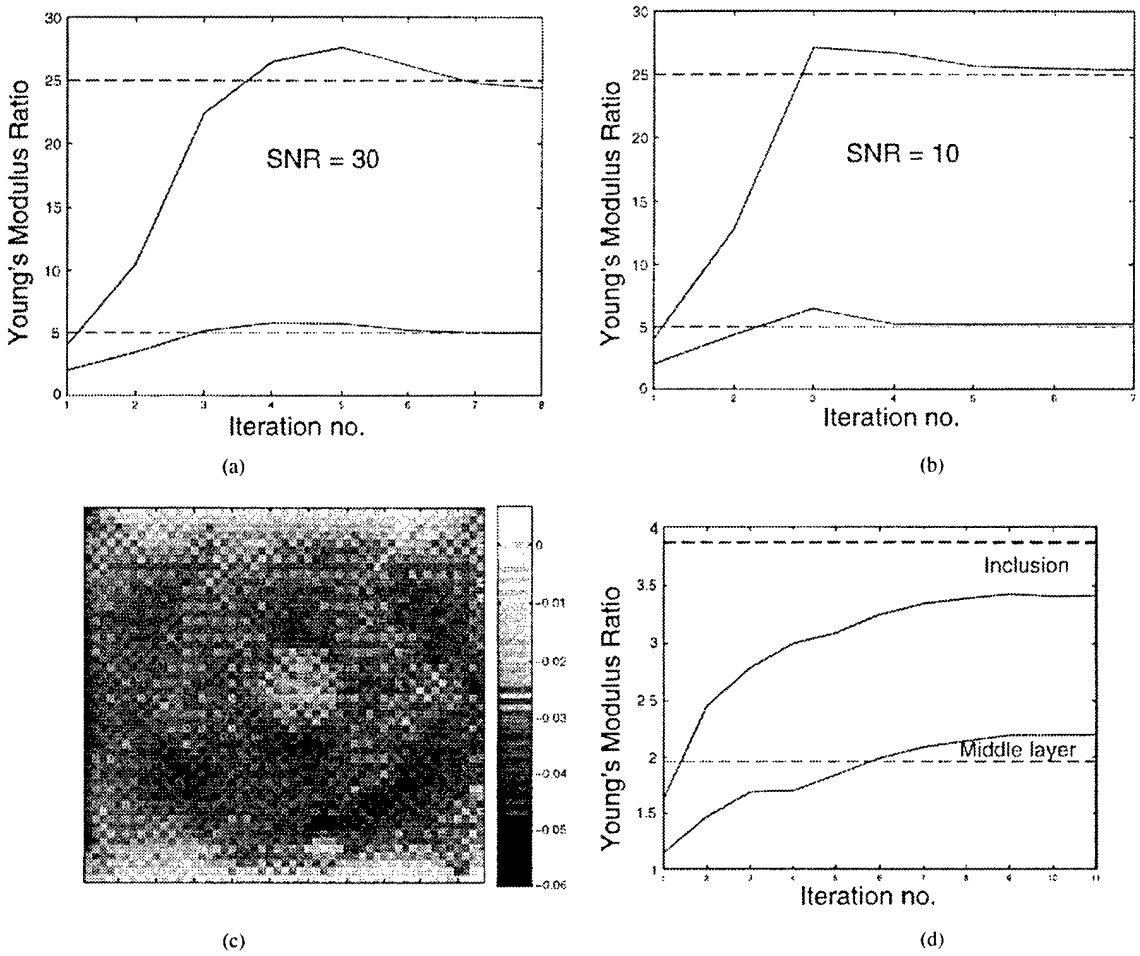

Fig. 6. Modulus reconstruction results. (a) and (b) Convergence of $E_{\rm fib}/E_{\rm fat}$ and $E_{\rm tum}/E_{\rm fat}$ of the breast to the true values (dashed lines) for SNRs of 30 and ten where $E_{\rm fat}$, $E_{\rm fib}$, and $E_{\rm tum}$ are the Young's modulus of fat, fibroglandular tissue, and tumour, respectively. (c) Measured strain in the phantom's middle slice. (d) Convergence of $E_{\rm fib}/E_{\rm fat}$ and $E_{\rm tum}/E_{\rm fat}$ where $E_{\rm fat}$, $E_{\rm fib}$, and $E_{\rm tum}$ are the Young's modulus of the outer layer, middle layer, and the inclusion, respectively. The reconstruction results indicate that reconstruction error for both the middle layer and the inclusion does not exceed 12%.

assumption that with any elastography study in the breast, there will be a conventional contrast-enhanced 3-D volume study immediately preceding it. In this paper we have demonstrated how the 3-D volume study could be used to identify the exact location of the tumor, and to segment the breast volume into three tissue types (adipose, fibroglandular, tumor). We make the important assumption that each tissue type has constant elasticity properties throughout the breast volume.Recent breast MRE results from other investigators such as Weaver *et al.* [22] indicate that normal breast tissues exhibit very little stiffness heterogeneity while to verify tumors' homogeneity, resolution was not sufficient. In situations where this type of simplification is appropriate, the iterative method described above provides a rapidly convergent technique that is robust in the presence of noise. Further investigation is required to verify the tissue homogeneity assumption. In case this assumption is not completely valid, one possible remedy would be to subdivide each tissue volume into a number of regions over each of which the tissue modulus is assumed to be constant.

A variant of the method in which the experimentally measured displacement vector is used as a complete boundary condition in the iteration has also been described. The advantage of this approach is that the reconstruction field-of-view may be made arbitrarily small to focus in on just the tumor and consequently reduce computation time in the iteration, but the drawback is the presence of experimental noise in the boundary conditions. This approach is primarily useful for plane strain cases where it can be implemented with just two components of displacement in a single plane. In unconstrained 3-D deformation, the use of external physical boundaries in the forward solution of (4), as described above, is more efficient.

We have conducted a numerical experiment to investigate noise propagation in the inversion procedure and we concluded that, with moderate SNR values, the iterative procedure does not accumulate noise. Another important source of error is segmentation. One way to investigate the impact of segmentation errors on the reconstructed values in a statistical sense is to conduct a numerical experiment similar to the noise propagation experiment. In this experiment, using a numerical model such as the breast model in Fig. 3, a number of pixels located around tissue interfaces are randomly selected and their tissue type is altered to simulate segmentation errors. With the resulting model and using displacement data generated from the original model, modulus values can be reconstructed. This process must be repeated a number of times (e.g., ten times) each time with a different set of pixels around tissue interfaces altered. Finally, the

reconstructed values are processed and errors calculated. This experiment is beyond the scope of this paper; however, based on the breast numerical experiment and the phantom experiment, it can be concluded that the 12% error is mainly due to factors other than data noise such as segmentation and FE modeling.

A further concern with the in-vivo application will be increased complexity in modeling the 3-D compression of the breast tissue. The phantom objects used in the experiments described above were prepared with sharply defined right-angle corners and edges. In contrast, the compression of the breast must be modeled as a 3-D contact problem [16], which is more computationally challenging. Future investigation will consider approximations to the stress estimation that may relieve the computational burden of the full contact problem treatment. For increased accuracy, there is the possibility of extending the method when the tissues are modeled as hyperelastic materials. In this case the modulus update calculation will involve solving a small nonlinear equations system.

As a final note, the methodology presented in this paper is not limited to MRI modality and can be implemented with other modalities such as ultrasound. It has been shown that ultrasound is capable of displacement measurement with moderate SNR [8], [9]. Ultrasound, however, does not provide magnitude images that are useful for segmentation purposes. A possible remedy would be to use corresponding strain images as a means for segmentation.

REFERENCES

[1] P. S. Wellman, "Tactile Imaging," Ph.D. dissertation, Harvard Univ., Cambridge, MA, 1999.

[2] A. J. Lawrence, R. Muthupillai, P. J. Rossman, J. A. Smith, A. Manduca, and R. L. Ehman, "Magnetic resonance elastography of the breast: Preliminary experience," in *Proc. ISMRM, 6th Annu. Meeting*, Sydney, Australia, Apr. 1996, p. 233.

[3] R. Sinkus, J. Lorenzen, D. Schrader, M. Lorenzen, M. Dargatz, and D. Holz, "MR-elastography applie to in-vivo MR-mammography," in *Proc. ISMRM, 7th Annu. Meeting*, Philadelphia, PA, May 1999, p. 259.

[4] T. L. Chenevert, A. R. Skovoroda, M. O'Donnell, and S. Y. Emelianov, "Elasticity reconstructive imaging by means of stimulated echo MRI," *Magn. Reson. Med.*, vol. 39, pp. 482–490, 1998.

[5] R. Muthupillai, D. J. Lomas, P. J. Rossman, J. F. Greenleaf, A. Manduca, and R. L. Ehman, "Magnetic resonance elastography by direct visualization of acoustic strain waves," *Science*, vol. 269, pp. 1854–1857, 1995.

[6] R. Sinkus, J. Lorenzen, D. Schrader, M. Lorenzen, M. Dargatz, and D. Holz, "Hi-resolution tensor MR elastography for breast tumour detection," *Phys. Med. Biol.*, vol. 45, pp. 1649–1664, 2000.

[7] A. R. Skovoroda, S. Y. Emelianov, and M. O'Donnell, "Tissue elasticity reconstruction based or ultrasonic displacemement and strain images," *IEEE Trans. Ultrason., Ferroelect., Freq. Contr.*, vol. 42, pp. 747–765, 1995.

[8] F. Kallel and M. Bertrand, "Tissue elasticity reconstruction using linear perturbation method," *IEEE Trans. Med. Imag*, vol. 15, pp. 299–313, June 1996.

[9] J. Ophir, F. Kallel, T. Varghese, M. Bertrand, Cespedes I, and H. Ponnekanti, "Elastography: A systems approach," *Int. J. Imag. Syst. Tech.*, pp. 89–103, 1997.

[10] J. Bishop, A. Samani, J. Sciarreta, and D. B. Plewes, "Two-dimensional MR elastography: Methodology and noise analysis," *Phys. Med. Biol.*, vol. 45, pp. 2081–2091, 2000.

[11] M. M. Doyley, P. M. Meaney, and J. C. Bamber, "Evaluation of an iterative reconstruction method for quantitative elastography," *Phys. Med. Biol.*, vol. 45, pp. 1521–1540, 2000.

[12] A. Manduca, R. Muthupillai, P. J. Rossman, J. F. Greenlead, and R. L. Ehman, "Image processing for magnetic resonance elastography," *Proc. SPIE*, vol. 2710, pp. 616–623, 1996.

[13] E. E. W. van Houten, J. B. Weaver, M. Miga I, F. E. Kennedy, and K. D. Paulsen, "Elasticity reconstruction from experimental MR displacement data: Initial experience with an overlapping subzone finite element inversion process," *Med. Phys.*, vol. 27, pp. 101–107, 2000.

[14] A. Samani, J. Bishop, J. Sciarretta, and D. B. Plewes, "Breast magnetic resonance elastography: A new reconstruction technique using MRI derived constraints," in *Proc. ISMRM, 8th Annu. Meeting*, Denver, CO, Apr. 2000, p. 2174.

[15] D. B. Plewes, J. E. Bishop, A. Samani, and J. Sciarretta, "Visualization and quantification of breast cancer biomechanical properties with magnetic resonance elastography," *Phys. Med. Biol.*, vol. 45, pp. 1591–1610, 2000.

[16] A. Samani, J. B. Bishop, M. J. Yaffe, and D. B. Plewes, "Biomechanical 3-D finite element modeling of the human breast using MRI data," *IEEE Trans. Med. Imag.*, vol. 20, pp. 271–279, Apr. 2001.

[17] S. Saada, *Elasticity, Theory and Applications* New York, 1989.

[18] K.-J. Bathe, *Finite Element Procedures in Engineering Analysis*. Englewood Cliffs, NJ: Prentice-Hall, 1996.

[19] *ABAQUS, Theory Manual*, Hibbit, Karlsson, and Sorenson, Pawtucket, RI, June 1998.

[20] D. S. Chandraserharaiah and L. Debnath, *Continuum Mechanics*: Academic Press, 1994.

[21] *AnalyzeAVW, Ver. 2.5*, Mayo Foundation, Rochester, MN, 1998.

[22] J. B. Weaver, E. E. W. van Houten, M. I. Miga, F. E. Kennedy, and K. D. Paulsen, "Initial performance of three dimensional steady state MR elastography," in *Proc. ISMRM, 9th Annu. Meeting*, Glasgow, U.K., Ap. 2001, p. 1638.

[20] Y. Cao and D. N. Levin, "Using prior knowledge of human anatomy to constrain MR image acquisition and reconstruction: Half k-space and full k-space techniques," *Magn. Reson. Imag.*, vol. 15, pp. 669–677, 1997.

[21] J. Tsao, "Prior-information-driven magnetric resonance imaging and magnetic resonance spectroscopic imaging," Ph.D. dissertation, Dept. Biophys. Computational Biol., Univ. Illinois at Urbana-Champaign, Urbana-Champaign, IL, 2001.

[22] Z. P. Liang, T. Constable, E. M. Haacke, F. Boada, M. Smith, and P. C. Lauterbur, "Constrained reconstruction methods in MR imaging," *Rev. Magn. Reson. Med.*, vol. 4, pp. 67–185, 1992.

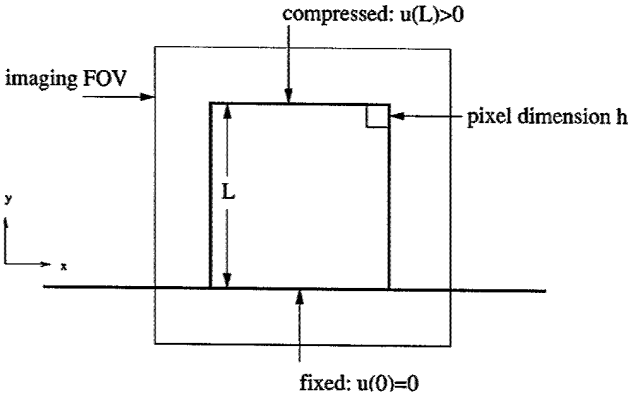

Fig. 1. Two-dimensional (2-D) geometry of a homogeneous phantom undergoing compression, illustrating the quantities discussed in the theory and experimental methods.

A Signal/Noise Analysis of Quasi-Static MR Elastography

Jonathan Bishop*, Abbas Samani, Justin Sciarretta, Chris Luginbuhl, and Donald B. Plewes

***Abstract*—In quasi-static magnetic resonance elastography, strain images of a tissue or material undergoing deformation are produced. In this paper, the signal/noise (S/N) ratio [SNR] of elastographic strain images, as measured by a phase-contrast technique, is analyzed. Experiments are conducted to illustrate how diffusion-mediated signal attenuation limits maximum strain SNR in small displacement cases, while the imaging point-spread function limits large displacement cases. A simple theoretical treatment agrees well with experiments and shows how an optimal displacement encoding moment can be predicted for a given experimental set of parameters to achieve a maximum strain SNR. A further experiment demonstrates how the limitation on strain SNR posed by the imaging point-spread function may potentially be overcome.**

***Index Terms*—MR, elastography, strain, imaging.**

I. Introduction

Elastography is an imaging technique that can display certain biomechanical properties of soft tissue, and which may offer improved specificity in the diagnosis of diseases such as breast cancer. The success of the technique depends on the extent to which disease process alters the biomechanical properties of the tissue. For example, cancerous tumours are frequently found to be harder than surrounding normal tissue [1]. While the concept of elastography was first described in the ultrasound literature [2]–[4], a large body of work has also been published in the magnetic resonance (MR) imaging literature. In MR elastography (MRE), two fundamental approaches have been demonstrated. Static [5] and quasi-static deformation [6] techniques fall into one broad category, while shear wave imaging with oscillatory [7], [8] stresses applied mechanically at the object surface, or remotely by other means such as ultrasound [9] fall into another. Common to many of these methods is the use of displacement-encoding by phase contrast [10].

In the case of static and quasi-static methods for MRE, the material strain may be computed from the measured displacement. Strain is not a direct measure of the underlying material property (i.e., the elastic modulus). However, strain images may be rapidly and unambiguously computed, while methods of solving for elastic modulus from displacement data are more involved [11], [12]. Furthermore, strain images can provide a limited degree of quantitation, since a strain ratio may be interpreted as a measure of relative elastic modulus in the case of simple geometries such as focal masses, when conditions of linear elasticity hold [6].

The goal of this work is to provide a signal/noise (S/N) analysis of strain images acquired with MRE. It specifically focuses on the static and quasi-static deformation technique as originally described in [5]. Previous analyzes have been conducted by simulation [13] and in the human myocardium [14]. In this paper, a simple theoretical treatment is shown to agree well with experimental measurements in phantom objects under controlled conditions. The results demonstrate that diffusion sensitivity is significant and may outweigh the imaging point-spread function as an upper limit on achieveable strain SNR. For cases in which the point-spread function is the limiting factor, it is also shown how that limitation may be partially overcome.

MR techniques for measuring tissue motion and computing strain are also used in the large body of work on myocardial strain imaging. Aside from the recent work of Aletras [14], the motion-encoding techniques used for myocardium are primarily tagging [15] and velocity-encoded phase contrast [16], [10]. The contents of this paper do not apply to tagging or velocity-encoded phase contrast techniques, as the SNR characteristics have been studied elsewhere [17], [18].

II. Theory

In quasi-static MRE, the S/N behavior of strain is composed of several factors which include the amplitude of deformation applied, the base SNR of the magnitude image, intra-voxel dephasing effects due to the encoding gradients, and the noise properties of discrete differentiation. To begin with, consider an object of height L which is compressed at the top surface by an amount $u(L)$ in the vertical (y) direction and fixed at the bottom surface (Fig. 1). Assume that the stimulated echo pulse sequence of Fig. 2 is used to measure vertical displacement $u(y)$, with gradient zeroth-moment of $\phi_d = \gamma G \tau$. The phase signal within the object Θ will be proportional to vertical displacement u as a function of height

$$\Theta(y) = 2\pi\phi_d u(y), \quad \Theta(0) = u(0) = 0. \tag{1}$$

Manuscript received May 14, 2001; revised August 1, 2001. This work was supported in part by the National Cancer Institute of Canada. The Associate Editor responsible for coordinating the review of this paper and recommending its publication was M. W. Vanneir. *Asterisk indicates corresponding author.*

*J. Bishop is with Colorado Medtech, 1811 Left Hand Circle, Longmont, CO 80501 USA (e-mail: jbishop@cmed.com).

A. Samani, J. Sciarretta, C. Luginbuhl, and D. B. Plewes are with the Department of Medical Biophysics, University of Toronto, Toronto, ON M4N 3M5 Canada.

Publisher Item Identifier S 0278-0062(01)10003-0.

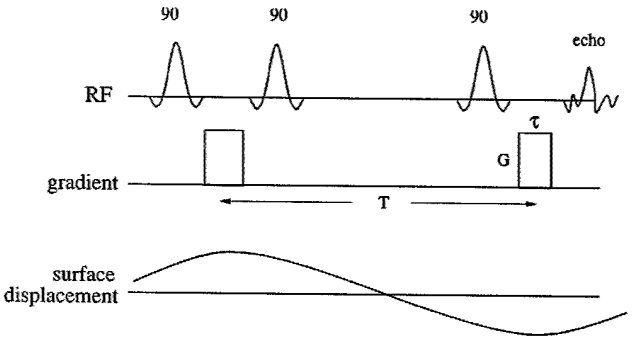

Fig. 2. Stimulated-echo pulse sequence used for phase-contrast displacement encoding.

The average gradient of the phase is

$$\frac{d\Theta}{dy} \simeq \frac{\Theta(L)}{L} = \frac{\theta}{h} \tag{2}$$

where θ is the average phase dispersion per pixel, and h is the size of a pixel. Since strain is an expression of displacement/unit of undeformed length, this average phase gradient can be directly interpreted as a measure of strain.

In a phase image, the pixel noise σ_p—expressed as a standard deviation in units of radians (rad)—is governed by the signal magnitude, A, and the standard deviation of the noise at the in-phase and quadrature channels of the A/D convertor, $\sigma = \sigma_i = \sigma_q$ [19]

$$\sigma_p = \frac{\sigma}{A}\frac{1}{\sqrt{2}} = \frac{1}{\sqrt{2}\mathrm{SNR}}. \tag{3}$$

An extra factor of $1/\sqrt{2}$ has been included since phase contrast imaging is usually conducted with two acquisitions subtracted to remove errors due to B_0 inhomogeneity, and it is assumed that $A \gg \sigma$.

The signal magnitude A is modulated by several different factors. The most significant is the diffusion sensitivity of the large gradient moments required for displacement encoding. This effect is modeled as an exponential signal decay $e^{-\phi_d^2(T-\frac{\tau}{3})D}$ [20] where the separation of displacement-encoding gradient pulses is given by T, the pulse width by τ, and D is the diffusion coefficient. In addition to diffusion, the data acquisition sampling results in a sinc-shaped point-spread function. In this paper, it is assumed that the imaging field-of-view will be selected to closely match the object size, and that the phase variations due to displacement encoding are generally smooth. In this case, the magnitude signal loss incurred by the point-spread function is "all-or-nothing" at the limit of $\theta = \pi$ [21]. Finally, the effect of T_2 has been omitted from this expression as explained below in methods.

To compute the phase gradient of (2), a differentiation operator must be applied. We consider here a simple numerical approximation of differentiation using a low-order interpolating polynomial [22]. It should be noted that this technique has no specific noise filtering or smoothing properties. Since only first-order differentiation is required for strain imaging, it is often not necessary to filter noise. In contrast, techniques of elasticity reconstruction that involve second or higher-order differentiation [23] would likely require additional noise filtering, using Savitsky–Golay algorithms [24] or similar.

Column two of Table I shows the first derivative operator for several different low-order interpolating polynomials, as a linear combination of terms required to estimate the derivative of function f at position 0. In general, the accuracy of the derivative estimate increases with the order of the interpolating polynomial. The noise figure of each operator

TABLE I
DISCRETE APPROXIMATION TO FIRST DERIVATIVE FOR SEVERAL LOW-ORDER INTERPOLATING POLYNOMIALS

Order	Terms	Noise Figure
1	$\frac{f_1-f_0}{h}$	$\frac{\sqrt{2}}{h}$
2	$\frac{f_1-f_{-1}}{2h}$	$\frac{1}{h}\frac{1}{\sqrt{2}}$
3	$\frac{2f_2-3f_1+6f_0-5f_{-1}}{6h}$	$\frac{1}{h}\sqrt{\frac{74}{36}}$
4	$\frac{f_2-8f_1+8f_{-1}-f_{-2}}{12h}$	$\frac{1}{h}\sqrt{\frac{130}{144}}$

can be computed by a standard propagation of errors analysis, assuming that noise statistics are locally constant, and are shown in column three of the table. The noise figure is the multiplicative factor by which the discrete differentiation will alter the phase noise σ_p.

Selecting the central difference approximation (second-order polynomial) for its minimum noise figure, then the phase gradient noise will be determined by combining (3) and the noise figure from Table I

$$\sigma_{pg} = \frac{1}{\sqrt{2}h}\cdot\frac{1}{\sqrt{2}\mathrm{SNR}}. \tag{4}$$

Since strain is a unitless quantity, there is no need to convert phase to units of displacement before computing the derivative. The ratio of (2) and (4) may, therefore, be interpreted directly as strain SNR

$$\mathrm{SNR}_e = \begin{cases} 2\mathrm{SNR}\theta e^{-\phi_d^2(\Delta-\frac{\tau}{3})D}, & \theta < \pi, \\ 0, & \theta > \pi \end{cases} \tag{5}$$

where the effects of diffusion and point-spread function have been included as described above. The quantity θ is dependent on two parameters (surface displacement $u(L)$ and encoding sensitivity ϕ_d) which can be freely varied in an experiment. However, we will assume that the choice of displacement $u(L)$ is fixed such that the object strain is as large as possible within the regime of linear elasticity (usually <10%). Note that the Fourier pixel size should be as large as possible given the features within the object that must be resolved, in order to maximize the magnitude SNR. Maximizing the pixel size also reduces the effects of diffusion since the gradient strength ϕ_d required to achieve the desired phase dispersion/pixel is minimized.

For a small compression amplitude $u(L)$, the ability to increase the strain SNR by increasing the phase encoding/pixel θ may be limited by diffusion effects, and there will be an optimal value for the quantity θ. For large $u(L)$ however, the Nyquist limit for discretely sampled data of π rad of phase/pixel [21] is most likely to be the limiting factor on strain SNR. In certain circumstances, however, it may be possible to exceed this limitation. If the spins are prewarped with a phase/pixel of θ_{pre} opposite to the anticipated degree of motion-encoding, then the net phase dispersion following displacement encoding may be retained within the range of $\pm\pi$ rad/pixel. In this case, the phase gradient is computed by

$$\frac{d\Theta}{dy} = \frac{\theta + \theta_{\mathrm{pre}}}{h}. \tag{6}$$

Since the prewarp phase θ_{pre} is not measured data, it is noise-free and the SNR of the strain data is increased relative to that of the raw phase data. A suitable value of θ_{pre} may be estimated from (1).

In addition to random noise discussed above, coil sensitivity profiles also affect signal magnitude and phase noise. In MRE of the breast, detectors are typically arrays of surface coils with significant spatial variations in sensitivity. When making an experimental measurement of phase noise statistics over a large region-of-interest (ROI), these sensitivity variations will affect the result. In (3), the term $1/A$ can be in-

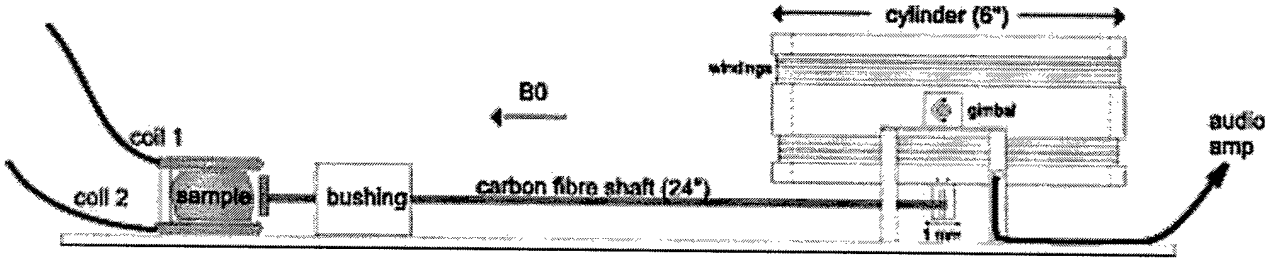

Fig. 3. Experimental apparatus for quasi-static MRE. An alternating current of 300 mA (peak) is delivered to the coil windings from an audio amplifier at a frequency of 2 Hz. The cylinder on which the windings are mounted is free to rotate about the gimbal axis under the torque due to the external magnetic field. A carbon-fiber shaft attached to the coil winding cylinder delivers a compressive force to the sample which is placed in between an array of two 25 mm coils. The sample is constrained from expanding in the vertical direction but free to expand in the direction out of the page.

terpreted as a variable with mean $\langle 1/A \rangle$ and variance $\sigma^2_{1/A}$. Expanding (3) to account for the variation in $1/A$

$$\begin{aligned}\sigma_p^2 &= \frac{1}{2}\left(\sigma^2\left\langle\frac{1}{A}\right\rangle^2 + \sigma^2_{\frac{1}{A}}\langle\sigma\rangle^2\right)\\ &= \frac{1}{2}\left(\sigma^2\left\langle\frac{1}{A}\right\rangle^2 + \left[\left\langle\frac{1}{A^2}\right\rangle - \left\langle\frac{1}{A}\right\rangle^2\right]\sigma^2\right)\\ &= \frac{\sigma^2}{2}\left\langle\frac{1}{A^2}\right\rangle \end{aligned} \tag{7}$$

where angle brackets $\langle\ \rangle$ have been used to denote expected value. The result of (7) is an effective phase variance that includes the effect of the coil sensitivity over the measurement ROI. The above expansion assumes that $1/A$ has a normal probability density, so the resulting expression is only an approximation of the truth. The phase standard deviation can then be written

$$\sigma_p = \frac{1}{\sqrt{2}}\frac{1}{\mathrm{SNR}}\left[\sqrt{\left\langle\frac{1}{A^2}\right\rangle}\langle A\rangle\right] \tag{8}$$

where the extra term in square brackets can be interpreted as a correction factor due to the effect of coil sensitivity variation. Of course, if the phase noise statistics are measured in a single pixel over multiple repetitions of an imaging experiment, then it is not necesssary to consider the coil sensitivity profile.

III. Methods

Imaging experiments were conducted with quasi-static compression and a stimulated echo pulse sequence gated to the compression cycle. A cubic phantom of dimension 25 mm, made of 1% agar, was compressed by 1 mm at a frequency of 2 Hz with an electromechanical device (Fig. 3). The detector was a two-coil volume phased array with inductive decoupling. Imaging time was adjusted to achieve a base SNR in the magnitude image of about 30. The motion encoding moment was then altered systematically to achieve phase accumulation/pixel of up to 1.5 rad. Each motion-encoded scan was followed by a zero motion scan with identical gradient waveforms, to enable correction for phase errors due to eddy currents. All scans were conducted at constant echo time, thus T_2 was not a variable in the analysis.

Magnitude reconstruction was obtained by a noise-weighted sum-of-the-squares. Since the complex data were available for both coils, the magnitude S/N for each coil was evaluated separately, and an estimate of the upper bound on the composite SNR produced under the assumption of zero noise correlation between the two coils. In comparison, deducing the SNR from the final composite image when noise correlations are present is a more difficult task [25]. Phase reconstruction was performed by combining the phase images arithmetically with equal weighting. Since all imaging was performed in the plane of symmetry between the two receiver coils, a magnitude-weighted phase reconstruction [26] was not used.

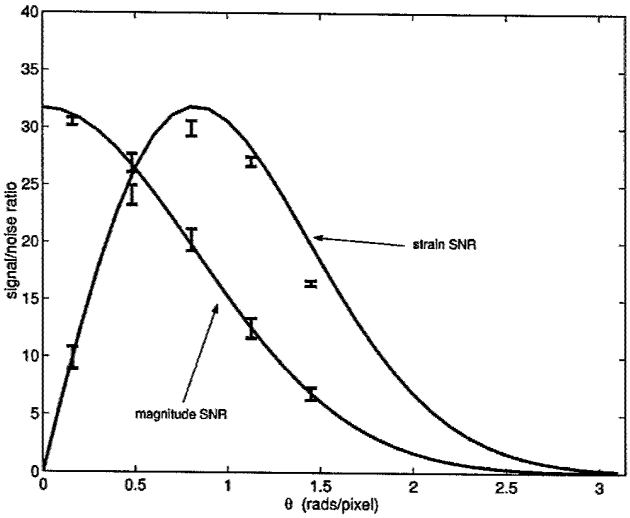

Fig. 4. Experimentally measured strain-to-noise ratio is plotted against the magnitude SNR of the data. As the phase dispersion (rads/pixel) increases, the strain SNR initially increases, but then falls off again as the magnitude SNR continues to decline through increased sensitivity to diffusion.

The phase gradient signal was computed by central difference of displacement, in the direction of compression. The mean gradient (or strain) was taken in a rectangular ROI along the central axis of the compressor piston through the center of the phantom. The phantoms were imaged in a moist condition to facilitate slipping at the boundaries and thus the strain was relatively constant within this rectangular ROI.

Phase noise was measured from the zero-motion images, in the same ROI as the strain signal. The phase noise included the effect of the coil sensitivity profile as described in (8). Therefore, a 2-D second-order polynomial surface was fitted to the magnitude image of each zero-motion scan. Since the phantom was homogeneous and uniform in its MR signal intensity, this second-order fit was interpreted as a good estimate of the coil sensitivity profile. The measured phase noise was then corrected according to (8), and the correction factors were typically 8%–10%. In addition, a correction for noise correlation was performed by measuring the correlation coefficient ρ in the noise of the two coils, and then simply dividing the phase variance by the quantity $1+\rho$. With this latter correction, the measured phase noise could now be compared directly to the estimated upper bound composite magnitude SNR which was formed above by assuming zero noise correlation.

The technique of prewarping the spin phase was demonstrated with a large amplitude compression experiment. A 6-cm block of plastisol

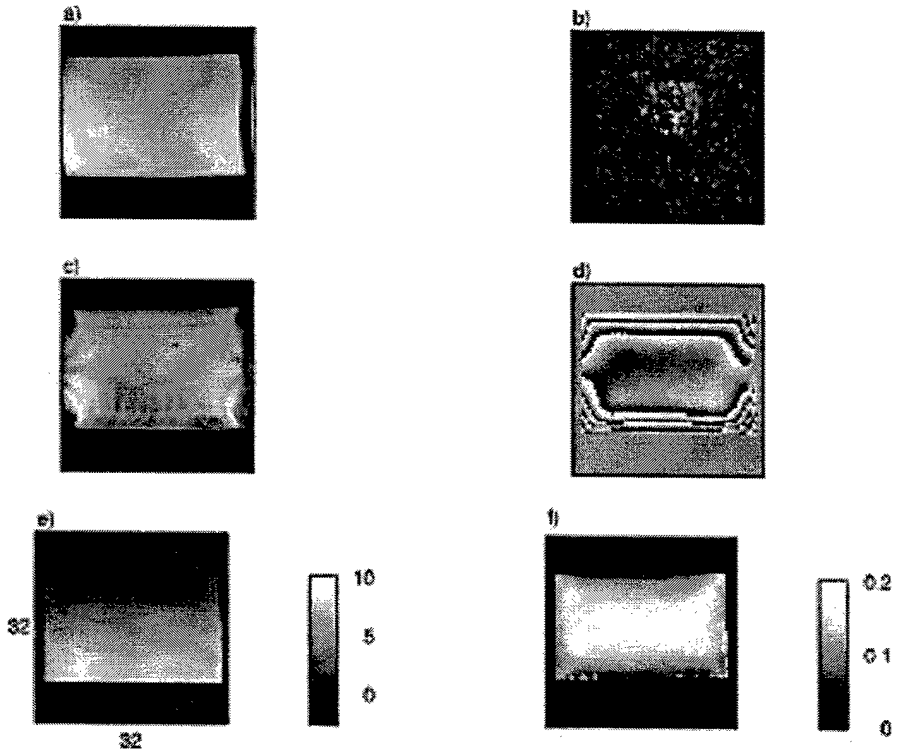

Fig. 5. Results of displacement encoding with spin prewarp. (a) Magnitude image at zero motion shows the rectangular phantom. (b) Magnitude image in the presence of motion, with a high degree of displacement encoding, shows complete elimination of the signal by the imaging point-spread function. (c) With the application of a spin prewarp gradient, the image signal is restored. (d) Raw phase image corresponding to magnitude image in (c). (e) Displacement reconstructed from (6) with greyscale units of mm. (f) Strain computed from the displacement with unitless greyscale. The strain image has had two extra rows of pixels masked off the top and bottom surfaces compared to the displacement image in (e), in order to hide the poor derivative estimates at the edges of the object.

PVC was compressed by 8 mm at 1.5 Hz with apparatus described in [27]. A motion encoding sensitivity of $\phi_d = 2.5$ cycles/mm was set, for a expected total phase shift of roughly 40π rad across the object, which was encoded with about 40 pixels in the 64×64 imaging matrix. Experiments were performed with and without a prewarp phase of approximately π rad/pixel.

IV. Results

Fig. 4 plots the results for experimental measurements of magnitude and strain SNR. The quantity θ, which represents the amount of displacement phase encoding in terms of rad/pixel, is plotted on the x axis. The SNR of the magnitude image drops off sharply as θ increases, which reflects the substantial diffusion sensitivity of the displacement encoding gradient pulses. Although the diffusion coefficient was not measured independently, a least-squares fit to the magnitude SNR data using the exponential term of (5) is shown by the solid line, and it yields an apparent diffusion constant of 2.05×10^{-9} m^2/s which is similar to the value for water [28]. This value includes the effect of material strain as noted in [29], but for purposes of this experiment no attempt was made to correct the data for that effect.

As expected, the strain SNR initially increases with increasing amount of displacement phase encoding θ. However, as diffusion effects become predominant they begin to counteract the gain in strain signal through an increase in the phase noise. The strain SNR goes through a maximum value, and then quickly drops off to zero well before the theoretical maximum encoding of π rad/pixel can be achieved, indicating that the experiment is limited by diffusion sensitivity. The predicted strain SNR from (5) is shown as a solid line, with partial agreement to experiment. The error bars on the experimental data are derived from the sample size of the measurement ROI (260 pixels). Note that to generate the theoretical curves as a function of magnitude SNR, no attempt was made to introduce the effect of coil sensitivity.

Fig. 5 plots the results of spin prewarping. In Fig. 5(a), the magnitude image of a zero-motion experiment demonstrates the rectangular PVC phantom. The magnitude image of the motion-sensitized experiment Fig. 5(b) indicates a total loss of signal due to the imaging point-spread function. By prewarping the spin phase by $\theta_{\text{pre}} \simeq \pi$ rad/pixel, the magnitude image of the same motion-sensitized experiment Fig. 5(c) indicates that the net phase/pixel has been returned to within the required range of $\pm\pi$. Fig. 5(d) shows the raw phase data corresponding to Fig. 5(c). In the central portion of the object, the phase due to motion encoding has been nearly balanced by the prewarp phase, so the net phase is nearly constant. Near the edges of the object, the effects of nonslip boundary conditions are seen, whereby there is reduced displacement and over-compensation by the prewarp phase. The boundary effects are particularly extreme in the corners of the object, such that some signal loss is even seen in the magnitude image (c). In 5(e), the displacement has been computed according to (6). In this image, the fixed surface (zero displacement) is at the top, and the compressed surface at the bottom shows roughly 8 mm of displacement. The corresponding strain image appears in 5(f). Again note the strain is near zero at the edges due to sticky boundary conditions, increasing to nearly 20% in the center of the object.

V. Discussion

In this paper, we have presented a S/N analysis of strain images that can be produced by static or quasi-static MRE. The results show that strain SNR can be predicted and maximized based on the magni-

tude SNR that can be achieved. Although the model predictions were slightly higher than the measured results, the model does correctly predict the displacement encoding sensitivity required to maximize the strain SNR.

In order to maximize strain SNR, there is an important size consideration. In any given experiment, the strain would typically be limited to about 5% to permit linear data processing and analysis. Therefore, the bigger the object, the bigger the absolute displacement that corresponds to a 5% strain. In the results described above, the displacement of 1 mm was not large enough to realize the theoretical maximum displacement encoding of π rad/pixel. Instead, diffusion signal attenuation became the limiting factor. As absolute displacement increases, the encoding moment can decrease in direct proportion, until the maximum encoding of π rad/pixel is reached.

The diffusion sensitivity noted above is a weakness of the quasi-static imaging methodology that was used experimentally, also noted in [14]. The motion encoding gradient pulses are played at the points of zero velocity in a sinusoidal deformation cycle, which means they are widely separated in time. For very hard or very small objects, the alternative is to implement an oscillating gradient solution [7]. While oscillating gradient methods are advantageous for measuring very small displacements, these typically require a wavelength-based or time-dependent analysis; a simple strain presentation is not available.

The strain SNR limitation due to the imaging point-spread function can be theoretically bypassed by prewarping the spin phase prior to displacement-encoding. In practical terms, it may be difficult to correct the entire spatial extent of the object within the imaging FOV unless lubricated, slippery boundary conditions are present. Where sticky boundary conditions exist, the phase dispersion may still be greater than $\pm\pi$ rad/pixel near the boundaries even as the center of object is corrected.

REFERENCES

[1] A. Sarvazyan, D. Goukassian, G. Maevsky, A. Oranskaja, A. Skovoroda, S. Emelianov, A. Klishko, G. Mironova, V. Sholokhov, and V. Ermilova, "Elasticity imaging as a new modality of medical imaging for cancer detection," in *Proc. Int. Workshop Interaction of Ultrasound with Biological Media*, Valenciennes, France, Apr. 5–9, 1994, pp. 69–81.

[2] J. Ophir, I. Cespedes, H. Ponnekanti, Y. Yazdi, and X. Li, "Elastography: A quantitative method for imaging the elasticity of biological tissues," *Ultrason. Imag.* , vol. 13, pp. 111–134, 1991.

[3] K. J. Parker, S. R. Huang, R. A. Musulin, and R. M. Lerner, "Tissue response to mechanical vibrations for sonoelasticity imaging," *Ultrasound Med. Biol.*, vol. 16, pp. 241–246, 1990.

[4] A. R. Skovoroda, S. Y. Emelianov, M. A. Lubinski, A. P. Sarvazyan, and M. O'Donnell, "Theoretical analysis and verification of ultrasound displacement and strain imaging," *IEEE Trans. Ultrason. Ferroelect. Freq. Contr.*, vol. 41, pp. 302–313, May 1994.

[5] T. L. Chenevert, A. R. Skovoroda, M. O'Donnell, and S. Y. Emelianov, "Elasticity reconstructive imaging by means of stimulated echo MRI," *Magn. Reson. Med.*, vol. 39, pp. 482–490, 1998.

[6] D. B. Plewes, J. E. Bishop, A. Samani, and J. Sciarretta, "Visualization and quantification of breast cancer biomechanical properties with magnetic resonance elastography," *Phys. Med. Biol.*, vol. 45, pp. 1591–1610, 2000.

[7] R. Muthupillai, D. J. Lomas, P. J. Rossman, J. F. Greenleaf, A. Manduca, and R. L. Ehman, "Magnetic resonance elastography by direct visualization of propagating acoustic strain waves," *Science*, vol. 269, pp. 1854–1857, 1995.

[8] R. Sinkus, J. Lorenzen, D. Schrader, M. Lorenzen, M. Dargatz, and D. Holz, "High-resolution tensor MR elastography for breast tumour detection," *Phys. Med. Biol.*, vol. 45, pp. 1649–1664, 2000.

[9] V. G. Andreev, F. N. Dmitriev, Y. A. Pishchal'nikov, O. V. Rudenko, O. A. Sapozhnikov, and A. P. Sarvazyan, "Observation of shear waves excited by focused ultrasound in a rubber-like medium," *Acoust. Phys.*, pp. 123–128, 1997.

[10] N. J. Pelc, R. J. Herfkens, A. Shimakawa, and D. R. Enzmann, "Phase contrast cine magnetic resonance imaging," *Magn. Reson. Quart.*, vol. 7, pp. 229–254, 1991.

[11] F. Kallel and M. Bertrand, "Tissue elasticity reconstruction using linear perturbation method," *IEEE Trans. Med. Imag.*, vol. 15, pp. 299–313, June 1996.

[12] E. E. W. van Houten, J. B. Weaver, M. I. Miga, F. E. Kennedy, and K. D. Paulsen, "Elasticity reconstruction from experimental MR displacement data: Initial experience with an overlapping subzone finite element inversion process," *Med. Phys.*, vol. 27, pp. 101–107, 2000.

[13] D. D. Steele, T. L. Chenevert, S. Y. Emelianov, and M. O'Donnell, "Signal-to-noise considerations in static displacement, stimulated echo NMR elasticity imaging," in *Proceedings of the IRMRM, 7th Meeting*, Philadelphia, PA, 1999, p. 1616.

[14] A. H. Aletras, R. S. Balaban, and H. Wen, "High-resolution strain analysis of the human heart with fast-DENSE," *J. Magn. Reson.*, vol. 140, pp. 41–57, 1999.

[15] E. A. Zerhouni, D. M. Parish, and W. I. Rogers *et al.*, "Human heart: Tagging with MR imaging—A method for noninvasive assessment of myocardial motion," *Radiology*, vol. 109, pp. 59–63, 1988.

[16] V. Wedeen, "Magnetic resonance imaging of myocardial kinematics. Technique to detect, localize, and quantify the strain rates of the active human myocardium," *Magn. Reson. Med.*, vol. 27, pp. 52–67, 1992.

[17] Z. Yudong, M. Drangova, and N. J. Pelc, "Estimation of deformation gradient and strain from CINE-PC velocity data," *IEEE-Trans. Med. Imag.*, vol. 16, pp. 840–851, Dec. 1997.

[18] W. G. O'Dell, C. C. Moore, W. C. Hunter, E. A. Zerhouni, and E. R. McVeigh, "Three-dimensional myocardial deformations: Calculation with displacement field fitting to tagged MR images," *Radiology*, vol. 195, pp. 829–835, 1995.

[19] T. Conturo and G. D. Smith, "Signal-to-noise in phase angle reconstruction: Dynamic range extension using phase reference offsets," *Magn. Res. Med.*, pp. 420–437, 1990.

[20] H. Y. Carr and E. M. Purcell, "Effects of diffusion on free precession in nuclear magnetic resonance experiments," *Phys. Rev.*, vol. 94, pp. 630–638, 1954.

[21] V. J. Wedeen, R. M. Weisskoff, and B. P. Poncelet, "MRI signal void due to in-plane motion is all-or-none," *Magn. Reson. Med.*, vol. 32, pp. 116–120, 1994.

[22] C. F. Gerald and P. O. Wheatley, *Applied Numerical Analysis*. Reading, MA: Addison-Wesley, 1984.

[23] A. R. Skovoroda, S. Y. Emelianov, and M. O'Donnell, "Tissue elasticity reconstruction based on ultrasonic displacemement and strain images," *IEEE Trans. Ultrason., Ferroelect., Freq. Contr.*, vol. 42, pp. 747–765, July 1995.

[24] P. A. Gorry, "General least-squares smoothing and differentiation by the convolution (Savitsky–Golay) method," *Analytic.Chem.*, vol. 62, pp. 570–573, 1990.

[25] C. Constantinides, E. Atalar, and E. McVeigh, "Signal-to-noise measurements in magnitude images from NMR phased arrays," *Magn. Reson. Med.*, vol. 38, pp. 852–857, 1997.

[26] M. A. Bernstein, M. Grgic, T. J. Brosnan, and N. J. Pelc, "Reconstructions of phase contrast, phased array multicoil data," *Magn. Reson. Med.*, vol. 32, pp. 300–334, 1994.

[27] J. Bishop, A. Samani, J. Sciarreta, and D. B. Plewes, "Two-dimensional MR elastography: Methodology and noise analysis," *Phys. Med. Biol.*, vol. 45, pp. 2081–2091, 2000.

[28] K. R. Harris and L. A. Woolf, "Pressure and temperature dependence of the self-diffusion coefficient of water and oxygen-18 water," *J. Chem. Soc. Faraday*, vol. 176, pp. 377–385, 1980.

[29] T. G. Reese, V. J. Wedeen, and R. M. Weisskoff, "Measuring diffusion in the presence of material strain," *J. Magn. Reson.*, ser. B, vol. 112, pp. 253–258, 1996.

Phys. Med. Biol. **45** (2000) 1591–1610. Printed in the UK PII: S0031-9155(00)06679-3

Visualization and quantification of breast cancer biomechanical properties with magnetic resonance elastography

Donald B Plewes, Jonathan Bishop, Abbas Samani and Justin Sciarretta

Department of Medical Biophysics, Imaging/Bioengineering Research Group, Sunnybrook and Women's College Health Sciences Centre, 2075 Bayview Avenue Toronto, Ontario, Canada M4N 3M5

E-mail: dbp@sten.sunnybrook.utoronto.ca

Received 4 August 1999, in final form 5 January 2000

Abstract. A quasistatic magnetic resonance elastography (MRE) method for the evaluation of breast cancer is proposed. Using a phase contrast, stimulated echo MRI approach, strain imaging in phantoms and volunteers is presented. First-order assessment of tissue biomechanical properties based on inverse strain mapping is outlined and demonstrated. The accuracy of inverse strain imaging is studied through simulations in a two-dimensional model and in an anthropomorphic, three-dimensional finite-element model of the breast. To improve the accuracy of modulus assessment by elastography, inverse methods are discussed as an extension to strain imaging, and simulations quantify MRE in terms of displacement signal/noise required for robust inversion. A direct inversion strategy providing information on tissue modulus and pressure distribution is described along with a novel iterative method utilizing *a priori* knowledge of tissue geometry. It is shown that through the judicious choice of information from previous contrast-enhanced MRI breast images, MRE data acquisition requirements can be significantly reduced while maintaining robust modulus reconstruction in the presence of strain noise. An experimental apparatus for clinical breast MRE and preliminary images of a normal volunteer are presented.

(Some figures in this article appear in colour only in the electronic version; see www.iop.org)

1. Introduction

Early detection is one of the primary requirements of successful cancer treatment and nowhere is this more important than in the case of breast cancer. Data linking reduced mortality from routine mammographic screening is now widely accepted in women over 50 (Baker 1982, European Society for Mastology Breast Cancer Screening Evaluation Committee 1993, Mathieson and Flensburg 1992), with growing evidence to suggest similar applicability to women over 40 (Sohn *et al* 1997, Bjurstam and Bjorneld 1994). Thus, early detection through screening mammography in conjunction with a programme of self-examination is considered central to breast cancer surveillance programmes throughout the world. In spite of the unquestionable successes of mammography, there remains an urgent need to improve both sensitivity and specificity of breast imaging methods for node-negative cancers. Developments in ultrasound imaging suggest a bright future for this inexpensive and widely available technology but it remains of limited value as a screening tool in comparison with high-quality mammography (Bassett and Kimme-Smith 1989). Isotopic methods with Sestamibi (Khalkhali *et al* 1995) and FDG tracers (Pietrzyk *et al* 1995) offer a number of intriguing possibilities for metabolic imaging, but resolution remains a severe limitation (Bombardien *et al* 1997).

0031-9155/00/061591+20$30.00

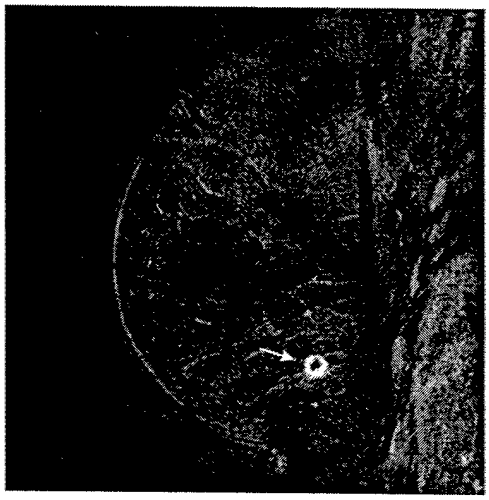

Figure 1. MRI image of a solitary breast cancer (arrow) undergoing rim enhancement. Imaging was performed with a gradient recalled sequence TR/TE/ = 9/4.3/30°, 5 min after the injection of 0.1 mmol kg^{-1} of Gd-DTPA.

Over the past decade a number of investigators have demonstrated the potential of MRI to detect breast cancers with very high sensitivity in all women, regardless of breast density (Orel *et al* 1994, Weinreb and Newstead 1995). While it has become widely recognized that MRI offers unique information on the extent of disease, staging and recurrence, it is still too expensive to be practical as a screening tool for the general population. However, a number of groups are exploring the use of MRI in the screening of high-risk women who present with mutations in the BRCA1 or BRCA2 genes or an extensive family history of breast cancer (Leach 1998, Kuhl *et al* 1999, Stoutjesdijk *et al* 1999). This small group of women represents an ideal population for screening by MRI as it is only 0.1–0.2% of the general population, yet is responsible for 5–10% of all breast cancer (Ford *et al* 1994).

While MRI can detect small enhancing masses in the breast, obtaining the exact diagnosis is difficult. Assessment of contrast uptake kinetics and lesion morphology can improve specificity (Nunes *et al* 1997, Daniel *et al* 1998), but unique differentiation of benign lesions from malignant cancers remains an ongoing challenge. This is illustrated in figure 1 which shows a focal mass of 5 mm in size. Morphology and kinetics suggest the presence of benign fibroadenoma, but diagnostic confidence can only be achieved through surgical biopsy. While core biopsy methods are minimally invasive, the need to reduce negative biopsies is paramount to minimize patient anxiety and health care costs. In this regard, there remains a critical need to seek new imaging methods which are specific for breast cancer. Amongst a number of interesting candidates, MR imaging of tissue biomechanics offers significant promise.

2. MR elastography

It is well known that variations in tissue elastic properties are associated with the presence of cancer and form the basis of clinical examination (Hill *et al* 1988). Properly applied, manual palpation can be a powerful, cost-effective and practical means of breast cancer detection, but is clearly restricted to relatively superficial, large, stiff masses (Newcomb *et al* 1991). Tissue stiffness, defined by Young's modulus, can span a range of 1–100 kPa amongst various

soft tissues in the body, with connective tissues and cartilage ranging from 100–1000 kPa and bone greater than 10^8 kPa (Fung 1993, Sarvazyan *et al* 1994). With regard to breast cancer, Anderson (1955) found scirrhous carcinoma of the breast to be extremely hard, while Sarvazyan *et al* (1995) has shown significant variation between normal breast tissue and various breast cancers in *ex vivo* measurements of 168 breast tissue specimens of varying histology. These studies suggest a 15-fold increase in the Young's modulus of breast cancer compared with normal fibroglandular tissue while fibroadenomas were only a factor of two stiffer than normal breast parenchyma. While significant variations in these values were present due to the measurement methods and tissue sample heterogeneity, these studies support observations that wide variations in tissue stiffness do exist between benign and malignant breast tumours.

The knowledge of tissue stiffness variability between normal and diseased tissues has stimulated the development of imaging methods aimed at imaging tissue elastic modulus in a quantitative manner. The general basis of these techniques is to induce motion within the tissue under investigation by either an external or internal mechanical stimulation. Conventional medical imaging modalities are then used to measure the spatial organization of the resulting deformation, from which the biomechanical properties can subsequently be extracted. While the majority of experience on this topic was pioneered within the ultrasound community, the advantages of magnetic resonance elastography (MRE) have recently become more widely recognized. With MRE, unlike ultrasound, motion can be measured in arbitrary directions with equal sensitivity.

The choice of mechanical deformation used for elastography generally falls into two categories, quasistatic or harmonic. Harmonic deformation perturbs tissues at frequencies of 50–1000 Hz, generating longitudinal or shear waves throughout the tissue. In this case, an oscillating magnetic field gradient is used to induce spin phase in proportion to the amplitude of the tissue motion (Muthupillai *et al* 1995). When implemented with a shear deformation at the tissue surface, to produce plane shear waves within the tissue, modulus is estimated from measurements of wavelength (Manduca *et al* 1996) or velocity (Bishop *et al* 1998). More recently, Sinkus *et al* (1999) and Weaver *et al* (1999) used a compressive deformation at the tissue surface, and measured the steady-state motion arising from mode conversion within the tissue. Alternatively, quasistatic elastography uses very low deformation frequencies of 0–1 Hz. In this case, wave propagation can be assumed to be negligible, with the tissue in an approximate state of static stress.

While both harmonic and quasistatic techniques represent valid approaches to MRE of the breast, we will limit our consideration in this paper to the use of quasistatic elastography. In this context, we will review two techniques for relative elastic modulus reconstruction, and assess their potential and limitations. We then present a novel technique that appears to be more efficient and robust. The latter is set up to improve specificity in breast lesions which have been previously detected by other means such as conventional contrast-enhanced breast MRI. The goal of this technique is to devise an efficient and convenient protocol to measure the relative elastic modulus of lesions which have been detected but not identified, and which could be appended to a conventional contrast-enhanced breast MRI procedure with minimal impact on the total procedure time.

3. Methods and materials

3.1. Tissue deformation measurement

Early MRI studies of motion were based on spin tagging (Zerhouni *et al* 1988) to elucidate strain rate studies of the myocardium. More recent studies have used phase contrast techniques

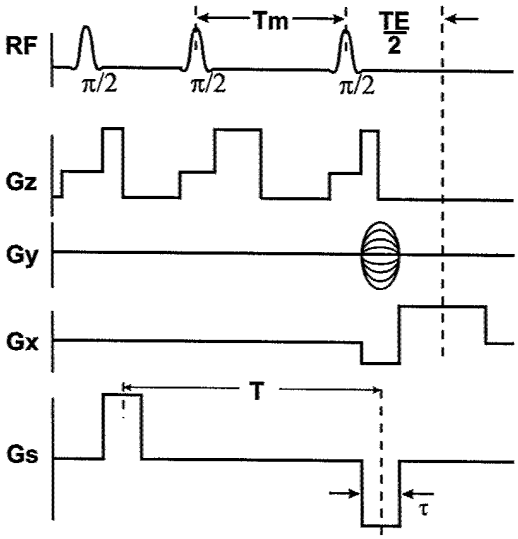

Figure 2. Stimulated echo pulse sequence used in MR elastography.

with pulsed gradients which are phase-locked to the applied mechanical deformation (Plewes *et al* 1995, Lewa and de Certaines 1995, Muthupillai *et al* 1995). The earliest methods for measuring tissue deformation with phase contrast imaging employed bipolar gradients to produce velocity-encoded images. Pelc *et al* (1991) used a cine phase-contrast method to obtain strain-rate images in the myocardium at multiple points throughout the cardiac cycle, and also demonstrated that the velocity data could be integrated in time to produce total displacement (Pelc *et al* 1995). Alternatively, the lobes of a bipolar motion encoding pulse can be separated in time to allow an interval for a finite displacement to occur and tissue come to rest again. This has been demonstrated in both spin-echo (Plewes *et al* 1995) or stimulated echo (STEAM) imaging sequences (Chenevert *et al* 1998). An advantage of the phase contrast methods is that they can be sensitive to very tiny motions with the appropriate choice of gradients. A recent study by Walker *et al* (1998) used such methods to detect motion with amplitudes of tens of nanometres arising from ultrasound fields.

A typical example of a STEAM pulse sequence for phase contrast MRE is shown in figure 2. The G_s gradient waveform provides displacement sensitivity. The two lobes of the G_s waveform are balanced, meaning that any nuclear spins which are stationary will receive zero net phase from it. Any other spins that displace will receive a phaseshift from G_s in the following manner. Assuming the material undergoes a step displacement of A units during the interval Tm:

$$r(t) = \begin{cases} 0, t < (\mathrm{TE} + \mathrm{Tm})/2 \\ A, t > (\mathrm{TE} + \mathrm{Tm})/2 \end{cases} \tag{1}$$

then the spin phase resulting from this sequence is:

$$\begin{aligned} \phi &= \gamma \int G_s(t) r(t)\, \mathrm{d}t \\ &= \gamma A G_0 \tau \end{aligned} \tag{2}$$

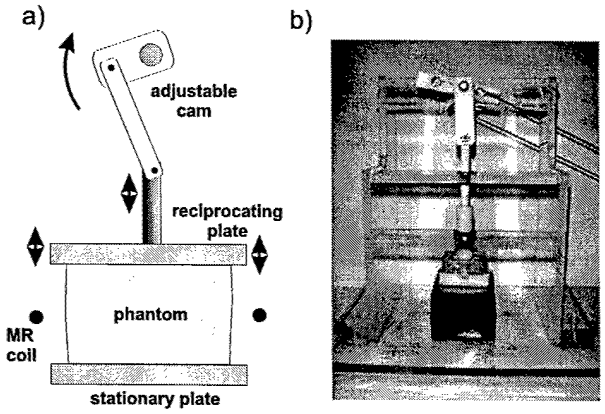

Figure 3. Schematic of the reciprocating compression device for phantom studies with quasistatic elastography (*a*). A camshaft with an adjustable moment arm is driven by an MR compatible ultrasonic motor positioned 12 in away and connected by a belt-drive. A photograph is shown in (*b*).

where γ is the gyromagnetic ratio of protons, G_0 is the amplitude of the displacement encoding gradient G_s and τ is the duration of each lobe of G_s. If there is non-zero velocity in the material when G_s is non-zero, that will be reflected as a source of error in ϕ. As long as $\tau \ll T$, phase errors from acceleration during the gradient pulses are assumed to be negligible. The orientation of the detected motion is determined by the orientation of the gradient G_s, which can be played on any axis. Each phase-encoded line of k-space is acquired twice, with the motion gradients reversed in polarity on the second acquisition. This compensates for phase errors due to B_0 inhomogeneity.

To illustrate the use of this technique, a gelatin/agar phantom composed of a cylinder of 1.25 cm in diameter in a 6 × 6 × 6 cm block was constructed. The Young's modulus of the gel was adjusted by varying the concentration of the agar (0.5 to 1.5%) during phantom preparation. In this case, the cylinder was prepared to have a Young's modulus of 31.5 kPa while that of the surrounding block was 11.5 kPa as determined by a uniaxial loading experiment on gel samples (Sciarretta *et al* 1999). This phantom was placed in a reciprocating compression device which is shown in figure 3. This system was designed to deliver quasistatic compression of 0–5 mm amplitude at the surface of the phantom, at a frequency of 1.0 Hz. At this low frequency, phase error due to velocity and acceleration can be minimized. The device was driven by an MR compatible ultrasonic motor (Shinsei USR-60-N4) (Tsuchiya 1988) which could be operated in the bore of the MR system without significant perturbation to the B_0 field homogeneity. The timing properties of the pulse sequence were TR/Tm/TE = 1000/250/15 (ms) and total scan time for a 128 × 128 matrix was 4:16. A magnitude image of this phantom is shown in figure 4(*a*), in which the inclusion can be seen with very subtle contrast. The phase image from the elastography experiment is shown in figure 4(*b*), encoded for left/right displacement (orthogonal to compression). Phase unwrapping and conversion of units according to equation (2) yields a displacement image (figure 4(*c*)). There is very little structure evident in the displacement image and it does not clearly resolve the circular inclusion. However, when the gradient of the displacement data is calculated to display the component of the strain tensor in the left/right direction, the circular inclusion is well resolved, as seen in figure 4(*d*). Note the areas of zero strain at the top and bottom surfaces of the phantom,

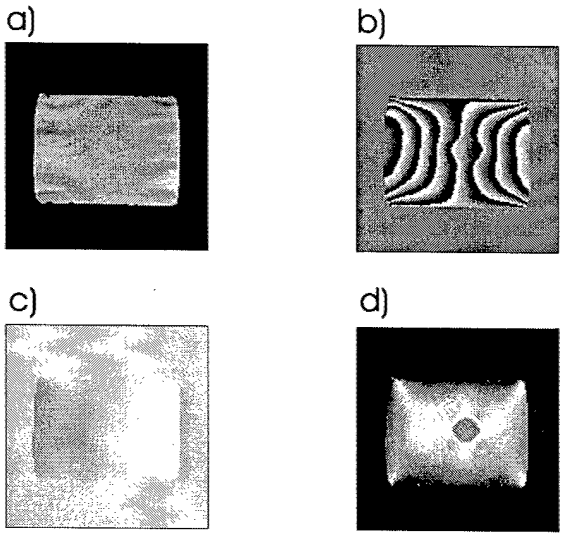

Figure 4. A magnitude image of an agarose/gel phantom with cylindrical inclusion (*a*). The inner circular region had a Young's modulus of 37.5 kPa with the outer material of 11.5 kPa. Compression was applied in the vertical direction using the apparatus of figure 3. STEAM sequence phase image (TR/T/TE = 1000/250/15 ms) with encoding in the horizontal direction (*b*). The displacement image after phase unwrapping (*c*) and the strain image in the horizontal direction (*d*).

which were not free to slide against the compressor plates, and compare with the right and left surfaces which were unconstrained. Points of very high strain appear at the corners of the phantom at the junction between these two types of boundary conditions. Aside from these minor artefacts, it is clear that strain images give a good rendering of the modulus distribution.

3.2. Finite element models for MRE simulations

One of the main components in iterative elastography algorithms is calculating the deformation and/or stresses resulting from known force or displacement boundary conditions. In complex geometries such as in biological tissues, this is done using numerical methods. We use the finite element method (FEM) (Bathe 1996) to calculate stresses in our novel reconstruction technique. To demonstrate the performance of this reconstruction technique, we present two examples. The first is a plane strain model of a block (figure 5(*a*)) which is composed of a hard circular lesion, a less rigid region representing fibroglandular tissue, inside a third soft rectangular region representing fat. The ratios of the modulus were 1:5:15 for the fat, fibroglandular and lesion regions respectively, and these ratios are indicated by the relative grey-scale intensity in figure 5(*a*). Because all MRE reconstructions described below are relative modulus reconstructions, specific values of Young's modulus are not assigned in these models. The Poisson's ratio of all materials was set to be 0.495.

To properly study a three-dimensional geometry, a realistic breast model was derived from MRI images of a healthy volunteer. The breast underwent gentle compression between two plates to conform the tissue into an approximately rectangular form, as seen in an axial image (figure 6(*a*)). Sixteen sagittal images through the breast volume were then obtained

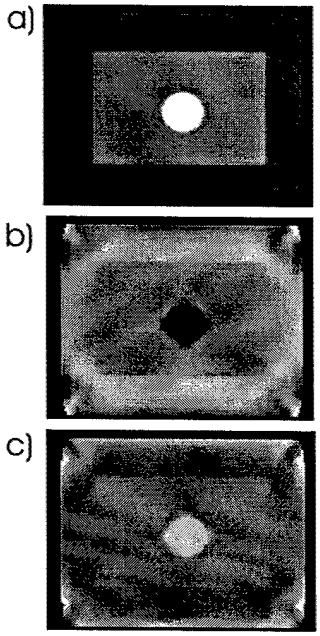

Figure 5. Numerical simulations of a two-dimensional three-component phantom composed of a hard circular inclusion in a rectangular region corresponding to fibroglandular tissue which is in turn embedded in a rectangular region of fat. The ratio of the lesion/fibroglandular/fat modulus was 15:5:1. The strain image corresponding to compression in the vertical direction (*b*). The reciprocal strain image (*c*) shows a qualitative agreement with the material modulus distribution of (*a*).

with a spin-echo pulse sequence. A typical image is shown in figure 6(*b*) where regions of fat (bright) and fibroglandular (dark) tissues are easily resolved with high SNR. The sagittal images were segmented on the basis of signal level to derive regions corresponding to adipose and fibroglandular structures throughout the breast (figure 6(*c*)) using an image analysis package (Mayo Foundation 1998). These segmented data were then used as a geometrical model to generate a mesh of the fibroglandular and fat components throughout the breast volume. As described elsewhere (Samani *et al* 1999), this mesh was generated using MAMMOGRID which was developed in our lab for breast finite element mesh generation. This code, which is fully automated, is voxel-based and uses eight-noded hexahedral elements to create 3D meshes from the segmented breast images. In order to conduct finite element calculations without excessive computational time and memory requirements, the resolution of the MRI data was reduced to produce a mesh of 16 841 elements and 15 939 nodes. The fibroglandular and fat layers were assumed to exhibit a homogeneous and isotropic behaviour throughout each material. The ratio of the modulus of the fibroglandular tissue to the modulus of fat which was assigned to these tissues was taken from data measured by Sarvazyan *et al* (1995) and set to be 5.0. The presence of a small tumour was simulated by altering the constitutive properties of appropriate elements in the 3D model. The meshed breast model is shown in figure 6(*d*) in relation to the breast plates used for compression. The problem of a breast compression between two plates is modelled as a 3D contact problem where the boundary conditions change continuously until equilibrium is reached.

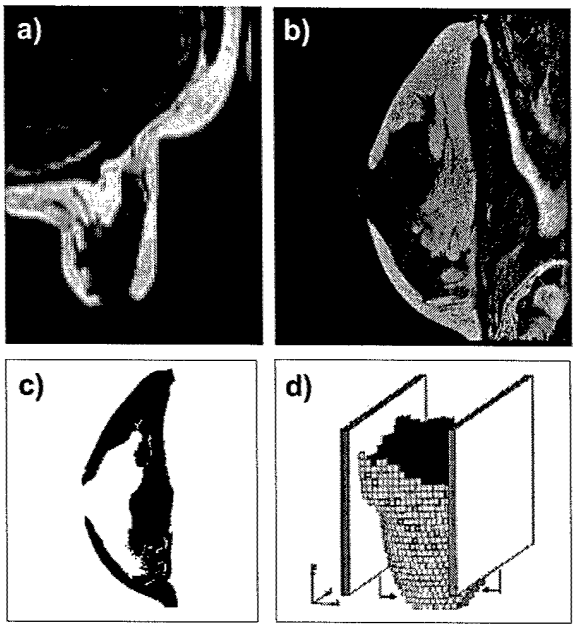

Figure 6. An axial image of the breast (*a*). A sagittal MRI image of the breast (*b*) taken from an array of images acquired under modest lateral compression. The images were acquired with a 2D spin-echo pulse sequence (TR/TE = 800/14 ms, three averages), and detected with the body coil for improved segmentation. Segmented image (*c*) of fat (black) and fibroglandular (white) tissues on the basis of signal brightness. The meshed 3D MRI data shown in conjunction with the compression plates used in image acquisition (*d*).

3.3. Strain imaging

Several investigators (Ponnekanti *et al* 1995, Kallel and Bertrand 1996, Skovoroda *et al* 1994) have pointed out that simple imaging of the strain data is useful as an approximate means to visualize the distribution of the tissue modulus. The relation between the Young's modulus E of a linear elastic, isotropic material, the stress and strain within the object is given by

$$\varepsilon = \frac{1+\nu}{E}\sigma - \frac{\nu}{E}\mathrm{tr}\,\sigma\mathbf{I} \tag{3}$$

where σ and ε and are the stress and strain tensors respectively and ν is the material Poisson's ratio, $\mathbf{I}$ is the identity matrix and tr is the trace operator. If we assume that the stress field is approximately constant over the local region of the lesion of concern, then the tissue modulus would be inversely related to strain measurement. This has been shown by Kallel and Bertrand (1996) for a very simple two-dimensional geometry of a circular inclusion of Young's modulus E_1 in a uniform and infinite medium of modulus E_2. The strain within the circular inclusion is independent of radius and is constant throughout the lesion, and furthermore the ratio of the strain in the direction of compression in the inclusion (ε_1) to the same component of strain in the medium far from the lesion (ε_2) is given by

$$\frac{\varepsilon_1}{\varepsilon_2} = \frac{1-2\nu}{\frac{E_1}{E_2}+(1-2\nu)} + \frac{2}{1+\frac{E_1}{E_2}(3-4\nu)}. \tag{4}$$

If we recognize that for most soft tissues Poisson's ratio is well approximated by 0.5, then this relation reduces to:

$$\frac{\varepsilon_2}{\varepsilon_1} = \frac{1}{2}\left(1 + \frac{E_1}{E_2}\right) \tag{5}$$

and shows that the reciprocal strain ratio is linearly related to the modulus ratio of the two materials. For large modulus variations the reciprocal strain ratio $\varepsilon_2/\varepsilon_1$ is 50% of E_1/E_2. For a small circular lesion in a relatively uniform background, we then expect that an image of the reciprocal strain ratio should be a first approximation of the relative modulus. To investigate whether this simple relation is a useful approximation for more complex geometries containing multiple regions of varying Young's modulus, we conducted studies with two- and three-dimensional finite element models described above.

3.4. Direct linear inversion with regularization

Strain images represent a good method of displaying the results of MR elastography, but in situations where more accurate quantitative measures of tissue elasticity are required, a calculation based on the governing partial differential equations of motion and known boundary conditions must be performed. This governing equation is known as the Navier equation, and is derived from Hooke's law, Newton's law and the continuum hypothesis (Chandrasekharaiah and Debnath 1994). In the following simplified form, it governs deformations in linear, isotropic elastic materials:

$$\nabla(\lambda\nabla\cdot\boldsymbol{u}) + \mu(\nabla^2\boldsymbol{u} + \nabla\nabla\cdot\boldsymbol{u}) + \nabla\mu(\nabla\boldsymbol{u} + \nabla\boldsymbol{u}^{\mathrm{T}}) = \gamma\frac{\partial\boldsymbol{u}}{\partial t} + \rho\frac{\partial^2\boldsymbol{u}}{\partial t^2} \tag{6}$$

where λ and μ are the Lame constants and $\boldsymbol{u}$ is the displacement vector field. On the right-hand side, γ and ρ are the material viscous damping constants and density respectively. In the case of quasistatic experiments, these derivatives vanish whereas harmonic elastography experiments require some knowledge of γ and ρ.

In a direct linear inversion of equation (6) for modulus, the equation is discretized with modulus as the unknown and may be solved with standard linear algorithms (Hansen 1998). This requires boundary conditions in terms of the unknown elastic modulus, but it is sufficient to assume a constant boundary modulus to achieve a relative modulus reconstruction. Skovoroda *et al* (1995) were the first to describe a direct linear inversion of equation (6), in a two-dimensional plane strain geometry. Most inversion methods published to date have assumed linear elasticity, small strain deformation and two-dimensional plane strain conditions. These assumptions limit the number of unknown variables and spatial locations such that the resulting matrix equation may be solved with a desktop workstation in a reasonable amount of time.

An inverse calculation usually requires high signal/noise to achieve a solution, which may be difficult to realize in experimental data. To study this issue, we have been exploring an alternative linear inversion to the method of Skovoroda *et al* (1995), in which the indeterminate term $\lambda\nabla\cdot\boldsymbol{u}$ in equation (6) is retained as an additional unknown. This second unknown is interpreted as an 'average' stress, or pressure (p). Accordingly, equation (6) becomes:

$$\nabla p + \mu(\nabla^2\boldsymbol{u} + \nabla\nabla\cdot\boldsymbol{u}) + \nabla\mu(\nabla\boldsymbol{u} + \nabla\boldsymbol{u}^{\mathrm{T}}) = 0. \tag{7}$$

The resulting matrix equation to solve is four times as large, but it avoids taking the third spatial derivative of displacement data. This has been shown to improve the matrix conditioning and relaxes the need for high displacement signal/noise data to obtain an inverse solution (Bishop *et al* 1999). The matrix equation is solved by generalized singular value decomposition combined with Tikhonov regularization (Hansen *et al* 1998).

A two-dimensional plane strain geometry was chosen to test this method. The object is composed of a hard inclusion in a soft uniform background of relative modulus of 3:1. Simulated displacement data were generated, and combined with normally distributed random values such that the maximum surface displacement to noise ratio varied between 500 and 10 000. The normal distribution is an adequate noise model in MR phase images assuming the signal/noise ratio in the magnitude is greater than 2 (Conturo and Smith 1990). These noisy displacement data were used as input data to the linear inversion.

3.5. Iterated inversion with geometric constraint

A clinically practical method of elastography for breast applications would be designed so that it could be added to the end of a standard contrast-enhanced MR breast procedure without significant additional imaging time. As such, the data acquisition should be limited to relatively few slices surrounding the lesion of interest. Further, as each strain component requires a separate acquisition with the gradients oriented in the direction of interest, it would be worthwhile to limit the number of strain components to minimize imaging time.

To achieve these goals, we consider the direct application of *a priori* knowledge to the elastography problem. First, we assume that we have some knowledge of the biomechanical properties of the fat and fibroglandular tissues which would surround an unknown lesion. In principal, these could be estimated from population averages of *ex vivo* experiments. In addition, we assume that the location and geometry of the suspicious finding is known from the contrast-enhanced MRI scan. Finally, as our goal is only to consider the modulus of the lesion as a whole, we may treat the lesion modulus as a constant value.

To illustrate this concept, we again consider the problem of estimating the modulus of a stiff circular inclusion in a uniform background of lower modulus as shown in figure 7. An iterative process is used whereby a current estimate of modulus distribution is used to calculate the stress distribution under the specified boundary conditions (Bishop and Plewes 1998). This stress field, combined with the experimentally measured strain ε_{yy}, is then used to update the modulus distribution in the inclusion using:

$$E = \frac{1}{\varepsilon_{xx}}(\sigma_{xx} - \nu\sigma_{yy} - \nu\sigma_{zz}) \tag{8}$$

which is derived from equation (3). The updated modulus of the inclusion, which is assumed to be constant over the inclusion and is calculated by averaging the values obtained from equation (8), is then used in a subsequent stress calculation. To start the calculation we begin with a modulus distribution as an initial guess which can be simply obtained by ignoring the inclusion. Based on this modulus distribution, the stress terms of equation (8) are calculated from a finite element analysis of the segmented tissue components obtained from previous MR images. The modulus for each pixel within the inclusion is calculated by a simple division by the corresponding measured strain to produce the inclusion's updated modulus using equation (8). Subsequent stress calculation based on the new modulus distribution and modulus updating is continued until convergence is achieved. Unlike other iterative inversion techniques which require inverting relatively large systems of simultaneous equations (Skovoroda *et al* 1995, Weaver *et al* 1999), this technique is computationally straightforward, and is less sensitive to noise because the presence of noise affects each element locally and does not propagate throughout the entire object. Furthermore, as this technique requires the measurement of only one strain component, it requires only a single MR acquisition in a single plane through the object.

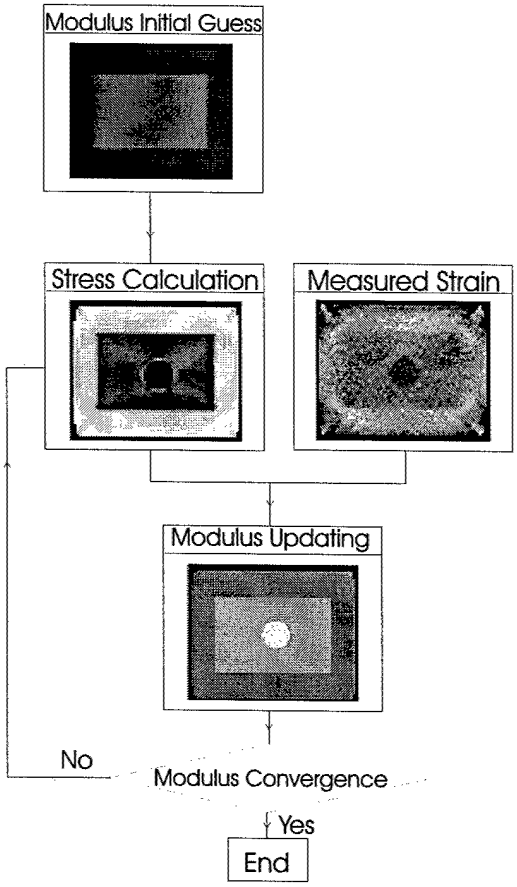

Figure 7. Flow chart of the iterative method for reconstructing elastic modulus.

3.6. In vivo strain imaging

In order to test whether the above concepts are suitable for clinical breast imaging we constructed a device for *in vivo* quasistatic elastography, which attaches to a commercially available phased-array breast coil (MRI Devices Inc., Milwaukee WI). In this application, the breast undergoes gentle pre-compression between two parallel plates (figure 8(*a*)). The lateral plate is driven sinusoidally by two pairs of counter-rotating cams connected by a shaft to an ultrasonic motor. The amplitude of the reciprocating motion is 2.5 mm, at a frequency of 1 Hz. Given that the typical breast thickness in this geometry is approximately 7 cm, this amounts to a maximum strain of 3.5%. A photograph of the actuator is shown in figure 8(*b*).

The compression device was tested with a volunteer to determine the quality of the displacement and strain data which could be expected in clinical application. Imaging was performed with the STEAM sequence over a 14 × 7 cm field of view, with in-plane resolution of 1 mm^2, 1 cm slice thickness and scan time of 2:08. The mixing time (T_m) was 150 ms and

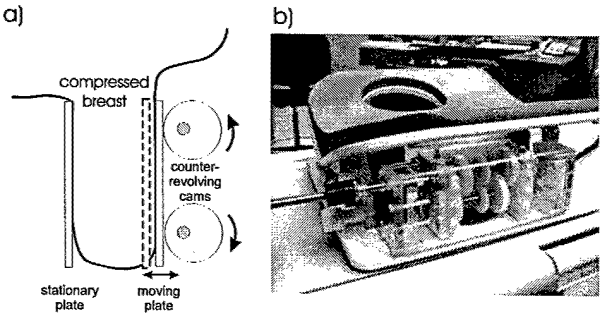

Figure 8. Schematic of a reciprocating compression device for quasistatic elastography with a commercial phased-array breast coil (*a*) and a photograph of the device (*b*). The moving plate is connected by the driveshaft seen at left to an ultrasonic motor at 12 inches distance.

the displacement encoding gradient pulses (figure 2) were adjusted to generate 10π radians of phase accumulation at the point of maximum displacement.

4. Results

4.1. Strain imaging

Using a nonlinear finite element package (Hibbit, Karlsson and Sorensen, Inc. 1998) a deformation corresponding to 5% strain in the vertical (y) direction was computed. In figure 5(*b*) we show the strain component ε_{yy}, while in figure 5(*c*) we show an image proportional to the reciprocal of this strain component $(1/\varepsilon_{yy})$ as suggested by equations (2) and (4). This image qualitatively reflects the modulus distribution. In order to estimate the accuracy of using the reciprocal strain data as a measure of modulus, we calculate the ratio R_{yy}, defined as the average reciprocal strain in the lesion relative to the average reciprocal strain in an area surrounding the lesion of identical area, given by:

$$R_{yy} = \frac{\langle 1/\varepsilon_{yy}\rangle_1}{\langle 1/\varepsilon_{yy}\rangle_2} \tag{9}$$

where the subscript 1 refers to the ensemble average over the area of the lesion and 2 refers to the ensemble average of an annulus surrounding the lesion in the fibroglandular tissue (region 2) with the area of the annulus equal to that of the lesion. R_{yy} is plotted versus the relative modulus of the lesion E_1 to fibroglandular modulus E_2 in figure 9. The relationship between the true modulus ratio and the reciprocal strain ratio is nearly linear, and the slope of the curve is approximately 0.5 as predicted from the two-component model of equation (5). Local variations in strain within four radii of the inclusion that affect this calculation (Kallel *et al* 1996) are effectively averaged out to zero by the annular ROI. However, this simulation is for a two-dimensional geometry which is still relatively simple compared with the three-dimensional geometry expected in measurements of the breast.

The three-dimensional breast model was then used to study the behaviour of equation (9). A 0.5 cm cancer, five times stiffer than the fibroglandular tissue, was added to the model as shown in a sagittal section of the mesh (figure 10(*a*)), and a static compressional strain of 10% was simulated according to the geometry shown in 6(*d*). The stress distribution (figure 10(*b*)) shows relatively little structure, while the strain distribution (figure 10(*c*)) allows a subtle rendering of the fat, fibroglandular and tumour components. Measures of the relative

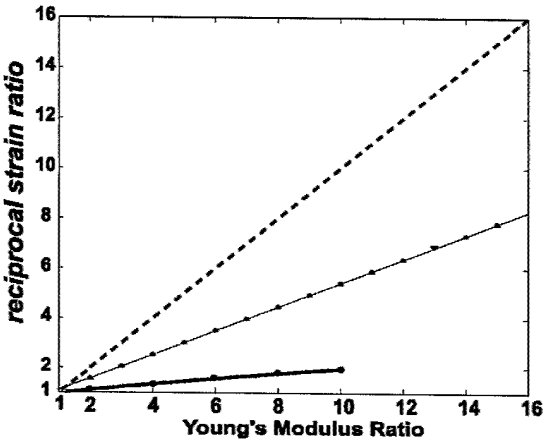

Figure 9. The reciprocal strain ratio in the lesion/fibroglandular tissue versus relative lesion/fibroglandular modulus from the geometry of figure 5 (thin full line). The same calculation for the three-dimensional lesion in the breast model of figure 6 (thick full line). The line of identity is shown (dashes).

reciprocal strain between the tumour and the surrounding material (as defined by equation (9)) were calculated for various modulus ratios of the tumour to the surrounding fibroglandular tissue, and plotted in figure 9. These data show that the reciprocal strain ratio is approximately linear with the true modulus ratio as was seen in the two-dimensional plane strain model, but the slope of the relation is significantly lower due to the three-dimensional geometry and the heterogenous distribution of tissue regions. These simulations support previous findings that strain imaging provides a straightforward means to image the distribution of modulus; however, the unavoidable variation in the stress field which must occur in complex geometries makes these metrics of modulus quantitatively unreliable.

4.2. Direct linear inversion with regularization

Results obtained for direct linear inversion are illustrated in figure 11. Constant and arbitrary elastic modulus and pressure boundary conditions are assumed, so reconstructed values are relative. The unregularized modulus solution (column 1) clearly shows the sensitivity of this inverse problem to noise. The SNR $=$ 10 000 dataset depicts a virtually noise-free result. As the displacement SNR of the data drops below 1000, the unregularized solution begins to diverge. The effect of Tikhonov regularization to improve the reconstruction is seen in column 2. For a displacement SNR of about 1000, most of the reconstruction artefact is removed, although the depiction of the inclusion is also mildly attenuated. The regularized pressure reconstruction (column 3) shows the distribution of average stress throughout the object.

4.3. Iterated inversion with geometric constraint

In the following simulated iterative reconstructions, the convergence criterion was set to be $|(E_{i+1} - E_i)/E_i| < tol$. Here E_{i+1} and E_i are the Young's moduli in the last two iterations and tol is a small number which was selected to be 0.04. The results of the iterative calculation are

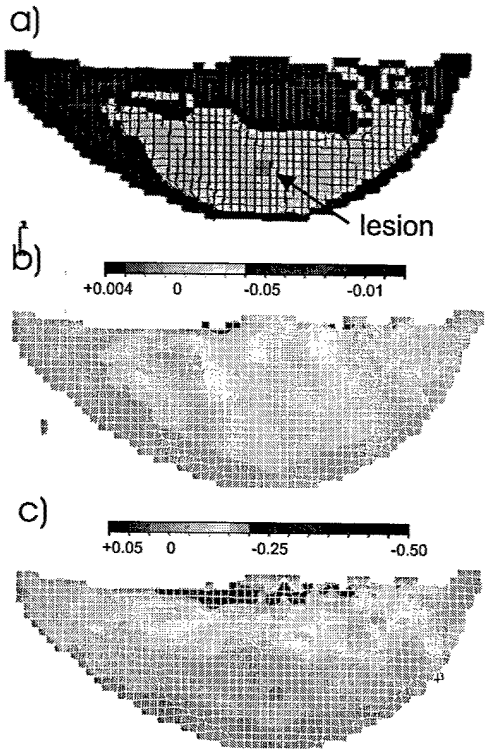

Figure 10. Segmented fat (black) fibroglandular (orange) tissues (*a*) with a simulated tumour five times stiffer than the fibroglandular tissue inserted in the breast (red). The stress distribution in the compression direction (*b*) and the strain component in the direction of the compression (*c*).

shown in figure 12 where we estimate the the modulus distribution of the lesion of figure 5, relative to the surrounding fibroglandular and fat regions for which modulus values are assumed to be known. The strain data were calculated in the presence of noise added to the displacement data corresponding to a maximum displacement signal/noise of 1000, 300 and 100. After five iterations the modulus distribution converges to stable results for the displacement signal/noise of 1000 and 300 while simulation with an SNR = 100 did not converge. These data suggest that for the lesion in this particular model, the signal/noise requirements are substantially reduced over that seen from the full inversion of figure 11 where a minimum SNR of at least 1000 is required.

To test this concept in a more realistic application, we once again use our three-dimensional model of the breast with a simulated lesion (figure 8). As before, we assumed that the location of the nodule was known on the basis of previous MRI data and that the relative modulus of the fat and fibroglandular components are also known. It is further assumed that only one component of strain data (parallel to the direction of compression of the breast) is measured experimentally. In addition, the boundary conditions of the three-dimensional object are assigned from the previous MRI data and the chest wall is assumed to be fixed. Noise was added to the displacement data to simulate signal/noise ratios of 1000, 300 and 100. As a first approximation, we calculate the reciprocal strain data which are shown in figures 13(*a*)–(*c*).

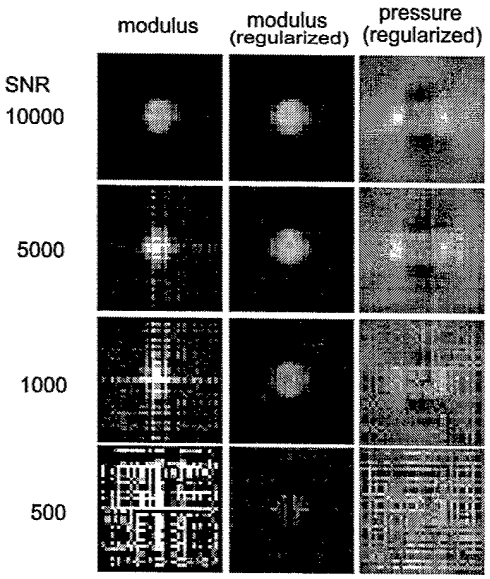

Figure 11. Relative modulus and pressure reconstruction for a round inclusion object. Inverse solutions of object modulus and pressure are shown for various SNR levels in the raw (unfiltered) input displacement data. The left column of images shows the modulus reconstructed with direct LU matrix decomposition. With regularization, considerable noise reduction is achieved (middle column). The pressure reconstruction is shown in the right column.

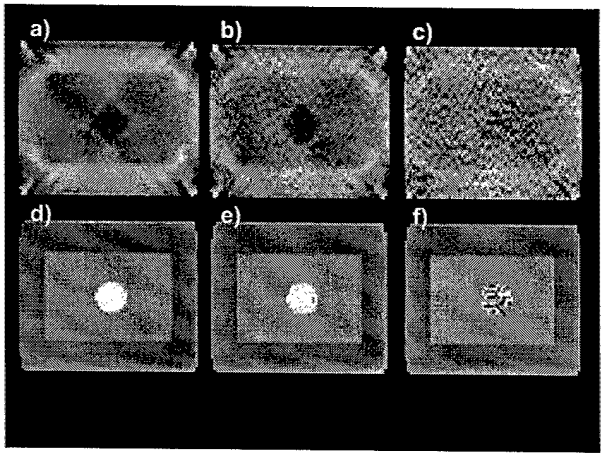

Figure 12. Strain distribution (*a*), (*b*), (*c*) for the geometry of figure 5 and the modulus distribution (*d*), (*e*), (*f*) after five iterations using *a priori* information for a signal/noise of 1000, 300 and 100 respectively. The average modulus value converged to a factor of 2.96, 3.7 and 1.02 times harder than the fibroglandular for the said signal/noise ratios respectively. The true modulus ratio was 3.

The resulting modulus ratio of the lesion to the background are 37%, 47% and 420% of the true values of the lesion/background ratio for the displacement SNR values of 1000, 300

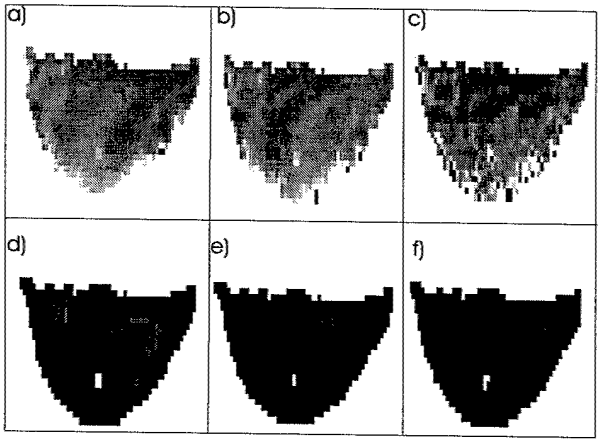

Figure 13. Strain distribution (*a*), (*b*), (*c*) for the breast of figure 10 and the modulus distribution (*d*), (*e*), (*f*) after six iterations using *a priori* information for a signal/noise of 1000, 300 and 100 respectively. The average modulus value converged to a factor of 5.75, 8.8 and 8.4 times harder than the fibroglandular for the said signal/noise ratios respectively. The true modulus ratio was 5.

and 100 respectively. These ratios were used to start the iterative procedure, and after six iterations, the modulus distribution converges to the final results shown in figures 13(*d*)–(*f*). Figure 13(*d*) shows that corresponding to signal/noise ratio of 1000, the modulus of the lesion converges to within 15% of the true value. It is important to note that this calculation is based on three-dimensional finite-element simulations of the breast to estimate the stress tensor throughout the breast for the iterative procedure. This simulation suggests that a signal/noise in the displacement data of approximately 1000 is adequate to conduct this localized inversion technique.

4.4. In vivo strain imaging

Results for *in vivo* strain imaging are shown in figure 14. In the magnitude image (figure 14(*a*)), the signal/noise ratio was 10 and 16 for fibroglandular and fat regions respectively. After the raw phase data have been unwrapped and converted to units of displacement (figures 14(*b*)–(*c*)), the displacement/noise ratio at the point of maximum displacement is in the range 300–500. The strain image (figure 14(*d*)) appears to show a relatively uniform strain throughout, except towards the bottom part of the image where the tissue was not in contact with the medial (left) compression plate. Numerical differentiation tends to sharply reduce signal/noise, and thus the strain/noise ratio is about 5. While no hard masses were likely in a healthy volunteer, it was expected that subtle strain variations arising from fat and fibroglandular components would be seen. However, the low strain/noise ratio and 1 cm slice thickness precluded visualization of separate fat and fibroglandular regions. Nevertheless, this experiment indicates that it should be feasible to obtain displacement/noise ratio of 1000 *in vivo* through further optimization of pulse sequence timing, resolution and bandwidth parameters, along with improvements in the geometry of the phased array to fit the breast more closely. As suggested by the simulations described above, a displacement SNR of 1000 should be sufficient for inverse reconstructions of elastic modulus *in vivo*.

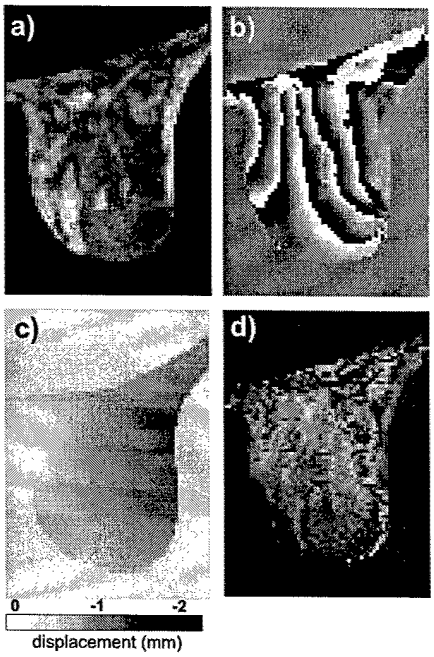

Figure 14. Breast magnitude image (*a*) from a normal volunteer acquired with the apparatus of figure 8. The lateral compressor plate is at the right, and the fixed medial plate at the left. The phase image (*b*) shows motion encoded in the direction of compression (left/right). The displacement image (*c*) shows some minor phase unwrapping artefacts, but these artefacts drop out of the strain image (*d*), which shows a relatively homogeneous strain in the upper part of the tissue volume.

5. Discussion

MR elastography is a new and promising approach for the diagnosis of breast cancer. The use of phase-contrast MR imaging can provide extremely high sensitivity to small motions and allows measurement of the entire strain tensor throughout the breast. However, accurate reconstruction of the distribution of modulus throughout the breast requires some form of inverse solution. While a number of previous efforts have been reported, the ill-conditioning of the governing equation makes robust inverse solutions challenging in the presence of experimental noise. At the heart of this problem is the implicit objective to reconstruct the spatial distribution of modulus throughout the image as would be needed for a detection task. This approach is the direction that many investigators have taken and continue to pursue. In this paper, we outline a different objective which aims not to detect lesions, but only to measure the biomechanical properties of previously identified regions within a breast MR image. As the sensitivity of contrast enhanced breast MRI to small breast cancers has been shown to be in excess of 90%, we believe that the main role of breast elastography will be to aid in lesion diagnosis. It is with this objective that we have investigated the application of *a priori* information about lesion size and location. We have shown that with assumptions about the breast configuration, robust estimates of lesion modulus are possible based on displacement signal/noise which appears feasible to obtain *in vivo*.

Furthermore, the proposed method has a significant advantage in that only one displacement component, in only one slice, is needed to reconstruct the modulus of a lesion in

three dimensions. As the images shown in figure 14 required only 2.1 min of signal acquisition time, this procedure could easily be appended to the end of a standard contrast-enhanced MR scanning procedure. In contrast, modulus reconstruction by direct inversion would require a minimum of three displacement measurements obtained over each separate slice location throughout the object in order to establish a three-dimensional boundary value problem. At 2.1 min per acquisition, a direct 3D inversion represents 6.3 min of scan time per slice, and total scan time therefore would be considerably higher than the iterative method described above.

A number of issues regarding the reliability of this technique need further study. The accuracy of solutions will depend on the degree to which the boundary conditions match the clinical experiments. The geometry of the breast relative to the elastography apparatus will be evident from the 3D contrast-enhanced MR images which are anticipated to precede any elastography study, and may be used to generate the finite element meshes. However, the nature of the constraint along the chest wall will need to be assigned with care as it represents an important boundary condition. Assumptions regarding the biomechanical properties of fat and fibroglandular tissue will also influence the accuracy of the final result. While properties of these normal tissues could be taken from population averages of *ex vivo* experiments, patient to patient variation would be expected to influence the accuracy of the result. A potential solution to this problem is to let the modulus values of fat, fibroglandular and the lesion be unknowns in our iterative approach while making the assumption that they are constant and isotropic over each tissue. Finally, the assumption that fat and fibroglandular tissue have constant modulus remains to be demonstrated within a patient. These issues, along with further technical improvements and clinical assessment of this technique, will be the subject of future research.

Acknowledgments

The authors gratefully acknowledge the support of the Terry Fox Foundation (programme project grant 006886) and the US Army (DAMD 17-99-1-9391).

References

Anderson W 1955 *Pathology* (St Louis: Mosby)

Baker M 1982 Breast cancer detection demonstration project: five-year summary report *CA Cancer J. Clin.* 32–194

Bassett L and Kimme-Smith C 1989 Breast sonography: technique, equipment and normal anatomy *Semin. Ultrasound, CT, MR* **88** 589

Bathe K 1996 *Finite Element Procedures* (Englewood Cliffs, NJ: Prentice Hall)

Bishop J, Leitch M, Poole G and Plewes D 1998 Magnetic resonance imaging of shear wave propagation in excised tissue *J. Magn. Reson. Imaging* **8** 1257–65

Bishop J and Plewes D 1998 An alternate method for calculating elastic properties of breast tissue *Proc. ISMRM 6th Meeting (Sydney)* p 2102

Bishop J, Samani A and Plewes D 1999 Pressure/modulus inversion for MR elastography *Proc. ISMRM 7th Meeting (Philadelphia, PA)* p 2063

Bjurstam N and Bjorneld L 1994 Mammographic screening in women aged 40–49 years at entry: results of the randomized controlled trial in Gothenberg, Sweden *American College of Radiology 26th National Conf. on Breast Cancer (Palm Desert, CA)* pp 62–3

Bombardien E, Frippa F, Maffioli L and Greco M 1997 Nuclear medicine technique for the study of breast cancer *Eur. J. Nucl. Med.* **24** 809–24

Chandrasekharaiah D and Debnath L 1994 *Continuum Mechanics* (New York: Academic)

Chenevert T, Skovoroda A, O'Donnell M and Emelianov S 1998 Elasticity reconstructive imaging by means of stimulated echo MRI *Magn. Reson. Med.* **39** 482–90

Conturo T and Smith G 1990 Signal-to-noise in phase angle reconstruction: dynamic range extension using phase reference offsets *Magn. Reson. Med.* **15** 420–37

Daniel B, Yen Y and Glover G *et al* 1998 Breast disease: dynamic spiral MR imaging *Radiology* **209** 499–509

European Society for Mastology Breast Cancer Screening Evaluation Committee 1993 *Technical Report* 2

Ford D, Easton D, Bishop D, Narod S and Goldgar D 1994 Risks of cancer in BRCA-mutation carriers *Lancet* **343** 692–3

Fung Y 1993 *Biomechanics: Mechanical Properties of Living Tissue* 2nd edn (Berlin: Springer)

Hansen P 1998 *Rank-deficient and Discrete Ill-posed Problems* (Philadelphia, PA: SIAM)

Hibbit, Karlsson and Sorensen, Inc. 1998 *ABAQUS V5.8.1, User's Manual*

Hill D, White V, Jolley D and Mapperson K 1988 Self examination of the breast: is it beneficial? Meta-analysis of studies investigating breast self examination and the extent of breast disease in patient with breast cancer *Br. Med. J.* **297** 271–5

Kallel F and Bertrand M 1996 Tissue elasticity reconstruction using linear perturbation method *IEEE Trans. Med. Imaging* **15** 299–313

Kallel F, Bertrand M and Ophir J 1996 Fundamental limitations on the contrast-transfer efficiency in elastography: an analytic study *Ultrasound Med. Biol.* **22** 463–70

Khalkhali I, Cutrone J and Mena I 1995 Scintimammography: the complementary role of Tc-99m Sestamibi prone breast imaging for the diagnosis of breast carcinoma *Radiology* **196** 421–6

Kuhl C, Schmutzler R, Ceutner C, Morakkabati N, Kempe A and Schild H 1999 Breast MR screening in women with familial breast cancer (carriers of breast cancer susceptibility genes): preliminary results of the first and second screening round *Radiology* **213** (p) 455

Leach M 1998 Assessing contrast-enhanced MRI as a method of screening women at genetic risk of breast cancer: study design, methodolgy and analysis *Proc. ISMRM 6th Meeting (Sydney)* p 226

Lewa C and de Certaines J 1995 MR imaging of viscoelastic properties *J. Magn. Reson. Imaging* **5** 242–4

Manduca A, Muthupillai R, Rossman P, Greenlead J and Ehman R 1996 Image processing for magnetic resonance elastography *Proc. SPIE* **2710** 616–23

Mathieson T and Flensburg H 1992 Breast cancer mortality reduction in three current randomized breast cancer screening trials *Breast Dis.* **5** 91

Mayo Foundation 1998 *AnalyzeAVW V2.5*

Muthupillai R, Lomas D, Rossman P, Greenleaf J, Manduca A and Ehman R 1995 Magnetic resonance elastography by direct visualization of propagating acoustic strain waves *Science* **269** 1854–7

Newcomb P, Weiss S, Storer B, Scholes D and Young B 1991 Breast self examination in relation to the occurrence of advanced breast cancer *J. Natl. Cancer Inst.* **83** 260–5

Nunes L *et al* 1997 Breast MR imaging: interpretation model *Radiology* **202** 833–41

Orel S, Schnall M, LiVolsi V and Troupin R 1994 Suspicious breast lesions: MR imaging with radio-pathologic correlation *Radiology* **190** 485–93

Pelc N, Drangova M and Pelc L 1995 Tracking of cyclic motion with phase-contrast cine MR velocity data *J. Magn. Reson. Imaging* **5** 339–45

Pelc N, Herfkens R, Shimakawa A and Enzmann D 1991 Phase contrast cine magnetic resonance imaging *Magn. Reson. Q.* **7** 229–54

Pietrzyk U, Scheidhauer K and Scharl A 1995 Presurgical visualization of primary breast carcinoma with pet emission and transmission imaging *J. Nucl. Med.* **35** 1882–4

Plewes D, Betty I, Urchuk S and Soutar I 1995 Visualizing tissue compliance with MR imaging *J. Magn. Reson. Imaging* **5** 733–8

Ponnekanti H, Ophir J, Huang Y and Cespedes I 1995 Fundamental mechanical limitation on the visualization of elasticity contrast in elastography *Ultrasound Med. Biol.* **21** 533–43

Samani A, Bishop J, Ramsay E and Plewes D 1999 A 3-D contact problem finite element model for breast shape deformation derived from MRI data *Proc. ASB, 23rd Ann. Meeting (Pittsburg, PA)* (American Society of Biomechanics) p 72

Sarvazyan A *et al* 1994 Elasticity imaging as a new modality of medical imaging for cancer detection *Proc. Int. Workshop on Interaction of Ultrasound with Biological Media (Valenciennes, France)* pp 69–81

——1995 Biophysical bases of elasticity imaging *Acoust. Imag.* **21** 223–40

Sciarretta J, Bishop J, Samani A and Plewes D 1999 MR validation of soft tissue deformation as modeled by non linear finite element analysis *Proc. ISMRM, 7th Meeting (Philadelphia, PA)* (Berkeley, CA: ISMRM) p 246

Sinkus R, Lorenzen J, Schrader D, Lorenzen M, Dargatz M and Holz D 1999 MR-Elastography applied to *in vivo* MR-mammography *Proc. ISMRM, 7th Meeting (Philadelphia, PA)* (Berkeley, CA: ISMRM) p 259

Skovoroda A, Emelianov S, Lubinski M, Sarvazyan A and O'Donnell M 1994 Theoretical analysis and verification of ultrasound displacement and strain imaging *IEEE Trans. Ultrason. Ferroelectr. Freq. Control* **41** 302–13

Skovoroda A, Emelianov S and O'Donnell M 1995 Tissue elasticity reconstruction based on ultrasonic displacement and strain images *IEEE Trans. Ultrason. Ferroelectr. Freq. Control* **42** 747–65

Sohn L, Fox K, August D, Dershaw D, Rebbeck T, Webser B and Lichter A 1997 *Principles and Practice of Gynecologic Oncology* (Philadelphia, PA: Lipponcott) pp 1088–105

Stoutjesdijk M, Boetes C, Van Die L, Beex L, Bult P and Barentsz J 1999 Magnetic resonance mammography for breast cancer screening of patients from high-risk populations: results of a prospective pilot study *Radiology* **213** (p) 454

Tsuchiya K 1988 A new concept in motors: ultrasonic wave oscillation drive energy *Japan. Electron. Eng.* July, 42–4

Walker C, Foster F and Plewes D 1998 Magnetic resonance imaging of ultrasonic fields *Ultrasound Med. Biol.* **24** 137–42

Weaver J, van Houten E, Miga M, Kennedy F, Hartov A, Poplack S, Nagy H and Paulsen K 1999 Measurement of harmonic motion for MR elastography *Proc. ISMRM, 7th Meeting (Philadelphia, PA)* (Berkeley, CA: ISMRM) p 1617

Weinreb G and Newstead G 1995 MR imaging of the breast *Radiology* **196** 593–610

Zerhouni E *et al* 1988 Human heart: tagging with MR imaging—a method for non-invasive assessment of myocardial motion *Radiology* **109** 59–63

Phys. Med. Biol. **45** (2000) 2081–2091. Printed in the UK PII: S0031-9155(00)10692-X

Two-dimensional MR elastography with linear inversion reconstruction: methodology and noise analysis

Jonathan Bishop, Abbas Samani, Justin Sciarretta and Donald B Plewes†

Department of Medical Biophysics, University of Toronto, 2075 Bayview Avenue, North York, Ontario, M4N 3M5, Canada

E-mail: dbp@srcl.sunnybrook.utoronto.ca

Received 5 January 2000, in final form 13 March 2000

Abstract. A methodology for imposing approximate plane strain conditions in magnetic resonance elastography through physical constraint is described. Under plane strain conditions, data acquisition and analysis may be conducted in two dimensions, which reduces imaging and reconstruction time significantly compared with three-dimensional analysis. Simulations and experiments are performed to illustrate the constraint concept. A signal/noise analysis of a two-dimensional linear inversion technique for relative elastic modulus is undertaken, and modifications to the numerical method are described which can reduce the SNR requirements by a factor of two to four. Experimentally measured data are reconstructed to illustrate the performance of the method.

1. Introduction

Contrast based on tissue elastic properties has significant potential for imaging breast cancer and other disease (Sarvazyan *et al* 1994). Since MR imaging is not directly sensitive to elastic modulus, such properties must be calculated from measurements of displacement. Displacement within an object is generated by either quasistatic or oscillatory stresses applied mechanically at the object surface, or remotely by other means such as ultrasound (Andreev *et al* 1997). In MRI, displacement is reliably measured with phase contrast methods (Pelc *et al* 1991). Thus the procedure of MR elastography (MRE) is composed of two distinct phases: acquisition of the displacement vector field through combined MRI and applied stress, followed by a data processing stage in which elastic modulus values and other variables may be calculated from raw displacement data (Ophir *et al* 1997).

Strain images represent a good method of displaying the results of MR elastography. They require only moderate SNR and can be computed promptly. For simple geometries such as focal masses, strain is related linearly to elastic modulus (Plewes *et al* 2000), and may suffice as a reconstruction method. In situations where more accurate modulus depiction is required, a calculation of the modulus based on governing partial differential equations and known boundary conditions may be performed. This calculation is ill-conditioned, and thus SNR requirements are high and the computation time is significant. Nevertheless, a number of investigators have pursued this approach with their displacement data (Skovoroda *et al* 1995,

† Author to whom correspondence should be addressed at: Department of Medical Biophysics, Imaging/Bioengineering Research Group, Sunnybrook and Women's College Healths Sciences Centre, 2075 Bayview Avenue Toronto, Ontario Canada M4N 3M5.

0031-9155/00/082081+11$30.00

Chenevert *et al* 1998, Kallel and Bertrand 1996, Manduca *et al* 1996, Dutt *et al* 1997, Sinkus *et al* 1999, Weaver *et al* 1999).

In this paper, we review previous inverse methods employed in MRE, and then focus on the linear inversion approach with a signal/noise analysis, and modifications for improved noise performance. We also describe a strategy for MR elastography that applies physical constraints to create an approximate state of plane strain in the object. Under plane strain, it is possible to perform accurate modulus reconstruction on two-dimensional strain data; this represents large potential savings in data acquisition and reconstruction time compared with the alternative of making three-dimensional strain measurements.

1.1. Inverse methods for elastography

The Navier vector equation is derived from Hooke's law, Newton's law and the continuum hypothesis (Chandrasekharaiah and Debnath 1994). In the following simplified form, it governs deformations in linear, isotropic elastic materials:

$$\nabla(\lambda\nabla\cdot\boldsymbol{u})+\mu(\nabla^2\boldsymbol{u}+\nabla\nabla\cdot\boldsymbol{u})+(\nabla\mu)(\nabla\boldsymbol{u}+\nabla\boldsymbol{u}^T)=\gamma\frac{\partial\boldsymbol{u}}{\partial t}+\rho\frac{\partial\boldsymbol{u}}{\partial t^2} \qquad (1)$$

where λ is a Lamé constant, μ the shear modulus and $\boldsymbol{u}$ is the displacement vector field. On the right-hand side, γ and ρ are the material parameters of viscous damping and density respectively. Depending on whether or not the data are acquired under dynamic loading conditions, the right-hand side may be omitted. In MRE, the shear modulus μ is the primary unknown of interest. Although the Lamé constant λ is also unknown, it can be eliminated by several means as described below.

There are two basic approaches to solving (1) numerically for modulus μ. If the equation is discretized directly with modulus as the unknown, it may be solved with standard linear algorithms (Hansen *et al* 1998). This requires boundary conditions in terms of the unknown elastic modulus, although it may be sufficient to assume a constant boundary modulus to achieve a relative modulus reconstruction. Alternatively, (1) may be solved in the usual forward sense with displacement as the unknown, based on a current estimate of modulus. The modulus estimate is updated through some nonlinear algorithm and the process repeated iteratively until the calculated displacement converges to experimentally measured displacement (Kallel and Bertrand 1996, Bishop and Plewes 1998). In this approach, exact displacement boundary conditions are available from the experimental data. In either case, most inversion methods published to date (Skovoroda *et al* 1995, Chenevert *et al* 1998, Kallel and Bertrand 1996, Manduca *et al* 1996, Dutt *et al* 1997, Weaver *et al* 1999) have assumed linear elasticity, small-strain deformation and two-dimensional plane strain conditions. These assumptions limit the number of unknown variables and spatial locations such that the resulting matrix equation may be solved with a desktop workstation in a reasonable amount of time.

Skovoroda *et al* (1995) were the first to describe inverse calculations of elastography data, using a direct linear inversion of (1). Assuming tissue incompressibility, $\lambda\nabla\cdot\boldsymbol{u}$ is indeterminate and was therefore eliminated analytically by taking another partial derivative. In two dimensions, equation (1) thus reduces to a scalar equation involving a single (unknown) modulus quantity (μ) and two (known) displacement components (u_1, u_2). Phantom results were shown for a 20 × 20 (4 mm^{2}p ixel) grid, 5 mm deformation and low-contrast modulus ratio <2. Chenevert *et al* have applied the Skovoroda method to static MR displacement data (Chenevert *et al* 1998). Results were shown in phantoms and *ex vivo* kidney encased in gel for a 128 × 128 grid and 1.5 mm compression. More recently, the method was extended to account for nonlinear effects, and an integral formalism introduced for improved performance with noisy data (Skovoroda *et al* 1999).

Kallel has presented a nonlinear iterative solution for static ultrasound data (Kallel and Bertrand 1996). In that approach, (1) is expressed using Poisson's ratio in place of Lamé constant λ:

$$\lambda = \frac{2\mu\nu}{1-2\nu} \tag{2}$$

and a near-incompressible value of $\nu = 0.495$ is assigned for all tissues, leaving only modulus μ as a single unknown. A Gauss–Newton algorithm was used to solve the least-squared error minimization problem

$$\min ||u(\mu) - u_m||^2 \tag{3}$$

in an iterative fashion. Here, u_m represents the experimentally measured displacement data, and $u(\mu)$ represents the calculated displacement from the current estimate of modulus. Results were shown in simulated data with and without noise for a 25×25 grid, 0.5 mm compression, and low-contrast modulus ratio of 3.

Ehman *et al* have presented two inversion methods to analyse dynamic shear wave MR data. Initially, modulus is inferred through estimation of local wavelength (Manduca *et al* 1996). The resolution of this method is related to the shear wavelength, but it is straightforward to implement. As an extension of this method, equation (1) was expressed as an inverse scattering problem and solved iteratively (Dutt *et al* 1997). Results were presented for noise-free simulated data on a 128×128 grid (1 mm^2), and low modulus contrast <3.

Recently, Sinkus *et al* (1999) and Weaver *et al* (1999) analysed MR elastography data with a steady-state harmonic model where the displacement $\boldsymbol{u} = \boldsymbol{U}e^{i\omega t}$:

$$\nabla(\lambda\nabla\cdot\boldsymbol{U}) + \mu(\nabla^2\boldsymbol{U} + \nabla\nabla\cdot\boldsymbol{U}) + \nabla\mu(\nabla\boldsymbol{U} + \nabla\boldsymbol{U}^T) = -\omega\gamma\boldsymbol{U} + \omega^2\rho\boldsymbol{U}. \tag{4}$$

Weaver solved this equation with the Poisson's ratio approximation (equation (2), $\nu = 0.49$) and an iterated Gauss–Newton method. As a further refinement to break down the computational load, the reconstruction field of view was subdivided into smaller regions of interest, solved in parallel, and reassembled. Sinkus *et al* were the first to produce a three-dimensional reconstruction from 3D displacement data. Using the Poisson's ratio approximation and assuming that modulus is locally constant ($\nabla\mu = 0$):

$$\frac{E}{2(1+\nu)}\nabla^2\boldsymbol{U} + \frac{E}{2(1+\nu)(1-2\nu)}\nabla\nabla\boldsymbol{U} = -\omega\gamma\boldsymbol{U} + \omega^2\rho\boldsymbol{U} \tag{5}$$

thereby converting the boundary value problem to a pixel-by-pixel calculation.

Finally, Plewes *et al* (2000) have described an iterative approach that is highly constrained through use of *a priori* knowledge of the lesion geometry. This method is ideal for assessing focal masses where the inclusion can be segmented from normal tissue along a discrete boundary. It is computationally efficient in that the modulus update calculation is performed on a pixel-by-pixel basis as in Sinkus *et al* (1999), rather than solving a system of simultaneous equations as in Kallel and Bertrand (1996) or Weaver *et al* (1999).

In the following section, we describe modifications to the linear inversion technique of Skovoroda *et al* (1995) in the handling of the Lamé constant λ, and in the use of regularization. These modifications are then shown to reduce the SNR requirements in the displacement data.

2. Theory

Plane strain conditions are often used to describe a cross-sectional state of stress in an object which is very long. It is assumed that motion in the long dimension is negligible compared with motion in the cross-sectional dimensions. Thus, a state of symmetry can be employed to make

approximate solutions in two dimensions. Most previous discussions of inverse problems in MR elastography assume plane strain conditions, but it is noted that such approximations are not very accurate for spherical inclusions (Bilgen and Insana 1998). However, an approximate state of plane strain can be achieved by simply constraining the material in one dimension, as shown below. The rest of this section assumes two-dimensional plane strain.

In incompressible materials such as soft tissue, the term $\lambda\nabla\cdot\boldsymbol{u}$ in (1) is indeterminate. It can be replaced by a variable p which is interpreted as the average pressure-stress. The vector equation describing static equilibrium in a linearly elastic material is thus:

$$\nabla p + \mu(\nabla^2\boldsymbol{u} + \nabla\nabla\cdot\boldsymbol{u}) + (\nabla\mu)(\nabla\boldsymbol{u} + \nabla\boldsymbol{u}^T) = 0. \tag{6}$$

Using finite difference discretization of (6), a matrix equation can be assembled:

$$Kx = b, \qquad x = \{\mu_1, \mu_2, \ldots \mu_n, p_1, p_2, \ldots, p_n\}^T \tag{7}$$

where x is the solution vector, K is a $2n \times 2n$ matrix of displacement derivatives (stiffness matrix) and b is the right-hand side vector containing boundary condition information. Alternatively, pressure may be eliminated from (6) analytically, with the use of a third differential operation, as shown by Chenevert *et al* (1998). However, we retain p as an unknown, such that derivatives of the displacement vector field are limited to second order; this improves the conditioning of the stiffness matrix K. Furthermore, K has a 2×2 block structure of $n \times n$ submatrices K_{ij}:

$$K = \begin{pmatrix} K_{11} & K_{12} \\ K_{21} & K_{22} \end{pmatrix} \tag{8}$$

which can be utilized to optionally rewrite (7) as an $n \times n$ matrix equation $K'x = b'$ with:

$$K' = K_{11} - K_{12}\cdot K_{22}^{-1}\cdot K_{21}, \qquad b' = b_1 - K_{12}\cdot K_{22}^{-1}\cdot b_2 \tag{9}$$

whereby solution x is now an $n \times 1$ vector containing only the modulus variables μ_i. The elimination of pressure has been achieved through matrix partitioning rather than partial differentiation. The matrix partitioning operation is reliable because there are no displacement terms in the coefficient of the ∇p term. Therefore, K_{22} is a noise-free orthogonal matrix and the inverse is trivial to compute.

Tikhonov regularization (Hansen *et al* 1998) is formulated by the problem:

$$\min\{||Kx - b||^2 + \eta^2||L(x - x_0)||^2\} \tag{10}$$

where η is the regularization parameter, L is a Laplacian smoothing operator and x_0 is an initial solution guess. Depending on the value of η, the solution is biased towards greater smoothness and away from the actual data in matrix K. The solution is:

$$x_{L,\eta} = (K^TK + \eta^2L^TL)^{-1}(K^Tb + \eta^2L^Tx_0) \tag{11}$$

and can be expressed in terms of the generalized singular value decomposition (GSVD) of the matrices K, L in such a way that solutions for multiple values of η are efficiently computed with matrix multiplication operations (Golub and van Loan 1996).

In the following sections, three variants of the stiffness matrix K are analysed, and will be denoted as follows. $K2$ refers to the stiffness matrix of equation (7) with two solution variables and size $2n \times 2n$. $K2'$ refers to the stiffness matrix of equation (9) with one solution variable and size $n \times n$. Finally, $K1$ refers to the stiffness matrix of Chenevert *et al* (1998) where pressure has been eliminated analytically, with one solution variable and size $n \times n$.

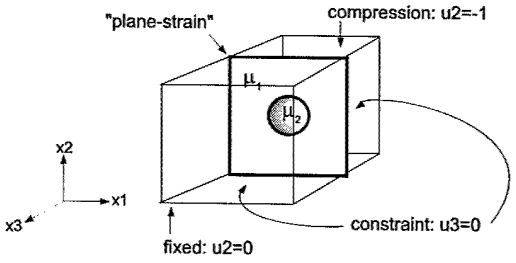

Figure 1. The model object used in three-dimensional simulations was a cube (thin solid lines) with a spherical inclusion (shaded). The object was discretized on a 48 × 48 × 48 grid, and compression was simulated with a constraint (arrows) in the x_3 direction. The model object used in two-dimensional linear inversion calculations corresponds to the central x_1, x_2 plane of the three-dimensional object, as outlined in the thick solid lines. The 2D object was discretized on a 32 × 32 grid.

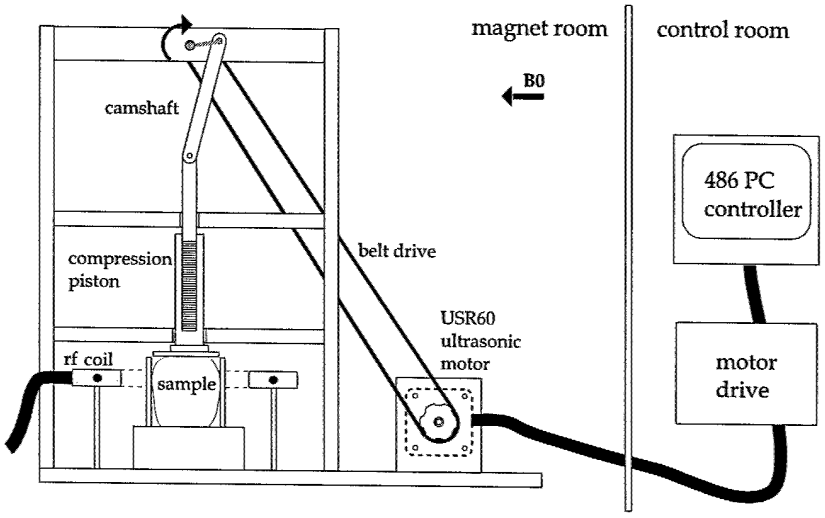

Figure 2. Experimental apparatus used to apply quasistatic deformation to test objects in the bore of the magnet. The sinusoidal motion of the compressor is achieved through a camshaft driven by a rotary ultrasonic motor at 1–2 Hz. Two vertical plates are shown constraining the sample from displacing in the horizontal direction, while the sample is free to deform in the direction perpendicular to the page.

3. Methods

Simulations and experiments were initially conducted to demonstrate that plane-strain conditions can be achieved in a three-dimensional object through use of physical constraints. A three-dimensional inclusion object was simulated with a 48 × 48 × 48 mesh (figure 1). A compression of 5% was simulated with zero-displacement constraints applied at the x_3 direction boundaries. The experimental three-dimensional inclusion phantom was constructed from plastisol PVC (M-F Manufacturing Company, Fort Worth, TX), having an inclusion

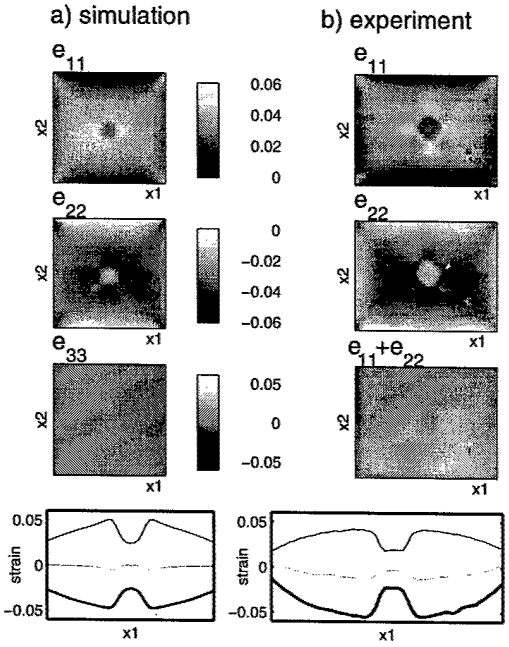

Figure 3. Simulated and experimental strains in a three-dimensional inclusion object. (*a*) Simulated results are shown for strain components e_{11}, e_{22}, and e_{33}. The strain in the restricted direction (e_{33}) is near zero. The bottom graph shows horizontal (x_1) profile plots of e_{11} (——), e_{22} (——) and e_{33} (– – –). (*b*) Experimental results for strain components e_{11}, e_{22} and $e_{11} + e_{22}$. The bottom graph shows horizontal (x_1) profile plots of e_{11} (——), e_{22} (——), and $e_{11} + e_{22}$ (– – –) which are qualitatively very similar to simulation. The aspect ratio is slightly different because the phantom was rectangular while the simulation was square.

modulus of 25.7 kPa and an exterior modulus of 11.9 kPa, as measured independently with benchtop apparatus. The phantom was placed in an MR-compatible compressor device driven by ultrasonic motor (USR60-N4, Shinsei Corp., Tokyo Japan) as illustrated in figure 2. Side panels were positioned to constrain this object in the x_3 direction (i.e. left/right in figure 2), and the motion measured in orthogonal directions with a stimulated-echo phase contrast method (Chenevert *et al* 1998). Imaging parameters used were $T_{\text{mix}} = 100$ ms, TE = 12.4 ms, two signal acquisitions, 64 × 64 matrix in a 9 cm field of view, and 4 mm slice thickness. The imaging sequence was prospectively gated to the sinusoidal motion signal, which had a period of 660 ms and an amplitude of 4 mm.

The linear inversion was evaluated with simulated data in two-dimensional plane strain to compare the three different discretization methods ($K1$, $K2$, $K2'$). The model geometry had a circular inclusion within a square field of view, denoted by heavy lines in figure 1. The sharp transition in modulus distribution was smoothed slightly with a 5 × 5 Gaussian convolution filter having a full-width half-maximum of 2.2 pixels. This smoothing is required because the finite difference approximations which are made in assembling equation (7) are first-order central differences, meaning that sharp discontinuities cannot be properly reconstructed. A finite element numerical method (Abaqus v5.8.1, HKS Inc.) was used to generate displacement data from this geometry corresponding to a strain of 5%. Normally distributed noise was added

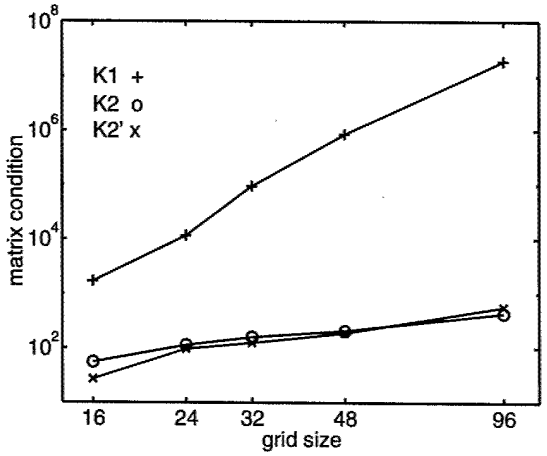

Figure 4. The stiffness matrix condition number for each of the discretization methods ($K1$, $K2$, $K2'$) is plotted as a function of grid size. The grid size is the number of discrete nodes per spatial dimension. All subsequent inversions used a grid size of 32 × 32.

to the displacement vector to establish a signal/noise ratio in the displacement data that would correspond to experimentally measured data. Since displacement varies throughout the field of view in quasistatic elastography, the displacement SNR is quoted as the ratio of maximum displacement at the object surface to standard deviation of the noise. These noisy displacement data then became the input to the inverse calculation. The computing time for the GSVD of the matrices K, L is proportional to n^3, and took about 90 min on a Sun Ultra 10 workstation for the $K2$ matrix on a 32 × 32 grid.

Two theoretical methods of selecting η were initially studied. The discrepancy principle (Morozov 1984), which balances the residual norm ($\| Kx - b \|_2$) against the noise in b, tended to oversmooth the result in the simulations. Furthermore, the noise in b may not be precisely known in experimental data, so this method was discarded. L-curve analysis (Hansen *et al* 1998), which balances the residual norm against the smoothing norm ($\| Lx \|_2$) yielded good results for very high SNR. With the lower SNR values selected in this study, the L-curve approach was also unsuccessful. Consequently, the 'best' value of η was difficult to define in a numerical fashion. Instead, 14 trial solutions were generated with η values ranging over two orders of magnitude. The value of η was determined empirically from that solution which presented a reasonable balance between numerical artefact and over-smoothing of the inclusion. The trial solutions required only a few minutes to generate once the GSVD of the matrices K, L was available. Typical values of η ranged between 0.05 and 0.1 for the various simulations in this study. In addition, the experimentally measured displacement data were processed with the $K2$ discretization.

4. Results

Figure 3 presents simulated and experimental results for compression of a three-dimensional object under lateral constraint. In the simulation (figure 3(a)), the strain component corresponding to the constrained direction (e_{33}) shows that a good state of plane strain is achieved. The experimental results (figure 3(b)) show the strain components measured

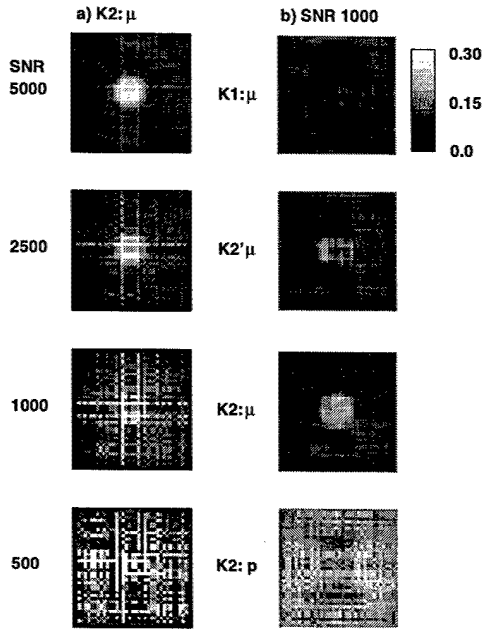

Figure 5. Linear inversion reconstruction results are shown for various SNR levels in the simulated displacement data. All images are displayed with the same colourmap. (*a*) The left column of images shows the modulus reconstruction by LU decomposition (unregularized) from the $K2$ discretization. As the SNR level decreases below 1000, the solution rapidly diverges. (*b*) The right column shows the regularized modulus reconstruction for each discretization and SNR = 1000, as well as the $K2$ pressure reconstruction. The regularization parameters were 0.05, 0.1 and 0.06 for $K1$, $K2'$, $K2$ respectively.

in the two unconstrained dimensions e_{11} and e_{22}. The component e_{33} was not measured experimentally so the sum $e_{11} + e_{22}$ is shown in comparison with the component e_{33} of the simulation. A horizontal profile of $e_{11} + e_{22}$ demonstrates that $e_{11} \simeq -e_{22}$. Since the Poisson's ratio of plastisol is >0.499 (Erkamp *et al* 1998), the trace of the strain tensor should be zero, and thus it is concluded that there is virtually no strain in the x_3 direction.

The stiffness matrix K can be characterized by the condition number, which is a measure of the sensitivity to perturbations in the displacement data such as noise or discretization errors (Golub and van Loan 1996). In figure 4, the matrix condition is plotted for each discretization method: combined pressure/modulus ($K2$), modulus only by matrix partitioning ($K2'$) and modulus only by partial differentiation ($K1$). The grid size is the number of discrete nodes per spatial dimension. As the relative degree of perturbation approaches the reciprocal of the condition number, the LU decomposition solution to equation (7) will typically begin to diverge. The graph in figure 4 shows the relative advantage in matrix conditioning in $K2$ and $K2'$ where calculation of the third spatial derivative of displacement has been avoided.

Figure 5 shows results for the linear inversions on simulated two-dimensional data. In the left column (figure 5(*a*)), the LU decomposition (unregularized) modulus reconstruction of the $K2$ stiffness matrix is shown for various displacement SNR between 500 and 5000. The solution diverges for SNR below 1000. In the right column (figure 5(*b*)), the regularized solution for each of the three discretizations ($K1$, $K2$, $K2'$) is presented for SNR = 1000.

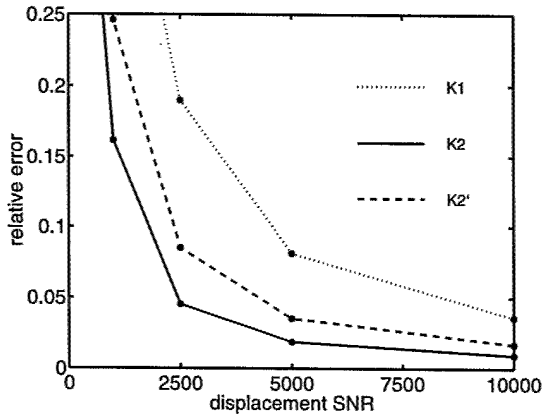

Figure 6. RMS error for the regularized modulus reconstruction by each discretization method ($K1$, $K2$, $K2'$) is plotted as a function of the displacement SNR. Data points (circles) are connected by straight lines for qualitative comparison.

The effect of regularization may be directly compared on the third row of the figure, where the $K2$ modulus reconstruction is presented with and without regularization. Although much artefact is removed by the regularization, there is clearly some attenuation of the modulus as well, so SNR $= 1000$ can be interpreted as a bare minimum requirement. The regularized modulus reconstruction for $K2$is somewhat worse than for $K2$, and the inclusion can just be detected in the $K1$ reconstruction. The pressure reconstruction from the $K2$ matrix is noisy and of less intrinsic interest, except as a means of obtaining a better modulus reconstruction.

Figure 6 plots the rms error in the modulus reconstruction returned by the three methods of discretization. Depending on the tolerance on this reconstruction error, the $K2$ and $K2'$ discretization methods offer from two to four times reduction in required SNR for an equivalent level of reconstruction error. Figure 7 illustrates the $K2$ modulus reconstruction of the experimental data in figure 3. The magnitude image (figure 7(a)) shows a relatively good SNR of about 60. There are approximately two cycles of phase wrap in the data, so the corresponding displacement SNR is roughly $2 \times 2\pi \times 60 = 750$. The noise was further reduced by 50% using a 9×9 Gaussian convolution filter of full-width half-maximum 1.5 pixels prior to reconstruction. In addition to reducing noise, this filter also smooths the discontinuity in the displacement data due to the sharp boundary of the inclusion, as required for central difference approximation of differentiation. The regularized modulus reconstruction is shown as a value relative to 1 in the background region of the phantom (figure 7(b)). Figure 7(c) shows a line profile of the reconstructed modulus, and a simulated profile corresponding to the benchtop measurements of elastic modulus in the separate material components of the phantom.

5. Conclusions

In direct linear inversion of MR elastography data, SNR requirements are fairly high due to the ill-conditioning of the inversion equations. We have described the benefits of solving for pressure simultaneously with elastic modulus in a linear inversion procedure. Retaining pressure as an unknown has the advantage of improving the conditioning of the numerical problem, but it carries an additional computational expense of roughly a factor of eight.

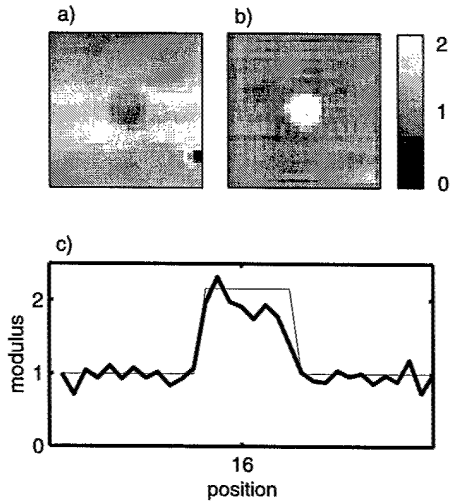

Figure 7. (*a*) A 32 × 32 region of interest in the magnitude image of the three-dimensional inclusion phantom shows relatively high SNR of 60. The inclusion appears dark, due to a shorter T2 relaxation time. The dark area at bottom right is an air bubble. (*b*) Relative modulus reconstruction of experimental data from $K2$ discretization on a 32 × 32 grid. (*c*) Line profile of reconstructed modulus (solid line) compared with the true modulus of the phantom as measured separately on benchtop apparatus (dashed line).

If matrix partitioning (rather than partial differentiation) is used to eliminate the pressure term, a good compromise is obtained whereby computation time is not affected, but some noise tolerance is gained. The decrease in SNR that can be tolerated by using the $K2$ or $K2'$ discretizations ranges from two to four. The recent integral formulation of the $K1$ discretization (Skovoroda *et al* 1999) is also designed to address this noise sensitivity.

Many investigators have identified the goal of solving a three-dimensional modulus distribution with accompanying 3D displacement data set. However, even a low-resolution 3D reconstruction is a challenging numerical problem and data acquisition requirements are substantial (Chenevert *et al* 1999). As an alternative, we have demonstrated with phantoms made of incompressible materials that confinement techniques may be used to effectively produce plane-strain conditions, such that measurement and analysis can be conducted in two dimensions.

The sensitivity to perturbation in the inversion equations means that filtering must be considered for two purposes. If the displacement SNR is low, then the noise must be reduced to obtain SNR $>$ 1000. If the SNR is high, some filtering must still be applied to eliminate discontinuities which cannot be reconstructed by low-order finite difference approximations. It is possible to use finite difference approximations corresponding to higher-order interpolating polynomials, but if it is known in advance that some low-pass filtering will be required to deal with noise in the data, then first-order approximations are sufficient. While the requirement of SNR $>$ 1000 is high, we have recently demonstrated *in vivo* displacement SNR of 300 in parenchymal tissue (Plewes *et al* 2000). In that procedure, two components of displacement were obtained in one slice location during four minutes of scan time. Improvements to our phased array detector, combined with the option of increasing the relatively brief scan time, should be sufficient to obtain a displacement SNR of 1000 *in vivo*. Nevertheless, the linear inversion is a demanding problem and may ultimately be inappropriate for use *in vivo*; Plewes *et al* (2000) also contains a discussion of a more robust reconstruction methodology.

In the context of breast MRI, it can be assumed that lesion detection is accomplished with Gd-DTPA enhanced 3D MRI. Elastography must only help classify a particular lesion as benign or malignant. Thus, reconstruction is only required on a localized ROI surrounding a specific lesion of interest, which greatly simplifies the numerical complexity of the problem, as originally noted in Skovoroda *et al* (1994). The 32×32 grid described above is representative of the size required for a localized reconstruction.

Acknowledgments

The authors gratefully acknowledge the support of the Terry Fox Foundation (programme project grant 006886) and the US Army (DAMD 17-99-1-9391).

References

Andreev V, Dmitriev F, Pishchal'nikov Y, Rudenko O, Sapozhnikov O and Sarvazyan A 1997 Observation of shear waves excited by focused ultrasound in a rubber-like medium *Acoust. Phys.* **43** 123–8

Bilgen M and Insana M 1998 Elastostatics of a spherical inclusion in homogeneous biological media *Phys. Med. Biol.* **43** 1–20

Bishop J and Plewes D 1998 An alternate method for calculating elastic properties of breast tissue *Proc. Sixth Meeting of the ISMRM (Sydney)* p 2102

Chandrasekharaiah D and Debnath L 1994 *Continuum Mechanics* (New York: Academic)

Chenevert T, Skovoroda A, O'Donnell M and Emelianov S 1998 Elasticity reconstructive imaging by means of stimulated echo MRI *Magn. Reson. Med.* **39** 482–90

Dutt V, Manduca A, Muthupillai R, Ehman R and Greenleaf J 1997 Inverse approach to elasticity reconstruction in shear wave imaging *IEEE Int. Ultrasonics Symp., Program and Abstracts* p 184

Erkamp R, Wiggins P, Skovoroda A, Emelianov S and O'Donnell M 1998 Measuring the elastic modulus of small tissue samples *Ultrason. Imaging* **20** 17–28

Golub G and van Loan C 1996 *Matrix Computations* 3rd edn (Baltimore, MD: The Johns Hopkins University Press)

Hansen P 1998 *Rank-deficient and Discrete Ill-posed Problems* (Philadelphia, PA: SIAM)

Kallel F and Bertrand M 1996 Tissue elasticity reconstruction using linear perturbation method *IEEE Trans. Med. Imaging* **15** 299–313

Manduca A, Muthupillai R, Rossman P, Greenlead J and Ehman R 1996 Image processing for magnetic resonance elastography *Proc. SPIE* **2710** 616–23

Morozov V 1984 *Methods for Solving Incorrectly Posed Problems* (New York: Springer)

Ophir J, Kallel F, Varghese T, Bertrand M, Cespedes I and Ponnekanti H 1997 Elastography: a systems approach *Int. J. Imaging Syst. Tech.* **8** 89–103

Pelc N, Herfkens R, Shimakawa A and Enzmann D 1991 Phase contrast cine magnetic resonance imaging *Magn. Reson. Q.* **7** 229–54

Plewes D, Bishop J, Samani A and Sciarretta J 2000 Visualization and quantification of breast cancer biomechanical properties with magnetic resonance elastography *Phys. Med. Biol.* **45** 1591–610

Sarvazyan A *et al* 1994 Elasticity imaging as a new modality of medical imaging for cancer detection *Proc. Int. Workshop on Interaction of Ultrasound with Biological Media (Valenciennes, France)* pp 69–81

Sinkus R, Lorenzen J, Schrader D, Lorenzen M, Dargatz M and Holz D 2000 High-resolution tensor MR elastography for breast tumour detection *Phys. Med. Biol.* **45** 1649–64

Skovoroda A, Emelianov S, Lubinski M, Sarvazyan A and O'Donnell M 1994 Theoretical analysis and verification of ultrasound displacement and strain imaging *IEEE Trans. Ultrason. Ferroelectr. Freq. Control* **41** 302–13

Skovoroda A, Emelianov S and O'Donnell M 1995 Tissue elasticity reconstruction based on ultrasonic displacement and strain images *IEEE Trans. Ultrason. Ferroelectr. Freq. Control* **42** 747–65

Skovoroda A, Lubinski M, Emelianov S and O'Donnell M 1999 Reconstructive elasticity imaging for large deformations *IEEE Trans. Ultrason. Ferroelectr. Freq. Control* **46** 523–35

Steele D, Chenevert T, Skovoroda R and Emelianov S 2000 Three-dimensional static displacement, stimulated echo NMR elasticity imaging *Phys. Med. Biol.* **45** 1633–48

Weaver J, van Houten E, Miga M, Kennedy F, Hartov A, Poplack S, Nagy H and Paulsen K 1999 Measurement of harmonic motion for MR elastography *Proc. ISMRM, 7th Meeting (Philadelphia, PA)* p 1617